TECHNISCHE UNIVERSITÄT DRESDEN

Faculty of Computer Science Institute of Artificial Intelligence

DYNAMIC THERMAL IMAGING FOR INTRAOPERATIVE MONITORING OF NEURONAL ACTIVITY AND CORTICAL PERFUSION

Dipl.-Inf. Nico Hoffmann
Born on: 26.2.1987 in Pirna

DISSERTATION

to achieve the academic degree

DOKTOR RERUM NATURALIUM (DR. RER. NAT.)

Supervisor
Sen.-Prof. Dr.-Ing. habil. Uwe Petersohn

Referee
Prof. Dr. med. Arya Nabavi MaHM

Dresden, 25.04.2016
Defended on: 09.12.2016

ABSTRACT

Neurosurgery is a demanding medical discipline that requires a complex interplay of several neuroimaging techniques. This allows structural as well as functional information to be recovered and then visualized to the surgeon. In the case of tumor resections this approach allows more fine-grained differentiation of healthy and pathological tissue which positively influences the postoperative outcome as well as the patient's quality of life.

In this work, we will discuss several approaches to establish thermal imaging as a novel neuroimaging technique to primarily visualize neural activity and perfusion state in case of ischaemic stroke. Both applications require novel methods for data-preprocessing, visualization, pattern recognition as well as regression analysis of intraoperative thermal imaging.

Online multimodal integration of preoperative and intraoperative data is accomplished by a 2D-3D image registration and image fusion framework with an average accuracy of 2.46 mm. In navigated surgeries, the proposed framework generally provides all necessary tools to project intraoperative 2D imaging data onto preoperative 3D volumetric datasets like 3D MR or CT imaging. Additionally, a fast machine learning framework for the recognition of cortical NaCl rinsings will be discussed throughout this thesis. Hereby, the standardized quantification of tissue perfusion by means of an approximated heating model can be achieved. Classifying the parameters of these models yields a map of connected areas, for which we have shown that these areas correlate with the demarcation caused by an ischaemic stroke segmented in postoperative CT datasets.

Finally, a semiparametric regression model has been developed for intraoperative neural activity monitoring of the somatosensory cortex by somatosensory evoked potentials. These results were correlated with neural activity of optical imaging. We found that thermal imaging yields comparable results, yet doesn't share the limitations of optical imaging. In this thesis we would like to emphasize that thermal imaging depicts a novel and valid tool for both intraoperative functional and structural neuroimaging.

ZUSAMMENFASSUNG

Die Neurorchirurgie stellt einen hochtechnologisierte Fachbereich innerhalb der Medizin dar. Durch den Einsatz von Neuroimaging-Methoden können in dieser Disziplin strukturelle sowie funktionelle Informationen aufbereitet und dem Chirurgen bereitgestellt werden. Im Rahmen von Tumorresektionen lässt sich hiermit eine feinere Abgrenzung von regelrechtem zu pathologischen Geweben etablieren. Dies beeinflusst das postoperative Outcome sowie die Lebensqualität des Patienten positiv.

In der vorliegenden Arbeit werden neuartige Methoden vorgestellt, um die Wärmebildgebung für die intraoperative Visualisierung von neuronaler Aktivität sowie Infarktdemarkierungen einzusetzen. Hierzu wurden Methoden zur Daten-Vorverarbeitung, Visualisierung, Mustererkennung sowie zur semiparametrischen Regressionsanalyse von intraoperativen Wärmebildaufnahmen erforscht.

Zur Visualisierung wurde ein online 2D-3D Framework zur Bildregistration und -fusion entwickelt, was eine mittleren Genauigkeit von 2.46 mm erreicht. Mit diesem Framework können in navigationsgestützen Eingriffen beliebige intraoperative kalibrierte 2D Imagingdaten auf preoperative volumetrische Datensätze abgebildet (z.B. MRT, CT) werden. Zusätzlich wurde ein Verfahren des maschinellen Lernens zur Erkennung von NaCl-Spülungen des Kortex erforscht. Dieses ermöglicht die Untersuchung der Gewebeperfusion an Hand eines Modells des Erwärmungsverhalten von Gewebe nach Applikation eines Temperaturgradienten. Die Segmentierung der Modellparameter liefert schließlich eine Karte mit zusammenhängenden Gebieten ähnlicher Perfusion. Es konnte gezeigt werden, dass diese Gebiete mit der Infarktdemarkierung aus postoperativen CT-Datensätzen korreliert.

Mit einem neuartigen semiparametrischen Regressionsmodell konnte neuronale Aktivität auf dem sensorischen Kortex bei somatosensorisch-evozierten Potentialen nachgewiesen werden. Optical Imaging Aufnahmen wurden gleichzeitig zu den Wärmebildaufnahmen erfasst, um die Ergebnissen entsprechend abzugleichen. Wir konnten eine Korrelation zwischen den Ergebnissen beide Modalitäten zeigen, wobei die Wärmebildgebung nicht den Beschränkungen von Optical Imaging unterliegt. Zusammenfassend wurden in dieser Arbeit neuartige und validierte Werkzeuge zum Einsatz der Wärmebildgebung sowie zur funktionellen- als auch strukturellen Neurobildgebung erforscht sowie an Hand von intraoperativen Studien validiert.

> Valar dohaeris!
>
> ---
> The traditional response to *valar morghulis*.

Significant advances in intraoperative neuroimaging require a complex interplay of various professions. Hence the achievements of this work would not have been possible without the support of many individuals! Hereby I would like to say thank you to all companions with whom I have collaborated over the past years. First and foremost I'm very grateful for the persistent support, advice and all valuable discussions with my doctoral supervisor Sen.-Prof. Dr. Uwe Petersohn! Our stimulating discussions always broadened my perspective of machine learning and scientific research in general. By means of his support I was able to pursue and improve my scientific ideas! Additionally, Prof. Dr. Nabavi helped me to improve this thesis as well as my scientific career by his valuable advices, remarks and hints. Thank you! Furthermore, I appreciate the many interesting, challenging and helpful discussions with Prof. Dr. Matthias Kirsch, Prof. Dr. Edmund Koch, Dr. Gerald Steiner, Julia Hollmach and Dr. Yordan Radev regarding the problems encountered as well as novel ideas to approach medical or intraoperative challenges. It was very inspiring to discuss advances in neuroscience and intraoperative optical imaging (IOI) with Dr. Tobias Meyer. His longstanding research regarding IOI as well as the research of Prof. Dr. Kirsch and Dr. Steiner were the most important prerequisites for the realization of intraoperative thermal imaging in Dresden. Without the profound engineering knowledge of Dr. Christian Schnabel and Mirko Mehner, some of the advanced technical building blocks of this thesis would not have been feasible. The surgical personnel of the University Hospital Dresden were and are another very important factor to the research of this thesis, as they enabled and backed intraoperative recordings. Furthermore my thanks goes to Dana Müller-Niegsch, who always gave me the correct antidote to cure broken English. I want to thank all of the former and current colleagues, students and interns of the working group Clinical Sensing and Monitoring for providing such a familiar environment and many inspiring talks as well as discussions. The memories of our Christmas singing always cheer me up! I'm very thankful to all of my friends for their appreciation, acceptance, and trust. A very special thank goes to Kathleen and Beate, who guided me through a very difficult time of my life.

Schließlich möchte ich meiner Mutter und meinem leider kürzlich verstorbenen Vater für ihr ausdauerndes und unumstößliches Vertrauen, ihre Förderung sowie Unterstützung danken!

CONTENTS

Contents

LIST OF FIGURES

LIST OF TABLES

1. NEUROSURGICAL BACKGROUND

The human central nervous system (CNS) consists of the brain and the spinal cord and is therefore a vital part of body. It coordinates conscious and unconscious behavior and enables the forwarding as well as processing of external and internal stimuli. The latter ability relies on neurons (nerve cells) and glial cells. Glial cells represent a larger group of cells that support neurons by electrically isolating them. Neurons are specialized cells which are responsible for processing and forwarding stimuli, which yields a mechanism to store information. They are connected to each other by nerve fibers of varying strength (axons), allowing stimuli to be forwarded. This stimuli can be thought of as an electrochemical impulse (action potential), which is forwarded only if it surpasses a certain threshold [12].

Disorders of this system require medical intervention in the field of neurosurgery. The latter is a highly specialized and technological medical discipline covering the diagnostics and treatment of disorders of the CNS. These range from diseases of the spinal cord, traumatic events, and vascular disorders in the brain to malign uncontrolled growth of abnormal cells. Neurosurgical methods include, among others, open surgery, microsurgery, stereotaxy, stereotactic radiosurgery and endovascular neurosurgery. For diagnostics and OP planning, a close collaboration with neuroradiology is necessary since this discipline provides necessary imaging tools and experience to explain neurological disorders. Hereby, neuroimaging denotes various approaches to measure and visualize neural activity, structure and cerebral perfusion at different micro- as well as microscopic scales. Because of the small electrical gradients that action potentials cause, it is difficult to image them directly. Alternatively, neuroimaging methods analyzing neural activity rely on indirect approaches to monitor neural activity by exploiting several aspects of neurovascular coupling.

1.1. BRAIN TUMOR

The steady growth of abnormal cells in the brain is denoted by brain tumor. These cells can be categorized by their origin, for example Glioblastoma multiforme originate from a massive proliferation of Glial cells. This growth causes an increased cerebral pressure (ICP) leading to pathophysiological symptoms like edema [70]. Increased intracerebral pressure of tumors of the cerebral cortex causes severe tissue mass movements and lastly a compression of the brainstem, as well as a displacement of parts of the temporal lobe into the posterior cranial fossa [70] significantly endangering the patient's life.

In general, brain tumors can be described by several aspects that we will introduce shortly.
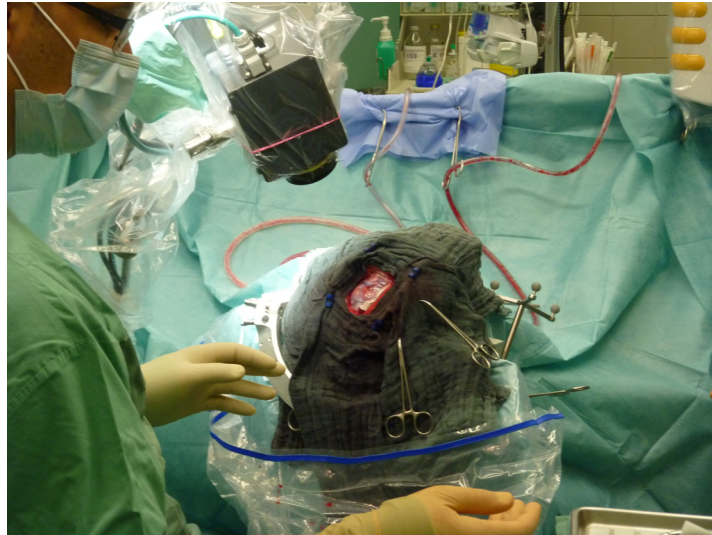
Figure 1.1.: First experiments were done with the thermal imaging system being directly connected to the OP table to enable low distance measurements.

Neoplasia denotes the uncontrollable growth of tumor cells. This ultimately compresses healthy tissue, increases the intracerebral pressure and destroys brain parenchyma. Anaplasia means the dedifferentiation or loss of differentiation of tumor tissue to healthy tissue and blood vessels. The degree of abnormality is called atypia. Another important factor of brain tumors is called necrosis. Necrosis denotes the abnormal way of cells dying, since it doesn't follow the common apoptosis cell-death pathway. With this, phargocytes are prevented from transporting the cell components away, leading to an accumulation of dead former cell components.

Brain tumors can be further categorized by their progression rate and shape. Malign tumors can be characterized by fast and infiltrative growth, whereas benign tumors shower slower growth rates and stronger differentiation to healthy tissue. Primary tumors originate from the brain, while secondary tumors originate from another part of the body and infiltrate the brain by a weakened blood-brain barrier. These abnormal cells are called brain metastasis tumor [48].

The following WHO classification [56] provides a rough classification of the malignancy grade of brain tumors (mean survival times are taken from [70])

   I) benign, highly differentiated, very slow growth rate, 5 or more years

   II) semi-benign, highly differentiated, slow growth rate, 3 to 5 years

   III) semi-malign, hardly differentiated, fast growth rate, 2 to 3 years

   IV) malign, undifferentiated, very fast growth rate, 6 to 15 months

There is no known single cause for brain tumors, yet one factor has been shown to increase the risk of getting a brain tumor: exposure to ionizing radiation. Common symptoms are headaches, vomiting, seizures and mental changes [59]. It is estimated that approximately 6,920 inhabitants of Germany develop a primary brain tumor every year [46]. Therefore, the primary brain tumor accounts for a total of 2 % of all cancer-related diseases. In the same year, 5,646 cases of death were reported ([46]).

Figure 1.2.: Recent developments have enabled parallel thermal and optical imaging by adapting the thermal camera to an OP microscope.

Analysis of brain activity using electroencephalography reveals abnormal patterns in the case of intracerebral tumors. Another indication for neoplastic tissue is midline shift caused by accumulation of tissue, leading to anatomic as well as structural changes within brain tissue. Using CT imaging, this pattern can be visualized with an accuracy of 96 - 98 %. Depending on the grade of anaplasia, variations in tissue density can also be a sign of brain tumors. By the application of tracers, it is possible to evaluate hypo- or hyperperfusion caused by tumor tissue. MRI achieves a comparable performance for classifying brain tissue, yet it is more difficult to differentiate edema from tumor tissue. As suggested by [70], MRI yields a better performance in the case of tumors in the cerebellum and brainstem.

The main treatment of brain tumors is the surgical removal of its mass (resection). In the case of anaplastic tumor cells, intraoperative reasoning about healthy and tumor tissue is difficult. In the last years, fluorescence imaging with ICG or 5-ALA as a tumor tracer (see section 2.8.5 for details) has proven to be a valuable tool for a more exhaustive removal of tumor tissue. Typically, the resection is combined with (neo-/adjuvant) radiation therapy and chemotherapy. The former tries to damage the DNA of tumor cells by ionizing radiation, while the latter requires the application of cytotoxic medicaments which primarily target cells with an high cell division rate [59].

There are several other specific curative and palliative methods to treat tumors, for example Cyberknife [1] and Gamma-Knife [82] are such approaches from radiotherapy. By employing a linear particle accelerator or high-intensity gamma radiation, these methods aim to completely remove or reduce the tumor mass. Proton therapy employs a cyclotron or synchrotron to generate proton beams, which are then accelerated, focused and shot to pathological tissue. This seems to be a helpful method in cases when the tumors are difficult to access, however its overall advantage has not yet been proven in literature [96].

(a) Cortex reconstruction from preoperative MRI.

(b) Intraoperative Thermal Neuroimaging fusioned with MRI.
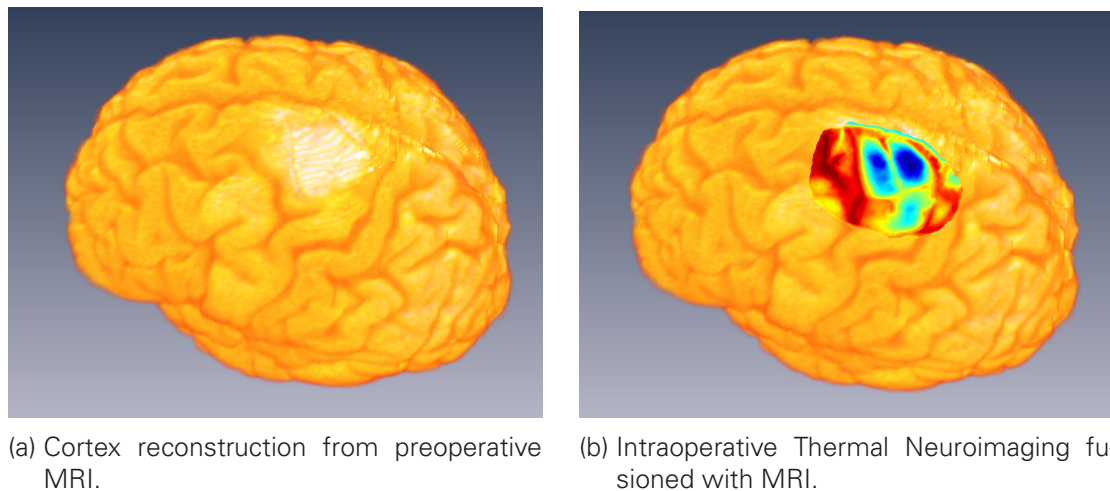
Figure 1.3.: **(a)** The white cluster in this image resembles the contrast enhancement of a grade III Oligoastrocytoma on precentral gyrus. **(b)** The tumor is clearly differentiable as the hypotherm (blue) area in thermal neuroimaging.

1.2. ISCHAEMIC STROKE

A shortage of substrates such as glucose in delimited parts of the brain is denoted by a stroke. This shortage can be caused either by embolic or thrombotic blockage (ischaemic stroke) of a vessel or by a bleeding (hemorrhagic stroke). Both lead to a (temporary) loss of brain function of the affected areas, depending on the duration of the shortage. Consequently, this hypoperfusion induces a chain of biochemical reactions which leads to the loss of function, cell death and a cerebral edema. A shortage of oxygen and glucose for 60 to 90 seconds causes neurons to stop functioning. Irreversible damages are caused after approximately 3 hours. Necrosis is initiated about 4 to 5 minutes after the nutrition supply has stopped [70]. Transient ischaemic attacks denote an ischaemic stroke of less than 24 hours [87].

The shortage of nutritions first affects the metabolic function, leading to a restriction or stopping of neural activity of relevant neurons. This doesn't necessarily cause pathologies since the structure metabolism may still be intact. When the shortage is below a certain threshold, the structure metabolism can't be maintained properly, which causes pathological changes in the tissue [70]. In 2008, 196,000 Germans suffered from a stroke for the first time with 63,000 cases of death [42]. The latter makes a stroke the third most common cause of death in Germany right after heart diseases and cancer. Worldwide, a stroke is the second most common cause of death and the most frequent cause of longer-term disabilities [42].

An acute stroke causes common signs supporting first diagnosis. A reliable stroke diagnostic allowing to differentiate between hemorrhagic and ischaemic strokes and for localizing their origin requires a CT or MRI study of the patient. Yet, an early (12 hours or less) ischaemic stroke is unremarkable in CT measurements, since the edema hasn't formed yet. In general, MRI is the best tool to diagnose an ischaemic stroke with sensitivity of 83 % and specificity of 98 % compared to 16 % and 96 % of CT imaging [15]. Hemorrhagic strokes can be imaged best by CT imaging with a sensitivity of 89 % and a specificity of 100 % [15].

The treatment of an acute stroke depends on pathogenesis. In general, conservative therapy consists of medication in order to optimize vascular parameters. In the case of ischaemic
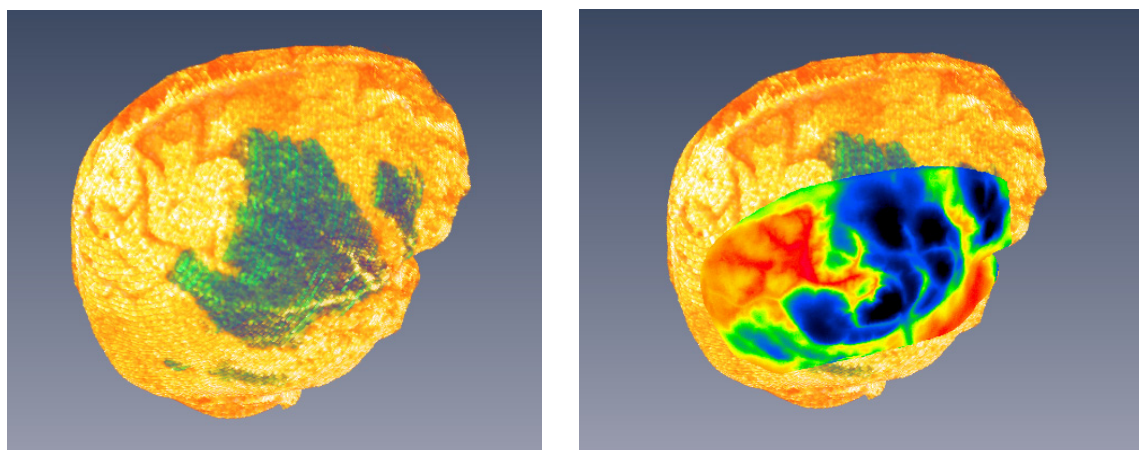
(a) Cortex reconstruction from preoperative CT scan.

(b) Intraoperative Thermal Neuroimaging fusioned with CT.

Figure 1.4.: **(a)** shows the 3d cortex reconstruction of a patient undergoing MCA occlusion. The demarcation is segmented as green area. **(b)** This hypoperfusion also correlates with colder (blue) areas in thermal neuroimaging.

strokes, a treatment by anticoagulants and antithrombotics might improve the outcome. An early thrombolysis of patients with acute ischaemic strokes further reduces mortality rates [78]. For this purpose, several protocols were developed for paramedical personnel, for example FAST [40]. Bleedings must be localized and treated appropriately. A swelling of large areas of the brain might require a decompressive craniectomy to reduce the intracranial pressure.

1.3. THESIS CONTRIBUTION

Intraoperative imaging yields the possibility to gain knowledge about the patient which is either not available prior to surgery or at lowered resolution and accuracy. Improved differentiation of pathological tissue from healthy tissue is a vital component of intraoperative imaging. In the case of tumor resections, the latter allows the patient's postoperative outcome and quality of life to be maximized. In this work we extend the available set of intraoperative tools by thermal neuroimaging so that the neurosurgeons profit from the thermal imaging's abilities to analyze cortical perfusion and vascularization.

Thermal imaging in neurosurgery allows cortical perfusion and cell metabolism to be better understood. By means of neurovascular coupling, it is possible to correlate local changes in cortical perfusion to neural activity and therefore to infer neural activity. Furthermore, the quantification of cortical perfusion provides insights into tissue composition.

In this work we present and discuss approaches to establish thermal imaging as a new and robust technique for intraoperative neuroimaging. In contrary to existing methods, thermal imaging is a whitelight-independent, marker-free and passive approach for recovering structural and functional information. This robustness is especially useful for intraoperative applications since lengthy and error-prone measurements and -protocols are to be prevented in order to minimize intraoperative delay.

We first present a novel camera motion correction scheme tailored to thermal imaging based

(a) Cortex reconstruction with marked postcentral gyrus.

(b) intraoperative functional thermal neuroimaging
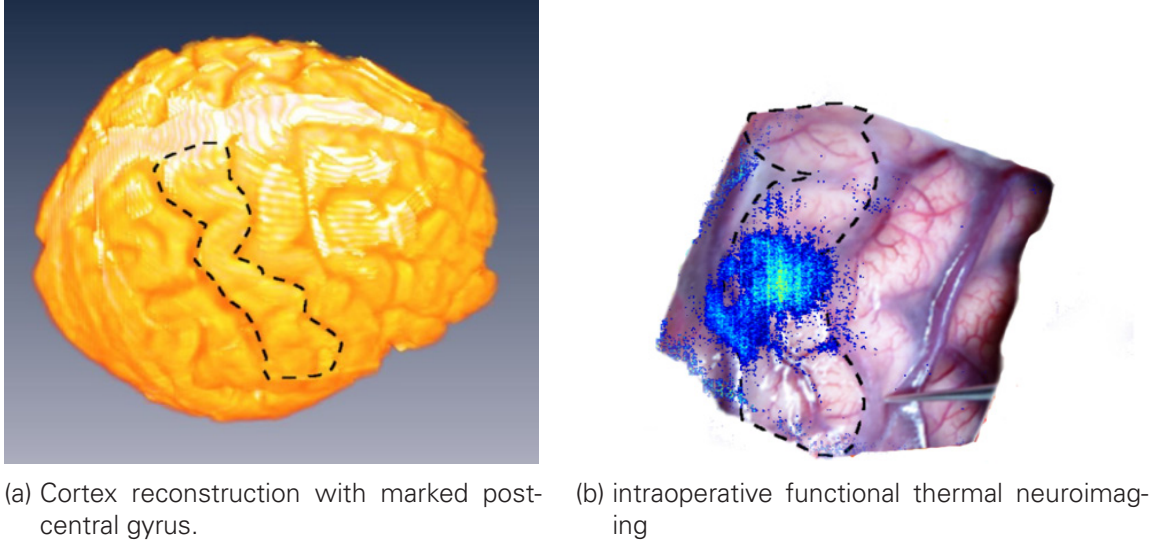
Figure 1.5.: **(a)** The postcentral gyrus (as marked in this figure) is responsible for sensory perception. Through the novel intraoperative thermal neuroimaging the detection of neuronal activity gets tractable as seen in **(b)**. The signal strength is coded by color brightness and fusioned with intraoperative optical imaging. In the case of tumor resections, the information regarding neural activity can guide intraoperative decisions regarding the extent of tumor mass removal.

on pattern recognition in wavelet domain. This initial approach is further improved by an FPGA-based optical flow estimation scheme with real-time performance. In order to exploit all available multimodal information in intraoperative settings and fusion structural with functional information, we further propose a 3D-2D multimodal image registration and image fusion framework to correlate intraoperative 2D thermal and optical imaging with preoperative MRI, CT and PET measurements. The novelty of this approach comes from the fact that the method is generic meaning that it is independent of the actual imaging device. The framework just requires a one-time offline calibration protocol and uses all available information provided by intraoperative neuronavigation systems.

We further provide a sound mathematical semiparametric regression framework to monitor somatosensory activity. This generic framework enables the analysis of various intraoperative experimental designs to unveil evoked neural activity. The model provides all necessary components to recognize statistically significant low SNR patterns of neural activity by incorporating thermal imaging specific artifacts that would otherwise prevent valid statistical inference. The model is used to recognize neural activity by analyzing temperature changes correlating with neurovascular coupling. In the case of tumor resections it is possible to localize the primary somatosensory cortex which improves the differentiation of functional tissue to neoplasms.

We provide a novel approach to the analysis of imaging data of patients suffering acute ischaemic strokes. During decompressive craniectomy, it is common to apply sodium chloride solutions to the cortex to prevent dehydration. We propose an analysis framework to locate these events in thermal recordings of the cortex and provide mathematical models and estimation schemes to quantify the cortical heating behavior after the application of such a solution at high spatial resolutions. We are the first to demonstrate correlations of the cor-

tex' heating behavior with preoperative infarct demarcations. Prospectively, this might be a method for automatic estimation of demarcation progression by combining information from preoperative infarct demarcation and intraoperatively estimated demarcation. This might be a building block to the research of novel local therapies at the boundary of the demarcation area in order to preserve as much tissue as possible.

This work primarily bases on the following publications:

1. Patent DE 10 2014 105 994.8. Nico Hoffmann, Uwe Petersohn, Gerald Steiner, Julia Hollmach, Edmund Koch "Verfahren zur Erkennung von Signalmustern in spektroskopisch erzeugten Datensätzen" (declared 29.04.2014, disclosed 30.10.2014)

2. N. Hoffmann, J. Hollmach, C. Schnabel, Y. Radev, M. Kirsch, U. Petersohn, E. Koch, and G. Steiner. Wavelet subspace analysis of intraoperative thermal imaging for motion filtering. Lecture Notes in Computer Science, 8815:411 – 420, 2014.

3. V. Senger*, N. Hoffmann*, J. Müller, J. Hollmach, C. Schnabel, Y. Radev, J. Müller, M. Kirsch, U. Petersohn, G. Steiner, E. Koch, and R. Tetzlaff. Motion correction of thermographic images in neurosurgery: Performance comparison. In Biomedical Circuits and Systems Conference (BioCAS), pages 121 – 124, 2014. [* both authors contributed equally to this work.]

4. N. Hoffmann, Y. Radev, J. Hollmach, C. Schnabel, M. Kirsch, G. Schackert, U. Petersohn, E. Koch, G. Steiner. Gaussian mixture models for classification of perfused blood vessels in intraoperative thermography. Biomedical Engineering / Biomedizinische Technik. 59(S1):596 - 599, 2014.

5. N. Hoffmann, E. Koch, U. Petersohn, M. Kirsch, and G. Steiner. Cerebral cortex classification by conditional random fields applied to intraoperative thermal imaging. Current Directions in Biomedical Engineering. 2(1): 475-478, 2016.

6. N. Hoffmann, F. Weidner, P. Urban, T. Meyer, C. Schnabel, U. Petersohn, E. Koch, S. Gumhold, G. Steiner, and M. Kirsch. Framework for 2D-3D image fusion of infrared thermography with preoperative MRI. Biomedical Engineering / Biomedizinische Technik, 2017.

7. N. Hoffmann, G. Drache, E. Koch, G. Steiner, M. Kirsch, U. Petersohn. Quantification and Classification of Cortical Perfusion during Ischemic Strokes by Intraoperative Thermal Imaging. TU Dresden technical report TUD-FI16-02, 2016.

8. N. Hoffmann, E. Koch, S. Gumhold, M. Kirsch, G. Steiner. Intraoperative functional thermal imaging of the primary sensory cortex. In: Proceedings of 16th CURAC Annual Conference, 2017.

2. REVIEW OF NEUROIMAGING TECHNIQUES

Neuroimaging denotes a class of medical imaging technologies which aim to image and visualize the structure and function of the central nervous system. Structural imaging denotes the visualization of structures and respective disorders, such as ventricles, vessels and tumor tissue. Prominent examples of this category are CT and MRI. Functional imaging allows the visualization of neural activity. Yet, since action potentials are weak electrical signals, current technologies can't record these directly and have to employ indirect measures such as metabolic activity, regional cerebral blood flow or postsynaptic potentials. In this chapter, we give a brief introduction to the technical foundations of common neuroimaging techniques and show recent advances in the application of machine learning methods to the analysis of this data. These advances are then summarized and discussed with respect to their capabilities and potential shortcomings when analyzing thermal imaging data.

2.1. COMPUTED TOMOGRAPHY

X-rays are electromagnetic radiation at 0.25 nm to 1 pm wavelength. Computed tomography (CT) now employs this radiation to create a visual representation of the interior of objects, such as human organs. For this, a CT consists of a circular array of X-ray sources and detectors. The sources emit radiation towards an object. X-rays now travel on a linear path and pass through the object. Parts of the radiation get absorbed by the material of the object. The actual strength of the absorption process depends on the concrete biochemical composition of the object and is difficult to predict a priori. At the opposite side of the object, the detector measures the transmitted X-ray radiation. This lastly enables the creation of a transverse plane. Each element of this plane represents the attenuation coefficient (Houndsfield units) of the respective object. The scanner, as well as the detector, move axial and lateral dimension in order to capture multiple projections of an object. A volume stack of the recorded object is now created by combining the recorded transverse planes [23].
Mathematically, different projections of an object are recorded. These originate from the X-rays traveling along a linear path through the object. The recovery of an human interpretable representation of the object requires the application of image restoration techniques. It was shown that this task resembles the inverse radon transform. The radon transform denotes
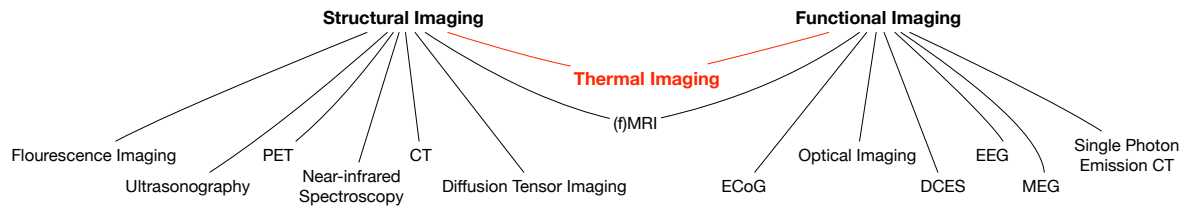
Figure 2.1.: Neuroimaging techniques can be grouped into methods for analyzing cerebral structure and neural activity (function). Most techniques provide information to one of this group, whereas MRI and thermal imaging provide all means for analyzing structure and function.

the integral of certain functions along a linear path. By inverting this function, the goal is to recover each single function value that formed the integral. Historically, this was done using a simple analytical approach called filtered back projection. Nowadays more advanced iterative reconstruction techniques were developed to reduce the noise and other influencing factors. Multi-layer CT employs multiple adjacent detectors and a fan-shaped X-ray source to evaluate multiple parts of an object by a single shot. This can be used to speed-up the measurement or to decrease the slice thickness. A 16-layer CT could reduce the common thickness of 10mm to sub-millimetre scale. Current Dual-Source-CTs use a second 90° shifted X-ray source to further decrease the measurement time. A state-of-the-art CT device of Siemens achieves isotropic resolutions of 0.33 mm and cross-plane resolutions of 0.3 mm [85].

CT imaging allows the prediction of neurological deficits caused by pathologies inducing structural changes such as traumatic brain injuries at an early stage [44]. In the case of an intracerebral tumor, CT imaging isn't capable to differentiate the tumor itself, but rather just of its swelling and the anatomical changes it causes. A radiocontrast agent further enhances the X-ray absorption of perfused vessels and structures. [41] proposed a graphical model for the estimation of lung motion by deformable registration. For this purpose, the authors developed a hierarchical graphical model based on multiple layers of supervoxels[1], whereas motion is assumed between neighboring supervoxels. MAP-inference of this model now yields a posterior distribution over the parameters of the image transformation. Through application of the mean-shift mode seeking [18], the authors discuss how to approach subvoxel accuracy for motion estimation. By restricting the framework to discrete optimization, a time-efficient approach is introduced, which is also resilient against local optima under certain circumstances.

In contrast to thermal imaging, CT depicts a three-dimensional modality. The patient has to be positioned in the CT device and there is no mobile version available yet. Depending on the dose, X-ray radiation also introduces harm to the human body due to the negative effects of ionizing radiation. The maximum achievable spatial and temporal resolution of CT scanners are one order of magnitude lower compared to thermal imaging. Specific tracers are further necessary in order to visualize perfusion and perfusion related disorders, depicting a clear difference to TI.

---

[1]Supervoxels combine a set of similar adjacent voxels, they can be thought of image patches.

High Resolution Intraoperative Neuroimaging

Structural Imaging   **Functional Imaging**

Flourescence Imaging   **Thermal Imaging**   Optical Imaging
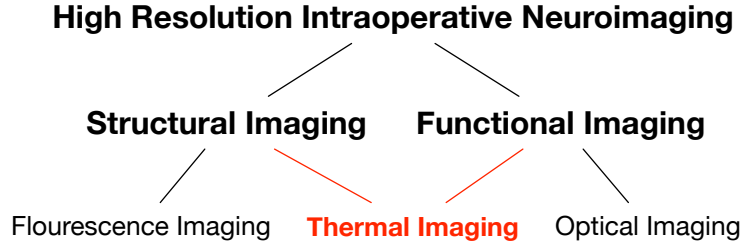
Figure 2.2.: Only a small subset of intraoperative neuroimaging techniques provide spatial resolutions lower than 1cm. Since these techniques are employed for differentiation of tissue state, sub-centimeter resolutions are required to guide tumor resections and minimize the removal of healthy tissue.

2.2. MAGNETIC RESONANCE IMAGING

The following discussion is based on [24]. Atomic nuclei have an intrinsic angular moment (nuclear spin) and furthermore have, in case of electrically charged particles, a magnetic dipole moment. By applying an external magnetic field with strength B_0 the spins align themselves parallel or antiparallel along the field lines (so-called net polarization). The ratio of parallel to antiparallel orientations follows a Boltzmann distribution. The polarization also has differing energy levels, whereas the distance between both levels linearly grows with the strength of the external magnetic field. The nuclear spin now lets the atomic nuclei undergo a precession movement, meaning they pivot around the field lines of the external field. This is called Larmor precession, yet it doesn't cause any measurable change of an arbitrary electrical unit. Therefore, an external high-frequent pulse at Larmor frequency is applied to change the orientation of the nuclear spins by 90°. This pulse also causes the nuclear spins to synchronize the phase of their Larmor precession. Larmor frequency w_0 is given by

$$w_0 = \gamma B_0 \tag{2.1}$$

with the gyromagnetic constant γ and the strength of the external field B_0. This changes the prior longitudinal magnetization into a transverse magnetization and now induces an electrical current into an external receiver coil.

Commonly, two different relaxation times are measured in order to form images of tissue. The spin-lattice relaxation T_1 denotes the time, until the longitudinal magnetization is recovered. Hereby, heat is delivered to tissue, making the tissue's thermal conductivity the strongest contributor to this relaxation time. Spin-spin or T_2 relaxation represents the time in which the nuclear spins lose their coherency. It therefore denotes the time span until the transverse magnetization has lost 63 % of its strength. MRI contrast agents increase T_1 relaxation times by accumulating at pathological tissue, for example by leaky blood vessels.

The described effect now works for a whole magnetic field, yet it doesn't yield spatial information. Therefore, three orthogonal linear gradient fields are applied to the external magnetic field, making the nuclei respond to varying Larmor frequencies. This causes the Larmor frequency to encode the spatial position and therefore allows the recording of spatially-dependent information about the nuclear spin in frequency domain (k-space). By application of an inverse Fourier transform, it is possible to recover a human interpretable representation of the imaged tissue. Recent developments regarding compressed sensing MRI decrease
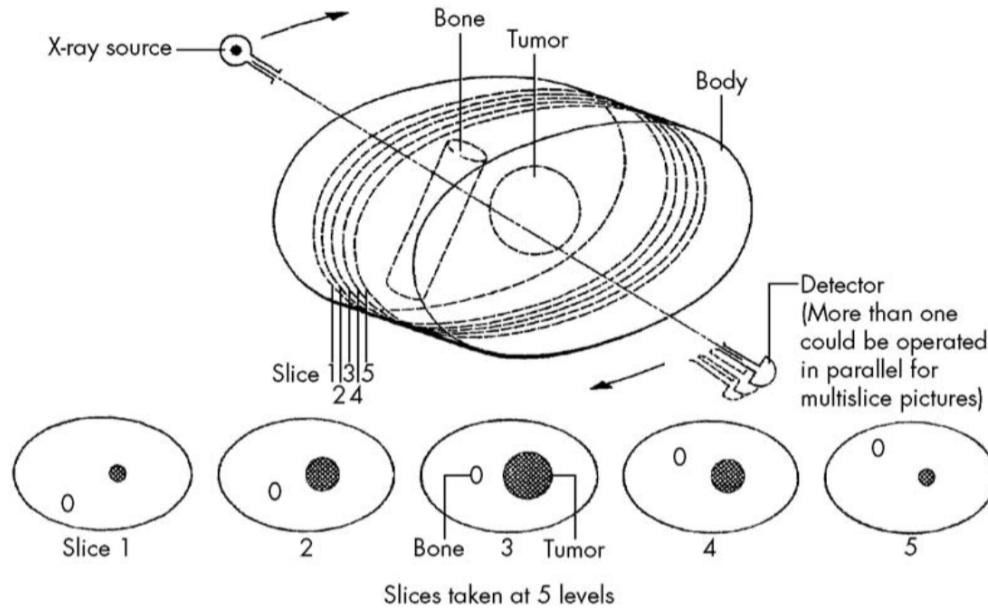
Figure 2.3.: Computed tomography works by detecting X-ray radiation with an X-ray detector at the opposing sites of the source. By combining the measurement of several such detections, it is possible to reconstruct a 3D image of any X-ray transparent object. (image source: [24])

recording time significantly and improve signal-to-noise ratio. Hereby it is assumed a sparse representation of the original MRI signal in the frequency domain exists so that it is no longer necessary to sample this space equidistantly. This comes, however, at the cost of increased computational complexity of the reconstruction algorithms. Several wavelet-based methods with sparsity enforcing constraints were discussed in [51] given 20 % subsampled raw MRI recordings. The authors found that patch-based methods minimize aliasing effects and preserve edges best compared to other state-of-the-art methods.

A statistical segmentation scheme was applied by [36] to T1-weighted MRI recordings in order to locate ischaemic stroke lesions. The authors employed a supervised naive Bayes classifier, wherein they model tissue state as independent Gaussian random variables of the combination of SPM's tissue and prior probability maps. In [30], the authors analyzed T1-weighted MRI data with respect to Alzheimer's disease. For this purpose, the authors applied a support-vector-machine (SVM) to the data and proposed a novel statistical inference scheme based on permutation testing given the estimated weight vector and margin of the SVM. A two-stage approach based on graphical models for segmentation of enhancing Multiple Sclerosis lesions in T1-weighted MRI data was proposed by [47]. The first stage consists of a voxel-level conditional random field with third-order neighborhood structure modeling a Gibbs distribution on MRI intensity values and assigned class labels. This stage yields a rough segmentation of lesions, which are then plugged into the next stage. Now, false-positives are reduced by using a second CRF with higher-order cliques on textural features. Depending on the lesion's size, the proposed method yielded sensitivity ranging from 79 % for small to 99 % for large lesions at a false discovery rate from 63 % to 7 %.

Similar to Computed Tomography, MRI is a three-dimensional modality that also requires a
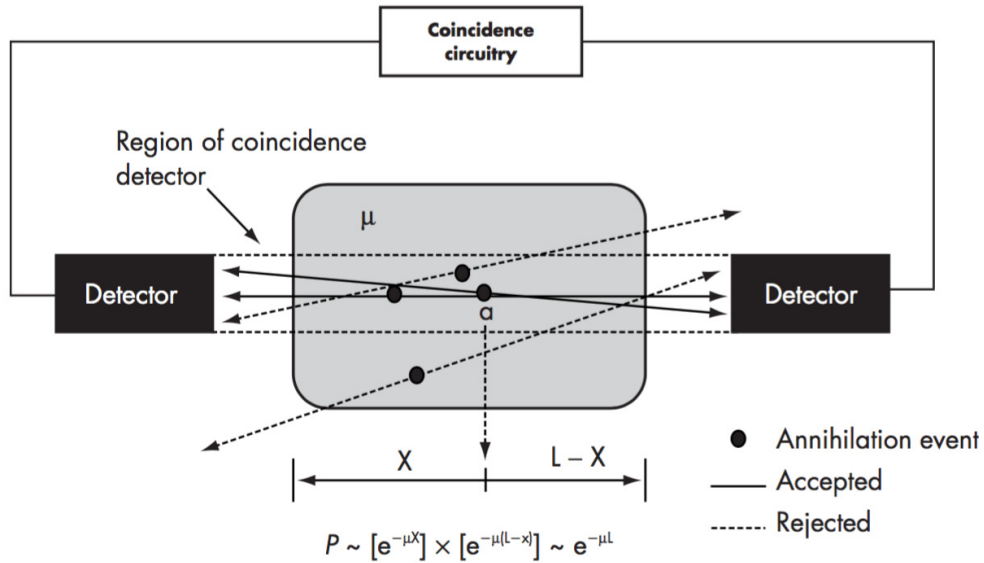
Figure 2.4.: The working principle of Positron Emission Tomography resembles Computed Tomography by the fact that particles of a linear path through an object are detected. Yet, the detected photons originate from the decay of injected atomic tracers limiting the repeatbility of PET studies. (image source: [24])

specific positioning of the patients. Due to the steadily changing magnetic field gradients, an intense acoustic burden at Larmor frequency is caused to the patient, clearly differentiating MRI measurements from passive thermal imaging. Due to current limitations of magnetic field strength, the spatial resolution of 1 mm is about 5 times higher than maximum achievable resolution of thermal imaging. This fact also limits the temporal resolution of MRI measurements.

BOLD FMRI

Blood oxygen level-dependent (BOLD) functional MRI enables the quantification of the blood oxygenation and by this yields indirect information about neural activity. Neural activity is strongly related to neurovascular coupling, which leads, amongst others, to an increase in deoxygenated hemoglobin. Two to six seconds after a neural activation, the regional cerebral blood flow leads to a further increase of oxygenated hemoglobin and decrease of deoxygenated hemoglobin [24]. Because of the differing magnetic properties of (de)oxygenated hemoglobin, it is possible to measure this behavior by a specific MRI protocol (weighted $T2^*$).

Studies have proved this correlation by comparing the fMRI results with intraoperative direct cortical stimulation [98]. Yet, Krings et al. [50] showed that the projection of subsurface signals onto the cortical surface doesn't necessarily correlate with direct cortical stimulation. Another study [111] unveiled that postoperative neurological deficits correlate with the distance between neural activity of the sensory cortex to tumor tissue. They conclude that this effect might be due to the fact that fMRI analysis yields too large an activation area since an increase of regional cerebral blood flow is broader than the actual active neurons.

Statistical parametric mapping (SPM) is a common Matlab toolbox consisting of various ap-
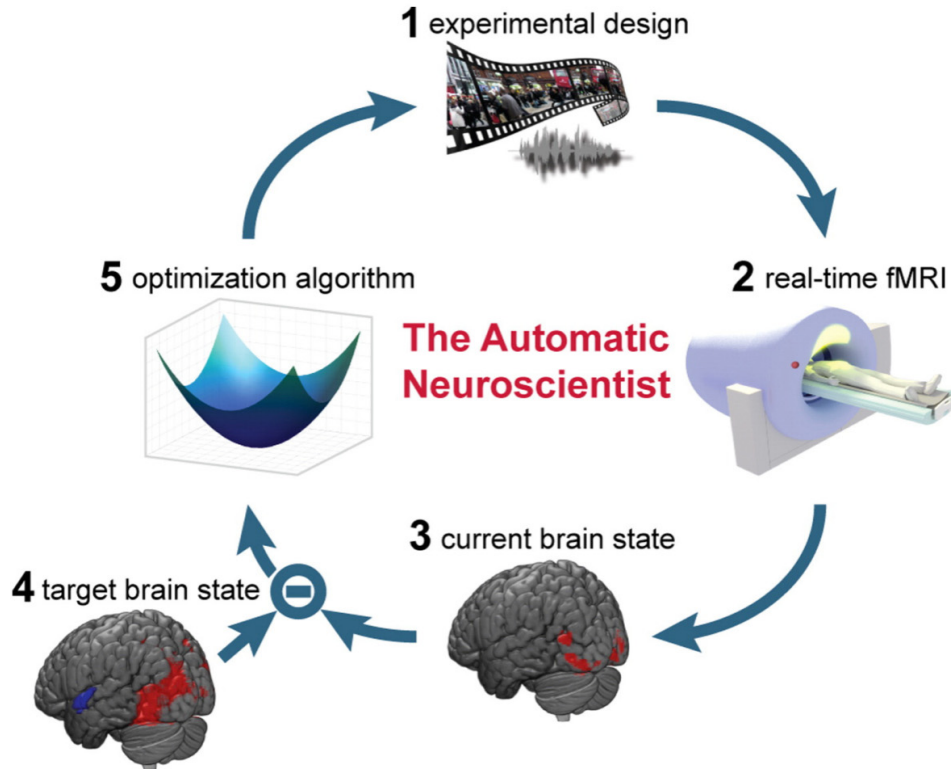
Figure 2.5.: Novel framework to optimize experimental design in order to maximize the neural activation in a pre-defined target cortical region (image source: [55]).

proaches to morphological normalization, registration, preprocessing and statistical analysis of brain imaging data (see [29] for an in-depth review). The statistical framework grounds on general and generalized linear regression models consisting of sets of deterministic components that describe the measured time series. Rest-state fMRI (rs-fMRI) is a recent development not requiring any patient interaction or deterministic components to identify eloquent areas. For this purpose, Mitchell et al. [62] applied a pretrained Multi-Layer-Perceptron neural network to low-frequency (< 0.1Hz) resting-state fMRI data and yielded a good (AUC 0.89 for motor activity, AUC 0.76 for speech) performance in localizing specific functional areas. Further advances were made by [90], who used spatially regularized SVMs for analysis of rs-fMRI data. Similarity encoding techniques such as Representational Similarity Analysis (RSA, see [49], [65]) are another novel approach for classification of brain imaging data combining multivariate statistics and machine learning. RSA-based inference depends on analyzing the similarity of the spatial activity pattern of experimental conditions in a specific region of interest [65], in contrast to testing the occurrence of an actual activation pattern in a time-series as done by regression-based methods. Another novel application for identification of functional network in fMRI data was demonstrated by [57] using sparse coding. The general idea is to represent the fMRI dataset in terms of linear combination of the elements of an over-complete dictionary which is to be learned dictionary by imposing sparsity (L_1) constraints to each element's coefficient. The latter minimizes the number of chosen elements to represent the fMRI signal. Experimental task-related elements of the dictionary

14

are then unveiled by analysis in time- and frequency domain. Stacked auto-encoders are another modern approach to unveil functional networks by recovering non-linear dependencies among input data. This approach was demonstrated by [95], who used multiple Restricted Boltzman Machines (RBM) to model non-linear behavior of input data. Linear RBMs can be thought of unsupervised feed-forward neural networks without inter-layer connections that approximate an input signal by a hidden layer of arbitrary dimension. A lower dimensional hidden layer leads to a projection into a subspace (in case of linear RBMs and a single hidden layer: onto the first principal components [16]). RBMs first *encode* the input given the model's weights, and afterwards *decode* it by using learned output weights. These weights are used as a compressed representation of the initial signal for a subsequent classification by a Hidden Markov Model. The authors demonstrated the applicability of their approach to classify Mild Cognitive Impairment at a diagnostic accuracy of 72.58 % on ADNI2[2] cohort. This performance is also superior to the accuracy of other state-of-the-art methods. The authors also evaluated the impact of the proposed Deep Autoencoder and found the necessity of learning non-linear relationships, since linear methods such as PCA yielded below-average results. The usage of a Gaussian mixture distribution for MCI classification also yielded a worse performance than the proposed HMM.

Automatic neuroscience was first demonstrated by [55]. The proposed method automatically optimizes the experimental conditions of real-time fMRI recordings in order to maximize neural activity at target cerebral sites (see figure 2.5). This was achieved by parametrizing the experimental space and traversing it by local optimization methods. It was found that non-parametric Bayesian optimization allows the whole parameter space to be sampled by using reasonable model assumptions such as flat priors. This work may further improve understandings regarding functional connectivity and accuracy of brain mapping.

BOLD fMRI is a technique to monitor neural activity by recognizing the BOLD contrast induced by neurovascular coupling. This allows to visualize the neural activity more directly than by using intraoperative thermal imaging. BOLD fMRI also provides depth maps of neural activity at spatial resolutions as low as 1mm. Yet, the same disadvantages of MRI also apply to BOLD fMRI, making it a less favorable solution for intraoperative imaging.

DIFFUSION TENSOR IMAGING

Diffusion tensor imaging (DTI) is based on MRI. After the transverse magnetization, a so-called diffusion weighting is applied. This means another gradient field of a specific orientation is applied to the external magnetic field. Atomic nuclei now precess at a varying Larmor frequency and become incoherent. Then, a 180* HF-pulse followed by the same gradient field is applied to the magnetic field. The nuclei's magnetic dipoles become phase-synchronous and induce characteristic electrical current into the receiver coil. This current is lower than the current of a plain MRI measurements, since some nuclei might have moved during the application of the second HF-pulse and the two gradient fields. This movement correlates with the diffusion movement of the nuclei. Thus, the weaker electrical current also correlates with the diffusion movement. By varying the gradient field, it is now possible to estimate a voxelwise 3×3 tensor and therefore visualize the flow direction of hydrogen molecules [24].

The evaluation of characteristic tissue perfusion properties now delivers valuable information

---

[2]The dataset is available at http://adni.loni.usc.edu/data-samples/.
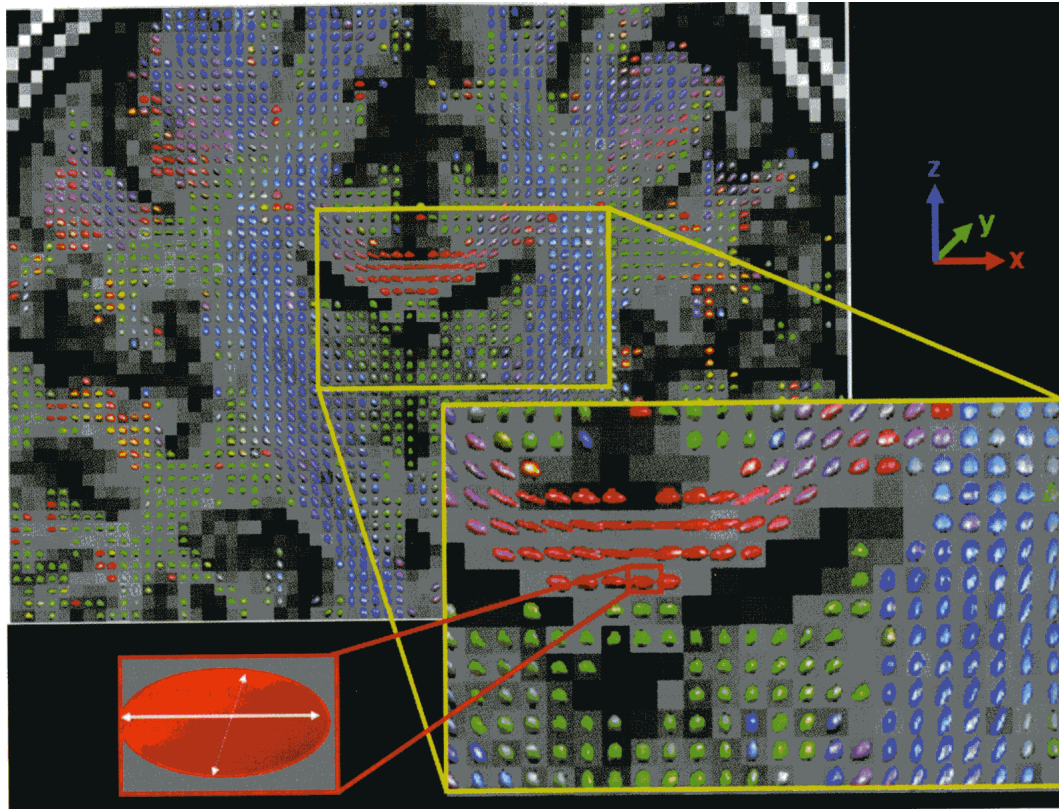
Figure 2.6.: Diffusion Tensor Imaging is a sort of MRI study providing information to localize nerve fibers. (image source: [105])

in neurosurgery, especially since it is now possible to recover nerve fascicles (so-called fiber tracking) and, in particular, to visualize diffuse axonal injuries [83] as well as white matter pathologies in general. DT-MRI provides the possibility to reconstruct the nerve pathway within the brain as well as the the analysis of white matter [22]. [13] discussed a non-parametric statistical approach to further improve the quality of fiber mixtures. The authors used a regularized Nadaraya-Watson estimator with Gaussian kernel and matching-based distance measure. By integrating the fiber information into neuronavigation systems, it is possible to lower the risk of harming the pyramidal tract during tumor resection (see for example [68]). Another recent development of DTI is white matter abnormality mapping [10] based on Voxel Based Analysis [3]. For this purpose, Booth et al. aligned and computed the Mahalanobis distance of template cortical perfusion- and subject data. Since this distance measure follows an χ^2 distribution, significance testing is straight forward. With this method, the authors were able to correlate spatial extent of estimated abnormality with white matter lesions as well as neurodevelopment outcome.

2.3. POSITRON EMISSION TOMOGRAPHY

Positron emission tomography (PET) scanners detect photons which originate from the atomic decay during the annihilation of positrons and electrons. The annihilation of these two elements yields two photons at 511 keV [2] that fly in opposite directions. To provoke this event,

biomolecules containing such a tracer are injected into the venous system of the patient and accumulate at characteristic sites, for example in liver tissue as well as in pathological tissue with increased metabolism. It then interacts with electrons and initiates the process just discussed. A PET scanner consists of an axial detector design to catch both opposed photons and correlate them in order to infer their distribution in the scanned body. [24]

The mathematical background is similar to CT since the detectors also measure the integral of photons over a linear path. Prevalent systems have a resolution of 5 to 8mm and are prone to noise. One typical recording takes approx. 90 minutes. Current devices combine CT/PET in order to combine structural information with hemodynamics and nutrition consumption. These devices have a resolution of 4 mm and take 15 minutes per recording.

PET scanners mainly allow the visualization of variation in the body's glucose distribution (FDG-PET, F-flurodeoxyglucose) and changes in regional cerebral blood flow ((15)O-water PET). In 1930, Otto Warburg found that tumor cells consume lots of glucose, making FDG-PET a promising tool for tumor diagnostics. (15)O-water PET enables monitoring the regional cerebral blood flow to be possible and therefore it is also possible to quantify cortical hemodynamics and - analogously to fMRI - neural activity. Studies have shown that PET scanners are rather inaccurate at detecting neural activity, since the focal center of the activity appears to be shifted by 1 cm and false-positives are measured that don't correlate with results of intraoperative direct cortical stimulation [43]. [53] reported a diagnostic sensitivity of 44.3 % in a cohort of 89 patients with refractory partial epilepsy for the localization of the epileptic lobe by FDG-PET. This may correlate with the findings of Wetjen et al. [107], who found that hyper-perfused areas at the sites of previously failed epileptic resection sites do not necessarily correlate with epileptic lobes. In order to classify Alzheimer's disease, [69] used bagged linear SVMs with recursive feature elimination [25]. Applying their method to FDG-PET data yielded an AUC 0.709, whereas multimodal fMRI-PET analysis increased AUC to 0.748. Their analysis also showed that unimodal FDG-PET and fMRI performance is comparable in terms of analyzing gray matter. Subsequent PET recordings can also be used for tumor growth analysis in order to evaluate the therapeutic treatment plan as suggested by [61]. For this purpose, the authors first developed a tumor growth model for consecutive FDG-PET scans of a single patient during radiotherapy. The model is initialized by providing a manual tumor delineation as boundary condition for the first two recordings. Tumor segmentation and mass computation of subsequent PET scans is then achieved by iteratively evaluating a Dirichlet distribution on PET intensity values and the growth model's predictions of the likely delineation for the to-be-evaluated recording. Hereby, the authors were able to achieve average volume concordance of 73.17 % between automatic and expert tumor segmentation. PET requires the application of radiopharmaceuticals (RN) that emit positrons. An extensive discussion of current tracers can be found in [2]. The measurement of this effect is delayed since the tracer has to distribute in the patient's cardiovascular system and accumulate at specific positions. The RN's half-life time and potentially harmful ionizing radiation also prevent rapid repetitions of a study. By a spatial resolution of about 3 to 5mm [24], PET scanners are furthermore less sensitive than thermal imaging by a factor of ten. A clear advantage of PET scanners is their ability to measure perfusion as well as the glucose distribution of a body, enabling good visualization of tumorous tissue - yet at worse spatial resolutions. It is further possible to quantify the neurotransmitter function of the brain (like Dopamin), which is useful for neuropsychological experiments. Since PET scanners allow regional cerebral blood flow to be quantified, it is also possible to establish functional imaging. Due to the half-life time of the

RNs[3], long study durations for this kind of experiments are required. In contrary to thermal imaging, there is no intraoperative application of PET.

2.4. SINGLE PHOTON EMISSION COMPUTED TOMOGRAPHY

SPECT is operationally similar to PET and also requires the application of a nuclear tracer. Due to physiological and optical reasons, the tracer's energy must lie between 100 keV and 200 keV. One common tracer is Technetium-99m ((99m)Tc). The tracers accumulate in human tissue and emit gamma radiation. Gamma radiation also introduces ionization radiation, which may cause "harmful biological effects" [26]. A scintillation detector now measures the emitted gamma radiation. One or more detectors rotate around the body and measure the gamma radiation. But unlike PET, scattering effects may influence the pathway of the photons (gamma rays) and their energy might also change due to absorption effects. Since a collimator is necessary to get directional information from incident photons, additional uncertainty is introduced about the origin of the measured photons. After recording the information, the same mathematical methods as with CT and PET are employed - filtered back-projection and iterative reconstruction.

The actual use-case of SPECT strongly depends on the applied tracer. By using the highly inert (133)Xe gas or (99m)Tc it is possible to quantify the regional cerebral blood flow, allowing - just like fMRI and PET - the evaluation of neural activity. (201)Tl can be used for tumor diagnostics [26].

A recent study that compared PET and SPECT argued that PET's sensitivity is "two to three orders of magnitude" higher than SPECT's mainly because of its need to use a collimator [72]. Analogously to PET imaging, a radionuclide is required for SPECT measurements yielding comparable disadvantages. Compared to PET, SPECT is limited to blood flow analysis and measurements of neurotransmitter function. Theoretically, functional imaging is possible by SPECT imaging, yet (99)m Technetium has a half-life time of 6 hours allowing only studies with one image per day [24]. [27] compared the localization abilities of MRI and SPECT for patients with focal dysplastic lesions (FDL) by analyzing thresholded normalized (Z-score) co-registered differential interictal-ictal SPECT recordings. They found that multimodal subtraction SPECT with MRI imaging (SISCOM) achieved a discovery rate of 47 % for FDL localization. They also discovered that FDL overlapped with 16.5 % the size of the found cluster as suggested by SISCOM imaging. Similar findings were reported by [53], who report 41.1 % sensitivity of subtraction SPECT imaging for the localization of epileptic lobes.

Several studies analyzed SISCOM data by using newly developed frameworks (for example [27], [107]), yet the reference framework of fMRI, Statistical Parametric Mapping, was also extended for analysis of SPECT imaging data. Table 1 of [100] lists several common techniques for analyzing SPECT data.

2.5. NEAR-INFRARED SPECTROSCOPY

Near-infrared spectroscopy (NIRS) is a non-invasive transcranial method to detect photons of the near-infrared spectral range (650 - 960 nm). These wavelengths contain (amongst

---

[3]The tracer (15)O has a half-life time of 2 minutes, which allows a certain extent of functional imaging, yet for each session it is a requirement that the tracer must be absorbed.

others) characteristic spectroscopic bands of hemoglobin, allowing information about its oxygenation state to be inferred. This yields the same potential as fMRI for acquiring information about the regional cerebral blood flow. Technically (functional)NIRS is comparable to infrared spectroscopy, meaning that it causes molecular vibrations by near-infrared radiation. These vibrations allow a detailed characterization of molecules and their bonds [67]. [19] compared BOLD fMRI and fNIRS measurements of (de)oxygenated hemoglobin and found a significant correlation between the time behavior of these tracers in both modalities.

A meta-study regarding functional NIRS imaging demonstrated the applicability to recover neural activity. Yet, there is room for improvement in terms of spatial and temporal resolution compared to fMRI and general image quality [67]. This also segregates fNIRS from thermal imaging, since former images are blurry and this technique only achieves comparatively bad spatial resolutions. Yet, (f)NIRS depicts a non-invasive method, allowing images of anatomic structures and functional information of the cerebral cortex to be acquired. The latter was demonstrated by [86], who used preprocessed NIRS data of (de)oxygenated hemoglobin of the left and right motor cortex as a foundation for a brain-computer interface. They classified the concentration value of hemoglobin by a SVM and a pre-trained 5-state Hidden Markov Model (HMM). The SVM achieved 73.1 % accuracy in a motor imagery task, while the HMM yielded a striking performance of 89.1 %. Guillermo et al. [37] established a brain-computer interface based on fNIRS using support vector machines at an overall accuracy of 76.30 %, allowing communication with a patient suffering from complete locked-in syndrome. In a comparative study regarding the classification of a binary decision (yes, no), [64] demonstrated a good performance of support vector machines (accuracy 82.14 %) compared to linear discriminant analysis (accuracy 74.28 %). Prior to these results, [109] published the possibility to analyze fNIRS data using an extension to statistical parametric mapping for task-related study designs.

2.6. ELECTROENCEPHALOGRAPHY

In neurology, electroencephalography (EEG) is the gold standard method for non-invasive measurement of the brain's electrical activity. EEG requires the placement of electrodes on the patient's head. These electrodes are connected to an electrical amplifier allowing the derivation of current variations over time. Typical amplitudes are approximately ± 100 mV [24]. These variations are caused by the extracellular current flow, which correlates with excited and inhibited postsynaptic potentials (IPSP, EPSP). It is important to note that IPSP and EPSP differ from the action potentials of neurons, since action potentials wander around axons and lead to a release of neurotransmitters. The neurotransmitter now activates a receptor of the adjacent (postsynaptic) neuron. The described process is also known as neurotransmission. This activation induces an electrical current that is measured by EEG [24].

Electrodes are a coarse-grain way of measuring electrical current, since they are several orders of magnitude larger than a single neuron. Therefore, the electrode measures the integrated electrical current at its contact area to the head. Common EEG bands are defined by the frequency range they cover. In detail, there are Delta (< 4 Hz), Theta (4 to 8 Hz), Alpha (8 to 13 Hz) and Beta (>13 Hz) bands. Each allows specific inference about pathological changes.

A common application of EEG is the detection of epilepsy related seizures, which typically induce distinct spikes into the recorded data. Other pathologies (such as lesions) also introduce characteristic patterns into the EEG signal, yet its use for this kind of pathology has
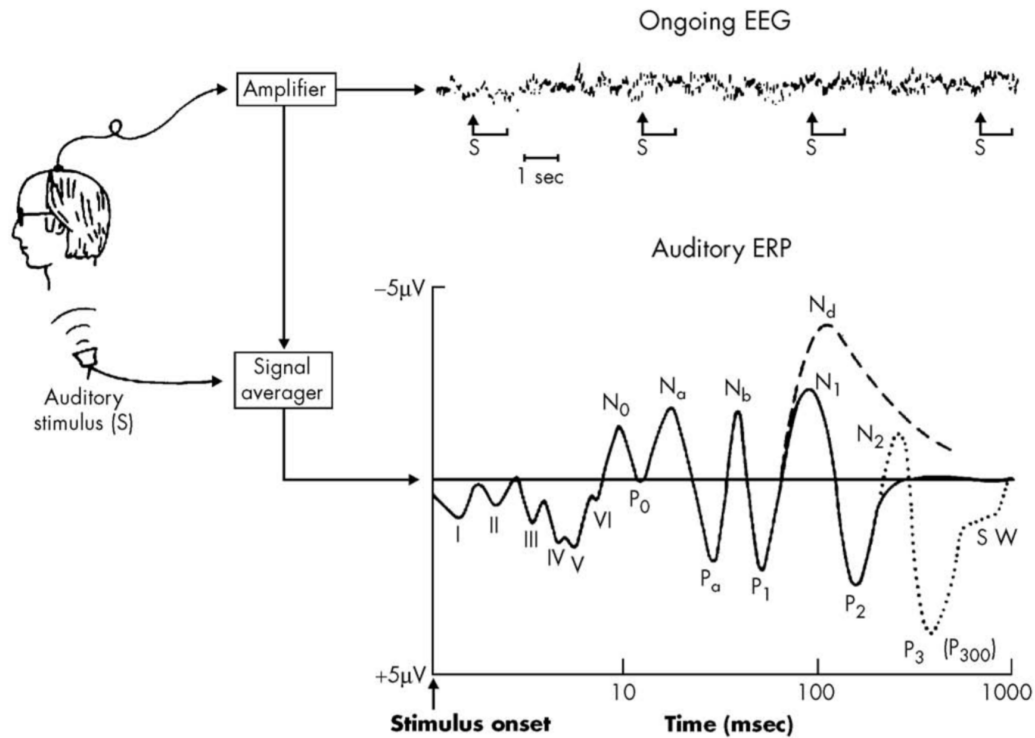
Figure 2.7.: Electroencephalography (EEG) is a non-invasive method to measure electrical activity of the brain by placing electrodes on the patient's head. In the upper part, the online EEG during auditory stimulation is seen. After multiple repetitions and signal processing, the response of the auditory system can be recognized as seen in the lower part. (image source: [24])

declined since the advent of imaging techniques with better spatial resolution like MRI or CT. Another application of EEG is the visualization of brain connectivity, meaning the disclosure of interaction between (groups) of neurons. For this purpose, [8] demonstrated an online method for single-trail connectivity analysis. The authors fitted a L_2 regularized vector autoregression (VAR) model jointly with an Independent Component Analysis on EEG data as of [7]. Afterwards, streaming EEG data is decomposed continuously into independent components by the gained unmixing matrix. By fitting a VAR model to this decomposed data, a causal relationship and therefore a representation of connectivity can be visualized (see [79] for details). Non-linear time-series analysis was applied to EEG measurements by [92]. From the measured EEG electrode's time-series, the parameters of a Lorenz attractor are reconstructed. This attractor describes the time-series behaviour in state space and is quantified by its embedding dimension (size of state vector) - and in the case of time-delay embedding - the lag used for constructing the state vector. Each state vector can be though of as a single point of the attractor's trajectory in state space. A characterization of this attractor (for example by Lyapunov exponents or Poincaré section) now allows the quantification of dynamic time behaviour of the data. The authors review several applications and argue that it might be useful for predicting and detecting epileptic seizures because of their highly non-linear nature.

2.7. MAGNETOENCEPHALOGRAPHY

As a consequence of the extracellular current flow (see EEG), the human's head is surrounded by a magnetic field. Measuring this field might allow the analysis of neural activity as is done by EEG [24]. Yet, sensitive superconducting quantum interference devices (SQUID [17]) are necessary to actually measure it, since the magnetic field's strength is at picotesla scale [104]. Note that the earth's magnetic field is at 0.5 mT and urban magnetic noise is just below 1 nT [104]. Therefore, very accurate noise correction and signal estimation schemes are required in order to differentiate neural activity from environmental noise.

The SQUID detectors are installed into the helmet array (dewar) just discussed. The patient now places his head into this fixed helmet but he can still move his head a little bit. This makes it necessary to employ registration techniques for motion compensation for efficient image fusion with other modalities such as EEG or structural imaging methods [104]. State-of-the-art is the integration of 275 SQUID detectors into the just discussed helmet array. This number of detectors allows finer scales and provide the ability to evaluate the communication patterns between adjacent groups of neurons.

MEG is currently employed for localizing epilepsy and non-invasive monitoring of sensomotory activity [24]. On synthetic MEG data, [97] simulated event-related potentials (ERP) in order to demonstrate the abilities of LDA beamformer to unveil the potentially correlated electrical source signals of neural activity given their assumed spatial distribution (map). The authors propose to employ a regularized scheme to estimate covariance matrix as solution to the LDA optimization problem. Hereby, they were able to recover the source signal at highest SNR compared to PCA and linear-constrained minimum-variance beamforming [101]. Yet, it has to be emphasized that the abilities of the method directly depends on the accuracy of the spatial map estimation scheme.

2.8. INTRAOPERATIVE IMAGING

Until now, we discussed methods to extract structural and functional information using pre- or postoperative methods. This information is then employed for surgical planning and as medical decision support, for example in the case of localizing aneurysms, tumor or brain mapping. In this section, we discuss intraoperative structural and functional imaging techniques that yield direct feedback to the surgeon regarding the desired information.

2.8.1. ULTRASONOGRAPHY

Ultrasonography (US) is a method to examine tissue structures and blood flow by ultrasound waves. US is regarded as safe method, since it just generates heat in the evaluated tissue and might lead to cavitation. Ultrasound waves with frequencies in the MHz range are emitted and their echo is received by a flexible probe (transducer). A transducer converts ultrasound waves via the piezoelectric effect. Incident ultrasound waves transmit through a crystal and are converted into an electrical current (Piezo effect). Contrary, in order to generate ultrasound waves, high-frequent alternating voltage stimulates this crystal to oscillation, raising ultrasound waves [45].

Impedance denotes a certain amount of acoustic resistance, which slows down the propagation of ultrasound waves. Tissue properties directly influence its impedance introducing characteristic properties to the acoustic signal. Pulses of US signals are sent to an object
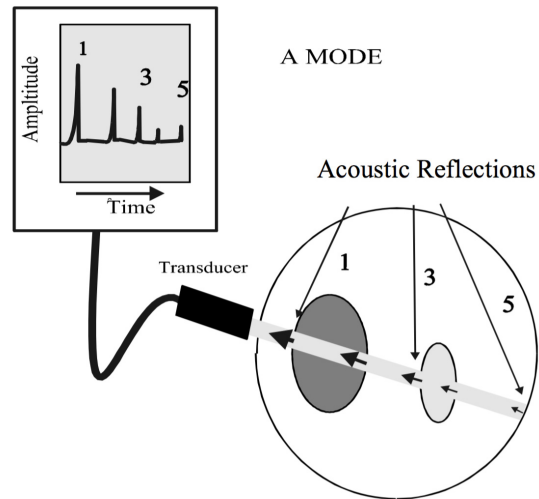
Figure 2.8.: A transducer emits acoustic waves and records their reflections. The time-of-flight of these reflections correlates with tissue properties which allows the structure of the examined tissue to be acquired as an image. (image source: [38])

and permeates it to some degree - depending on the tissue's structure and composition. The signal now echoes off the tissue and returns to the probe. The runtime of the US signal's echo correlates with the penetration depth and its amplitude with the tissue's composition [45]. Because of impedance, it is not possible to measure the surface of objects, since the transition between different materials (air, tissue) causes a high impedance, resulting in weak to no echos.

B-Mode-imaging is an extension to conventional US by the application of a linear array of transducers to scan multiple positions in parallel. The resulting data is a two dimensional representation of the object. Doppler-US computes the phase shift between sent and received US and therefore allows the visualization of flows, for example blood flow [45]. In [21], the authors discussed the influence of anisotropic 4D (three spatial and one temporal dimension) ultrafast Doppler imaging for cerebrovascular imaging. For this purpose, a linear scanner array was translated and rotated at consecutive positions at respective angles. Since the pixel dimension increases in an out-of-plane direction of the propagating plane wave of the employed 1D linear scanner array, anisotropy is introduced into the data. By simulating the 3D point-spread-function and plugging it into a Wiener filter, the authors significantly improved the in-plane resolution as demonstrated on synthetic and animal experimental data leading to spatial isotropy. Further studies have shown that intraoperative US can be employed to find tumor lesions [99]. The integration of 3D ultrasound systems with neuronavigation systems provides additional use to the surgeon for guided resection procedures [81].

Ultrasound introduces several challenges to image analysis tasks. This is due to the fact that the images are prone to speckle noise, intensity fluctuations and physically connected components can appear disconnected in US data because of some parts not reflecting the US signal, leading to so-called shadows. One approach to these challenges was discussed in [76], wherein the authors recovered structural information of fetal US imaging data. They proposed to combine a rough fuzzy-connectedness based image segmentation scheme with subsequent refinement step by exploiting structural information. The latter was achieved by

comprising shape information to the previously segmented objects to improve object delineation in the case of shadows. For this purpose, they extracted local curvature information of the objects convex hull and for each point of its boundary an inwardly pointing normal. By measuring the intersection of the normal with the object's inner boundary, they computed its width and were able to locate gaps. These gaps are filled by connecting the normals at both sides leading to closed objects. It has to be emphasized that this approach assumes that a single object which may be prone to gaps is segmented. However, their approach reached an average sensitivity of 87.3 % and specificity of 97.05 % wrt. expert segmentation.

Intraoperative US enables 3D imaging of anatomic structures and blood flow. Yet, as discussed and contrary to thermal imaging, it is not possible to analyze cortical structures. Intraoperative US recordings further require the surgeon to pay attention that no air is enclosed between the US probe and tissue for acquisition of high-quality three-dimensional data sets. It is furthermore not possible to visualize functional activity by this method. Inherent speckle noise, heterogeneous image intensity distributions and object discontinuities require advanced image analysis methods in order to reach a reasonable performance.

2.8.2. INTRAOPERATIVE MRI

The mechanical forces that occur during trepanation and resection cause structural changes in the elastic brain tissue during OP. This effect is denoted by brain shift. In navigated surgery (see section 2.9) this unwanted effect increases the deviation between preoperative MRI recordings and the actual intraoperative tissue structure. Brain shift increasingly invalidates the advantages of navigated surgeries overtime and has to be corrected. One approach to solve this issue is by employing intraoperative MRI (iMRI). IMRI allows the intraoperative acquisition of MRI datasets. However, the surgery has to be interrupted in order to update the preoperative MRI dataset with a new intraoperative recording. Currently there are two main approaches to intraoperative MRI:

1. Acquire the MRI dataset in an adjacent and specially prepared room [108]

2. Acquire the MRI dataset in the operating room [63]

The first approach requires the patient to be brought into another room and then for the MRI dataset to be transferred into the neuronavigation system. This approach also requires the patient registration procedure of neuronavigation systems to be repeated, and therefore further delays the OP. Automatic image fusion approaches (see for example [77]) were proposed, yet are not robust enough for general intraoperative usage. The second approach requires special attention to the used surgical tools, since they are not allowed to be magnetic. Recording an MRI dataset without being forced to move the patient minimizes intraoperative delay and enables a seamless integration of new data into intraoperative neuronavigation system. The latter approaches lower the delay between acquisition and integration of the MRI dataset into the neuronavigation system [45]. Independent of the actual approach to intraoperative MRI, the surgical intervention has to be interrupted, the patient must be positioned in an MRI scanner, and any magnetic instruments have to be removed from the patient. After acquisition, the patient must be re-registered (potentially semiautomatic) to the MRI dataset. This requirement delays surgical procedures and limits the number of repetitions of intraoperative measurements.
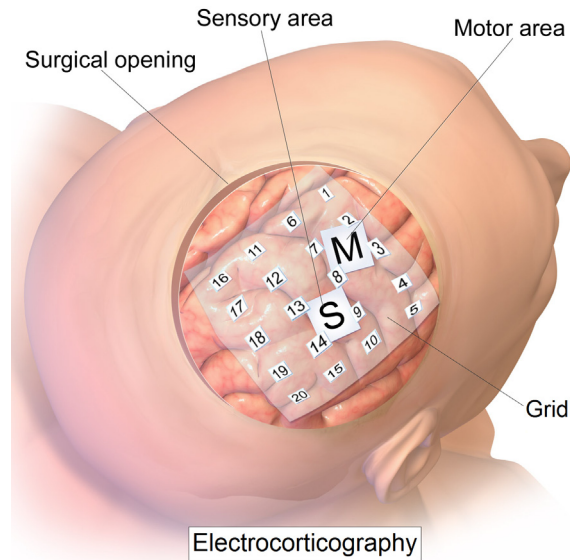
Figure 2.9.: Electrocorticography requires the placement of a sterile electrode grid directly onto the cortex during neurosurgical interventions. Hereby it is possible, to measure electrical activity of neurons at very high temporal resolutions to infer the position of e.g. eloquent areas. Despite its high temporal resolution, the electrodes of the grid limit the spatial resolution of this technique to cm range. (image source: [9])

2.8.3. ELECTROCORTICOGRAPHY

Electrocorticography (ECoG) denotes a technique similar to EEG. A sterile electrode grid is placed on the exposed cortex and the electrical current is measured. The underlying origin of the current is the same as in the case of EEG, yet the signal is much stronger, since it is not getting attenuated by the patient's skull. ECoG devices typically have a temporal resolution of 5 ms and a spatial resolution of about 1 cm [80].

The main usage of ECoG is the localization of eloquent cortical areas as well as the center of a focal epilepsy. ECoG depicts the gold-standard for intraoperative measurements of cortical and subcortical neural activity. However, this method requires the placement of electrodes onto the cortex, resulting in spatial resolutions in cm range, which is a factor of 1000 worse than the achievable resolution of thermal imaging. Therefore, ECoG is generally employed for measuring neural activity, especially in the case of locating epileptic foci, yet since it doesn't provide anatomic information, lengthy repetitions are required for precise differentiation of focal lobes of neural activity to other tissue. [31] used ECoG signals for the detection of epileptic foci. The ECoG signal was projected into time-frequency domain by Wavelet Packet Transform. Since this yields an over-complete representation of the signal, they applied a best-basis transform to get a compact representation. By application of the identity penalty function $G_E(x) = G_W(x) = x$ a correspondence matrix is computed, which is plugged into PCA. The scores of the three principal components are then visualized. The geometric properties of the resulting three dimensional structures (dimensionality, symmetry) now allow the exploration of corresponding signals.
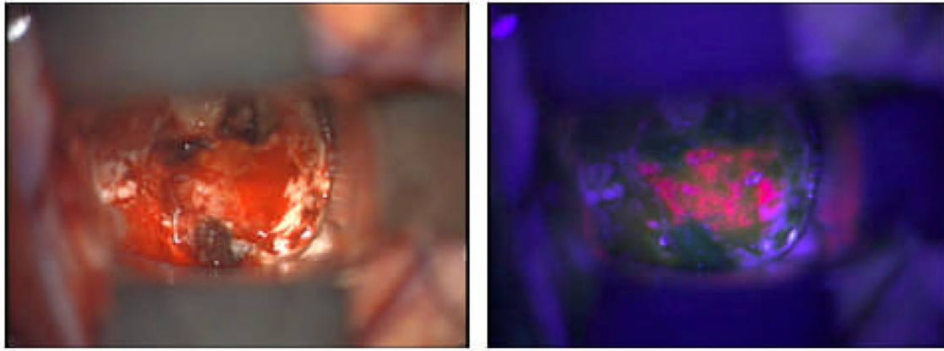
Figure 2.10.: The left subimage shows an intraoperative recording of the microscopic image of a glioma. Using flourescence imaging and the application of a tracer. The right image shows flouscenting tumor tissue caused by ALA-PpIX. (image source: [71])

2.8.4. DIRECT CORTICAL ELECTRICAL STIMULATION

Direct cortical electrical stimulation (DCES) is done in parallel with ECoG. The surgeon uses a bipolar electrode to apply an electrical pulse to a specific part of the cortex. As a result, inhibited and excited neurons are activated. In fact, there is also a chance that this procedure also activates remote sites. The pulse strength is 0.5 to 10 mA at a pulse width of 0.3 ms for approximately 2 to 5 seconds [80].

This technique is used for brain mapping (for example language processing tasks, sensormotory cortex), since the activation can be evaluated directly. For example stimulating a specific part of the motor cortex leads to movements of the patient's hand. Another important application is a coarse-grain differentiation of tumor to healthy tissue by stimulating the cortex. It is expected that tumor tissue shows abnormal or no behaviour following an electrical stimulation [80].

2.8.5. FLUORESCENCE IMAGING

Fluorescence denotes the effect that a material emits photons after it is excited by photons of different wavelengths. Autofluorescent materials react to photons without the application of external agents. In the medical domain, florescence is provoked by the application of an external tracer that accumulates in specific types of tissue, for example in tumor tissue. By external excitation with photons, electrons of the tracer are promoted from their ground state S_0 to a state of higher energy S_1. Since matter wants to reach a state of minimal energy, a relaxation process is initiated, wherein photons are emitted. These photons can now be detected. The Stokes-Shift states that the wavelength of the excitation source is lower (higher energy) than the wavelength of the emitted photons (lower energy). In neurosurgery, typical agents are Indocyangreen (ICG) for videoangiography and perfusion analysis and 5-ALA. The latter accumulates in tumor tissue [4].

There are various approaches to intraoperative fluorescence imaging, such as epiflourescence, spectral flourescence imaging, confocal microscopy, two-photon microscopy. Epiflourescence is commonly employed in OP microscopes, for example in Zeiss microscopes. The target gets illuminated through the objective. Lamps with high luminosity are required for this technique, for example Xenon gas discharge lamps. These lamps typically emit pho-

tons of a wide spectrum, whereby it is possible to narrow down the spectrum by the usage of specific bandpass filters appropriate for the excitation spectra of the used agent. By the application of dichromatic mirrors, the excitation light gets coupled into the beam path of the microscope. This doesn't affect the imaging of the fluorescence emission, since the dichromatic mirror works like a spectrally selective beam splitter. Reflected excitation light of the surface gets forwarded to the light source and the surgeon just sees the tissue's fluorescence pattern. The usage of an emission filter of appropriate bandwidth may further improve the visual quality of this fluorescence pattern. Importantly, fluorescence imaging allows a submicrometre resolution [4].

Current research shows promising results for handheld confocal endomicroscopy with NIR light sources in combination with ICG. Hereby, it is possible to visualise the tumor demarcation and histological details. NIR further allows better penetration depths (350 μm). This technique provides microhistological information about tumor cells in vivo. This provides valuable information about healthy, tumorous and transitional tissue [58].

There is further ongoing research regarding targeted tracers aiming to improve target specific kinds of tissue for fluorescence imaging. Nano particles (for example quantum dots) provide features allowing a more specific binding to tissue to occur. They might be coupled to proteins, fatty acids or other compounds that mostly accumulate in tumor tissue and therefore improve the sensitivity in the detection of the tumor's demarcation.[54]

In contrast to thermal imaging, fluorescence imaging requires a tracer to highlight specific effects and structures. At high doses - above FDA limits - the used tracers also introduce toxicity [4]. Due to the half-life time of the employed tracers, a delay of several minutes to hours is required for repeated measurements. Depending on the employed microscopes, FI yields good temporal- as well as spatial resolutions in the μm range. This technique allows differentiation of specific tissues as well as perfusion monitoring to be established, for example by the application of 5-ALA or ICG. Compared to thermal imaging, functional imaging is not possible and tumor differentiation requires tracers that mostly accumulate at sites of tumor cells.

2.8.6. OPTICAL IMAGING

Optical imaging can be used for the measurement of light absorption and light scattering. The former provides the necessary tools to inspect the occurrence of specific chemicals whilst the latter can be used to analyze physiological characteristics.

Functional activity of neurons leads to variations in a cell's water balance. [39] state that the blood flow and blood oxygenation changes during neural activity. Action potentials lead to local changes in both blood flow and oxygenation, which may allow us to draw conclusions regarding neural activity[75]. Neurovascular coupling denotes the correlation of neural activation with an increase of regional cerebral blood flow. This bases on the assumption that cellular processes of neurons require glucose and oxygen to function properly. In the case of neural activity, the neurons have an increased demand for glucose and oxygen which must be satisfied by an increased regional cerebral blood flow. This demand is over-fulfilled, leaving additional glucose in the blood and in tissue [98].

Optical imaging quantifies the oversupply of oxygen, since this changes the ratio of Oxyhemoglobin (HbO_2) and Deoxyhemoglobin (Hb). Both molecules absorb light differently, making it possible to monitor their ratio over time. In the case of neural activity, this ratio gets changed significantly (see figure 2.11) allowing the localization of active areas or epileptic seizures of the cortex [98]. In 2013, the detection and visualization of somatosensory
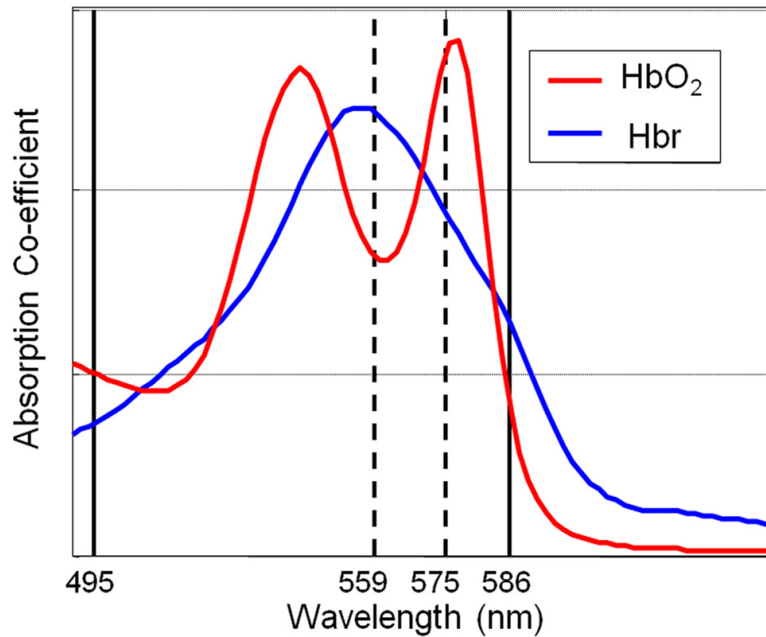
Figure 2.11.: Plot of the characteristic absorption spectra of Oxyhemoglobin (*HbO$_2$*) and Oxy-hemoglobin (*Hbr*). (image source: [6])

evoked potentials [88] and visual function [89] was demonstrated by thresholding the normalized power spectrum at stimulation frequency $\frac{1}{60}$ *Hz*. In the very common case of spatially correlated noise, [91] discussed the suboptimality of the former approach and applied generalized indicator function analysis to IOI data to detect periodic signal components among correlated noise.

[52] modeled the time course of a pixel by state-space equation accounting for smoothly varying functional responses and periodic components (heartbeat, respiration). By using a state-space model, the authors allow for dynamic parameter evolution over time, yet at the cost of an expensive Markov Chain Monte Carlo estimation of the model's posterior probability distribution. Another suggested maximum likelihood estimation scheme was too sensitive to the starting condition and didn't converge to a global optima. Since Optical Imaging integrates seamlessly into OP microscopes, it achieves good spatial and temporal resolutions. By visualizing BOLD effects, it is further possible to recognize neural activity by neurovascular coupling. Intraoperative OI therefore yields anatomic/structural as well as functional information of the cerebral cortex. Like thermal imaging, this method doesn't require contrast agents and instead invasive measures the light reflectance and absorbance of the analyzed surface in a non-invasive way. The usage of OI needs experience since it requires a optimal illumination of the scene and is affected by light scattering and light reflections. Both are to be controlled since they would otherwise prevent measurements at the respective sites.

2.9. NEURONAVIGATION

The discussed preoperative modalities support medical diagnosis and OP planning. Pathological objects and functional areas can be localized by means of different imaging technologies. Neuronavigation systems enable the use of these preoperative datasets in guided or navi-
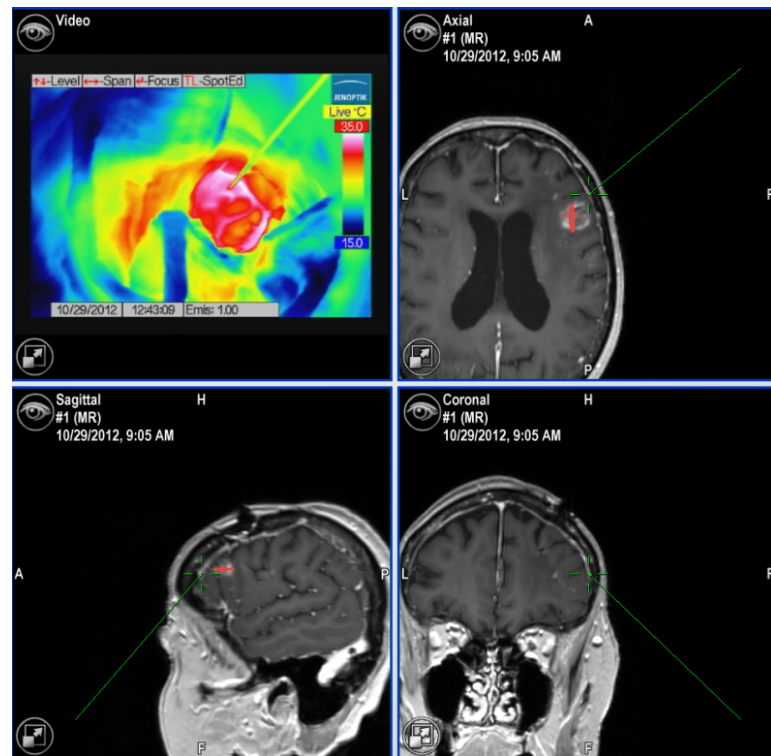
Figure 2.12.: Example image of the intraoperative screen of a neuronavigation system.

gated surgeries and provide valuable information to the surgeon. A global coordinate system is formed by a landmark-based registration technique. This enables the surgeon to correlate anatomical information, structures and other features of a preoperative dataset with the patient's exposed brain.

Fiducial markers are placed on the patient's head prior to any neuroimaging run. They are then segmented in the preoperative datasets and must be further intraoperatively selected on the patient's head by a pointing device. It is now possible to compute a homogeneous transformation to map the coordinates of a preoperative dataset to the tip of a pointing device and therefore register both datasets. After completed registration, the surgeon can correlate any point of the exposed brain with the respective position in any (registered) preoperative neuroimaging dataset. In the case of tumor resection, the surgeon can now infer the tumor demarcation from the neuroimaging dataset and ground his resection decision on these information. An intraoperative example of the application of neuronavigation systems is shown in figure 2.12.

2.10. TOWARDS THERMAL NEUROIMAGING

As reviewed in this section, there is a wide variety of neuroimaging techniques available. These can be classified as techniques for structural or functional imaging. Structural imaging allows the analysis of morphological *structures* of the analyzed object, for example to localize pathological neoplasms such as tumors. For guided and navigated neurosurgical interventions, this information enables the surgeon to differentiate tissue with respect to features that are characteristic for the respective modality during the OP, allowing, for example more

complete resections of tumors. In contrary, functional imaging is based on the analysis of cerebral metabolism or blood flow to unveil neural activity. It can be used to isolate focal epilepsies or to differentiate functional cortex from pathological tissue. Both applications improve the patient's quality of life after neurosurgical interventions by preserving as much function as possible.

In the case of intraoperative imaging, only a few modalities meet the respective requirements, such as keeping the delay of the OP short. The latter affects the usability of intraoperative MRI, since the neurosurgical intervention has to be interrupted and the patient has to be brought to the device for the measurement. Specific imaging techniques such as optical imaging and fluorescence imaging simplify this process, since they are based on microscopic measurements of the cortex during the OP. Hereby they either provide information regarding function (optical imaging) or structure (fluorescence imaging). Thermal imaging provides all means to close this gap through the analysis of the cortical heat distribution. The latter is driven by tissue composition as well as cortical perfusion. Hereby, combined functional-structural analysis of the cortex becomes possible with the same modality. In the next chapters, we discuss all necessary preprocessing as well as analysis tools to establish novel analysis of thermal images of the cerebral cortex for functional- as well as structural imaging at spatial resolutions as low as 170 μm and temporal resolution of up to 50 frames per second.

From a methodological point of view, we will now discuss required extensions of current state-of-the-art methods for intraoperative functional and structural imaging by thermography. An important aspect of intraoperative imaging is a seamless integration into existing systems and tools. For this reason a novel multi-modal 2D-3D intraoperative image registration and fusion framework grounding on developments in neuronavigation systems are required to co-register pre-operative 3D volumetric data with intraoperative 2D images. By proposing an efficient unsupervised vessel segmentation scheme based on detecting quasi-periodic patterns, we further set the foundations for the application of beamformers to thermal imaging data. In combination with the just discussed approach to multimodal image fusion, the integration of anatomic structures into the LDA beamformer[97], further analysis of a broad class of pathologies may become possible.

In the case of functional imaging, prevalent methods commonly employ statistical parametric mapping[29]. However, the underlying framework of general linear models has to be extended by means of effects specific to thermal imaging in order to achieve accurate results. Those will be introduced in the next chapter and all required extensions to the GLM framework are discussed in section 5.2. Alternatively, in the case of intraoperative optical imaging, [88] proposed a method based on a massively-univariate empirical thresholding of each pixels power signal densities without further statistical reasoning. This computationally efficient method lacks respective findings in statistical signal recognition like those provided by SPM.

Deep autoencoders (DAE, based on Restricted Boltzmann Machines as discussed in [95]) are quite general and flexible approaches for unsupervised representation of signals in a lower-dimensional space that is to be learned. The idea of learning a characteristic signal representation to unveil or correct certain behaviour seems very attractive in the case of heavily superimposed signals. In terms of intraoperative imaging, finding characteristic patterns of the cerebral cortex or camera motion are favorable applications of this approach. Therefore, we first applied this idea using PCA (which is shown to be similar to single layer linear RBMs[16]) to thermal imaging data and developed a generic unsupervised framework based on detecting encoded time-frequency domain features at determined spatial sites. In

this thesis, this framework was applied to estimate and correct camera motion. We further proposed to classify cortical pixels by encoding their time-domain signal using DAE and a combined Random Forest - Markov Random Field graphical model.

Finally, we newly developed a supervised irrigation detection framework to locate characteristic temperature behaviour in thermal imaging data. Through mathematical modeling of this behaviour, we demonstrated a novel method for intraoperative quantification of tissue perfusion.

3. THERMAL IMAGING

Thermal imaging (TI) is an imaging technique that detects the emitted heat radiation of a target object and converts it into temperature values. The thermal properties of an object's surface also correlate with its subsurface structure. Heat propagates through various layers of an object, making inner heat sources visible at outer layers or even at the surface, depending on the object's inner structure. At first sight, the working principle TI cameras are technically similar to CCD cameras, however the data is recorded in a different electromagnetic spectra. TI devices use a focal plane array of detector cells, enabling the spatially-resolved detection of incident heat radiation. Each cell is represented by a thermic sensor (microbolometer) that detects incident electromagnetic radiation in the mid- to long infrared range. This radiation heats the sensor and causes changes in the sensor's electrical resistance. Since this resistance change correlates with the amount of incident radiation, it can be computed into temperature values.

By just passively recording the emitted temperature of a body, thermal imaging is a contactless, non-invasive, whitelight-independent and marker-free approach to analyzing temperature distributions. Modern achievement in microtechnology improved state-of-the-art TI systems significantly. The number of detector elements has grown by a factor of 275 from 10880 pixels in 1993 ([84]) up to 3 megapixel nowadays, which leads to improved pixel resolutions. This causes growing interest in thermal imaging and therefore an even larger pervasion of various heterogeneous application domains in medicine, science and industry.

Thermal radiation itself and especially passive thermal imaging is vastly influenced by environmental noise and other heat sources which hamper data analysis in any application domain. Incident heat radiation of nearby humans, objects or even air also contribute to the detected temperature radiation. From a technical point of view, the detector hardware is another noise source since detector noise, hysteresis effects as well as challenges in medical and especially intraoperative applications (for example due to the camera being covered by a sterile case) further degrade signal quality.

In this section we give an overview to the technical prerequisites for the usage of thermal imaging in medical domains. For this purpose it is necessary to discuss the physical background to visualize the challenges of the employed technique. Using this knowledge we are able to qualify technical correction methods for certain prevalent issues and discuss common techniques to measure the quality of acquired thermal images. In the case of medical decision support systems, this knowledge allows us to assess the accuracy and validity of thermal imaging data as well as respective data analysis. This knowledge also presents fur-

ther directions to develop even more accurate methods. The latter are discussed in chapter 4 and enable the recognition of characteristic patterns at low signal-to-noise ratios which is a quite common setting in analyzing biological data. The combination of patient-specific information with technical issues of thermal imaging allows us to establish a reasonable data analysis framework for intraoperative thermal data.

3.1. PHYSICAL BACKGROUND

Each body with a temperature above 0K emits thermal radiation. The intensity of this radiation is maximized in the case of a black body which isotropically emits as much or more energy than any another body at the same core temperature. Besides convection and thermal conduction, the radiation and absorption of heat are the only means for a body to change its temperature. Thermal radiation is emitted as electromagnetic waves in mid- to long infrared range (7.5 – 14 μm wavelength). Yet, at higher object temperatures the spectral range of the heat radiation is shifted towards the visible light, causing for example very hot objects to glow yellow to red.
The Stefan-Boltzmann law for the emitted thermal radiation reads

$$P = \epsilon \sigma A T^4 \qquad (3.1)$$

It states that the emitted heat P depends on the bodies emissivity ϵ, the Stefan-Boltzmann constant σ, the object's surface A and temperature T. Emissivity denotes the amount of radiation that is emitted by a body. Black bodies are theoretically described by $\epsilon = 1$ since they emit a maximum of the possible radiation, while human tissue is characterized by an emissivity of approximately 0.98 [94]. The temperature contributes by the power of 4 to the emitted temperature radiation making it the main cause for temperature changes.

3.2. HEAT TRANSFER

Heat transfer denotes the propagation of heat energy from one system to another. According to the first law of thermodynamics, both systems change their energy household but the total energy is constant. Suppose all objects exchange their heat energy then they would converge to the same temperature. This property is called thermal equilibrium. In the following we will discuss dominant mechanisms for heat transfer (as of [103]):
Conduction denotes heat transfers in solids or liquids by microscopic effects. It occurs within one object or between two thermally coupled objects. Hot objects are composed of particles with an increased amount of kinetic and potential energy - both influence the velocity of molecules. This leads to an increased chance of collisions between molecules, yielding an energy transfer between them. The overall energy household of the respective matter doesn't change by this effect, yet deviations of each individual molecule's energy gets smaller over time, leading to a homogeneous distribution.
Convection requires an intrinsic flow, which is why this effect is limited to liquids and gases. The flow moves particles and therefore causes a certain form of mass transfer. The latter transports heat from one place to another until certain convergence criteria is fulfilled, meaning until the flow stops. Free convection denotes the induction of an intrinsic flow by means of temperature differences in a liquid, while forced convection requires outer forces (such as

a fan or pump) to cause fluid motion.

Thermal radiation is emitted by each object in terms of electromagnetic radiation. The amount of radiation is given by the Stefan-Boltzmann law (see preceding section 3.1).

3.3. DETECTORS

The detectors of thermal imaging devices are regarded as transducers that transform one form of energy into another. In terms of thermal imaging, incident electromagnetic radiation of the IR band is converted into electrical energy. Nowadays there are two dominant groups of detectors with orthogonal advantages and disadvantages. Photon (quantum) detectors absorb incident radiation by a photoelectric effect and convert it directly into an electrical quantity (for example current, resistance, conductivity)[103]. Microbolometer consists of IR absorbing materials (common materials are amorphous silicon and vanadium oxide) an electrode and a readout circuit. Incident IR radiation causes a resistance change in the IR absorbing material (bolometer effect) which is propagated to a readout circuit by an electrode. The lower the mass of the absorbing material, the less the energy is required to change its temperature, increasing the system's sensitivity[103]. Quantum detectors achieve high sensitivity and high framerates yet at the cost of requiring expensive cryogenic cooling solutions. Uncooled bolometers are inexpensive to produce and don't require any cooling, but they achieve considerably low frame rates and provide worse sensitivity than quantum detectors. Both detectors can be arranged in a focal plane array (FPA) consisting of a grid array of single detectors to achieve spatially resolved IR measurements.

3.3.1. INSTANTANEOUS FIELD OF VIEW

A single IR detector converts incident IR radiation into temperature values. In order to maximize the detector's accuracy, incident radiation has to impinge orthogonally onto the detector. This requires the detector to be aligned orthogonally with respect to the recorded object's surface. The instantaneous field of view (IFOV) now defines the allowed angular deviation from this constraint. Suppose a camera has an IFOV of 30 ° then its detector is able to integrate infrared radiation arriving in pyramidal-shape (its top being the detector) with a dihedral angle of 15 °.

3.3.2. NOISE EQUIVALENT TEMPERATURE DIFFERENCE

There are several factors to describe the sensitivity of IR detectors. Noise-equivalent power (NEP) defines the necessary radiant power to produce a signal-to-noise ratio of 1 for a given bandwidth in terms of W/Hz$^{1/2}$. An SNR of 1 implies that the (output) signal level and the noise level are equal. NEP therefore gives a lower bound on the measurable signal power of IR detectors. The bandwidth term allows for more comparable results since changing the bandwidth of the signal also influences the noise component. In terms of NEP for example doubling the bandwidth leads to an increase of the error by $\sqrt{2}$.

NETD now defines the amount of necessary incident radiation power to produce a signal with SNR 1:

$$\text{NETD} = \left(\frac{\delta \Phi_{BB}}{\delta T_{BB}} \right)^{-1} \text{NEP} \tag{3.2}$$
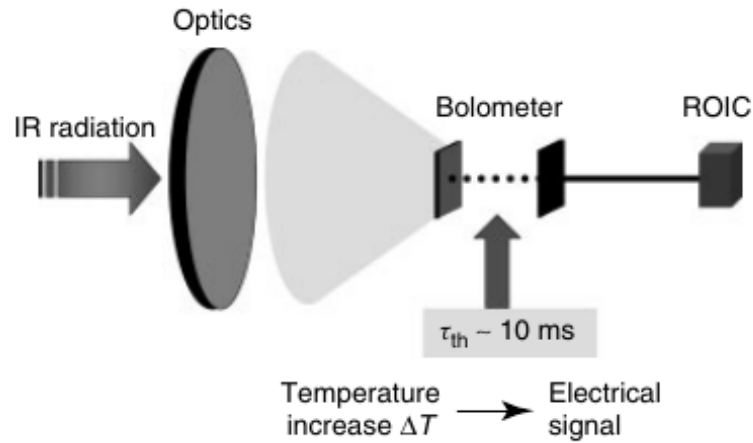
Figure 3.1.: A schematic overview of a bolometer based thermal imaging camera design. τ_{th} represents the delay until absorbed IR radiation causes a change in electrical signal of the bolometer. (image source: [103])

Equation 3.2 (see [103]) establishes the connection between radiant power difference $\delta\Phi_{BB}$, object temperature difference δT_{BB} and NEP. Hereby it yields the minimum difference in object temperature, which can be measured by the employed detector. [103]

3.3.3. NON-UNIFORMITY CORRECTION

Thermal imaging devices impose several challenges caused by the idiosyncrasies of IR detectors and focal plane arrays. These characteristics require special attention when analyzing long-term recordings. Microbolometer detectors are very sensitive to environmental conditions since they work by absorbing heat[1] which is then converted into electrical units. Suppose the camera's body heats up over time then this will inevitably influence the computed electrical current of the microbolometer. This hysteresis effect is known as (temperature) drift. Additionally in neuroimaging the desired signals typically inhibit low signal-to-noise ratio requiring more sophisticated data preprocessing methods.

The following discussion of the non-uniformity correction (NUC) is based on [103]. A focal plane array IR imaging system consists of a microbolometer IR FPA detector. Each microbolometer responds differently to the same amount of incident infrared radiation due to variances in the manufacturing process. If this effect is not corrected it leads to unrecognizable data. The latter error introduces both a bias and gain component.

Offset implies that a constant is added to the computed temperature values. A common correction method is a 1-point NUC. This approach requires the placement of a reference object (gray body with $\epsilon > 0.9$ [103]) with homogeneous temperature distribution in the camera's field of view. Now the deviation of each bolometer's temperature response to the target temperature is computed and its difference is used for correction.

Gain refers to the fact that the microbolometer's response to infrared radiation is non-linear in the amount of radiation (see section 3.1). For FPA detectors the error terms are location dependent, making a local gain correction necessary to achieve isotropic signals. This behaviour is corrected by a 2-point NUC in the affected temperature range. As we will discuss

---

[1]Note that the detector itself also emits temperature radiation.

later this behaviour also introduces mean shifts and discontinuities into the time course of thermal data requiring the special attention for subsequent data analysis workflows.

3.4. APPLICATIONS

Thermal imaging can be divided into two main groups: passive and active thermography. In passive thermography the imaging device just records the emitted heat of the surrounding objects. Reasoning is done solely by evaluating temperature deviations.

Active dynamic thermography (ADT) requires the usage of an external heat source to apply a temperature gradient to the surface of the recorded objects. This can either be done by a single temperature impulse or by periodically applying a temperature gradient. Another technique is the application of temperature gradients at varying strength to establish thermal tomography. The latter enables the evaluation of the temperature distribution of objects at varying penetration depths.

Thermal imaging is a prevalent technique in many non-medical domains. These include the detection of persons by their heat signature for border patrol or person rescue or non-destructive testing. The usage of ADT leads to specific heat distributions in materials and is especially useful to image transitions between components in order to detect heterogeneous surface structures or cracks.

In medicine, thermography was used centuries ago for blood pressure monitoring[14] and in dentistry[35]. In 2003, passive thermal imaging was employed in Taiwan as a method for SARS fever screening[74]. A very exhaustive discussion of more use-cases can be found in [73]. Shevelev published a study in 1993 wherein he successfully measured neural activity in rat brains by thermal imaging[84]. These findings were intraoperatively verified by Gorbach in 2003[33]. Gorbach demonstrated the visualization of neural activity in thermal imaging with a rather simple statistical approach ranging from speech mapping to sensory activations. A year later Gorbach published a paper about the possibilities of thermal imaging for tumor segmentation[34]. Steiner et al.[93] have shown that there's a direct link between temperature gradients and an injected cold bolus (ice-cold saline solution), which was used to quantify the cerebral blood flow. This method enables the analysis of the cortical perfusion under cerebral ischaemia.

In the following chapters we propose novel methods to (pre-)process thermal imaging data. These algorithms are then further used to analyze various neurosurgical use cases. Existing approaches like these of Gorbach are further extended by sound mathematical and statistical framework to improve validity, sensitivity and flexibility of the approaches. Finally we also propose a new intraoperative application of active dynamic thermography.
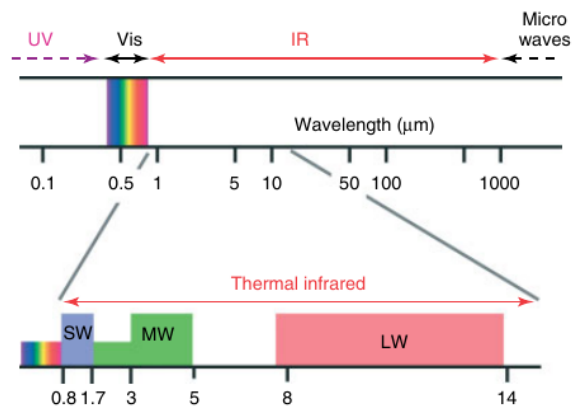
Figure 3.2.: This figure shows the spectral range and highlights the relevant part for IR imaging. (image source: [103])

4. IMPROVING PREDICTIVE ACCURACY AND PERFORMANCE OF THERMAL NEUROIMAGING

This chapter discusses published original work regarding various aspects to improve the data quality, signal to noise ratio and visualization of intraoperative thermal imaging data. These extensions are required, since thermographic images contain weakly differentiated anatomic information and are influenced by artifacts originating from physiological and environmental sources. In section 4.2, approaches to the estimation and correction of motion artifacts are discussed. We also propose an FPGA-based hardware motion correction scheme in section 4.3, that allows online correction of motion artifacts.

Thermal neuroimaging systems measure the emitted heat of the exposed cerebral cortex, which in turn is mainly influenced by tissue perfusion. This makes it difficult to correlate specific areas of thermal images with other modalities like intraoperative optical imaging or preoperative MRI/CT imaging. To solve this issue, we will discuss a novel generic image registration and image fusion algorithm in sections 4.4 and 4.5. Multimodal image fusion further allows the surgeon to better assess the quality of the gained results and depicts an important foundation for future combined multimodal reasoning and inference at very low SNR. The latter could allow the integration of information from preoperative fMRI measurements with intraoperative thermal and optical imaging to analyze functional connectivity or detect focal epileptic sites by state-of-the-art analysis methods for neuroimaging data as discussed in chapter 2.

4.1. LEARNING THERMAL PROCESS REPRESENTATIONS FOR CLASSIFICATION OF CEREBRAL CORTEX (OW A.1)

Intraoperative imaging imposes several changes to the employed algorithms such as minimizing the intraoperative delay. One approach to this constraint is limiting the analysis to only foreground objects. In the following we discuss a generic framework to classify pixels of cortical tissue.
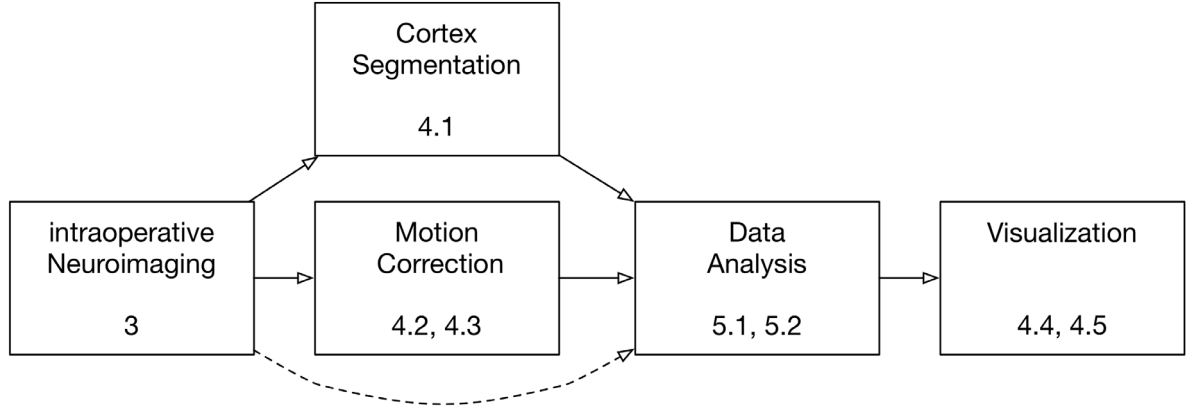
Figure 4.1.: Overview of the novel thermal neuroimaging data processing pipeline.

4.1.1. STRUCTURED PREDICTION FOR LATENT FEATURE REPRESENTATIONS

The time-resolved thermal behaviour of the exposed cerebral cortex is on one hand influenced by artificial noise sources like baseline drift of the thermographic signal. On the other hand cortical perfusion also contributes to the overall signal, although the actual influence to the measured thermographic signal is not fully understood yet. For this reason we propose to train an unsupervised autoencoder that independently extracts a latent representation of dynamic thermal behaviour. The probability distribution of these high-level features is then learned by a random forest. The regular structure of the imaging data is further exploited by extending local probability distributions in terms of knowledge of adjacent pixels.

1. Feature representation learning denotes the process of learning high-level features of low-level data. In the present case, prior to recovering a representation we have to estimate and remove the smooth background signal $T^{bg} = B_{2d}\widehat{\alpha}$ first by regressing $vec(T) = B_{2d}\alpha$ using least squares:

$$\widehat{\alpha} = (B_{2d}^T B_{2d})^{-1} B_{2d}^T vec(T) \tag{4.1}$$

with column stacked version $vec(T) \in \mathcal{R}^{nm}$ of the thermal data T and the tensor product $B_{2d} = B_{xy} \otimes B_t$ of two 1D B-Spline bases (see [28] for details).

2. High-level features $f(c_i)$ are learned from the background corrected and wavelet transformed signal $c_i(j, k)$ of pixel i at scale j and point k given some wavelet function ϕ

$$c_i(j, k) = \sum_j \sum_k (T_i(k) - T_i^{bg}(k))2^{-j/2}\phi(2^{-j}n - k) \tag{4.2}$$

with an linear autoencoder[102] (AE). This AE consists of an encoding $f(c_i)$ and decoding function $g(f(c_i))$ so that $(g \circ f)(c_i) = AE(c_i) \approx c_i$. The functions g, f are commonly modeled as sigmoid function with weight matrix $W \in \mathcal{R}^{d' \times m}$, bias vector $x \in \mathcal{R}^{d'}$. The decoding function $g(x)$ is commonly constructed by a tied weight $W' = W^T$:

$$f(c_i) = sigm(Wc_i + b) \tag{4.3}$$
$$g(c_i) = sigm(W'c_i + b') \tag{4.4}$$
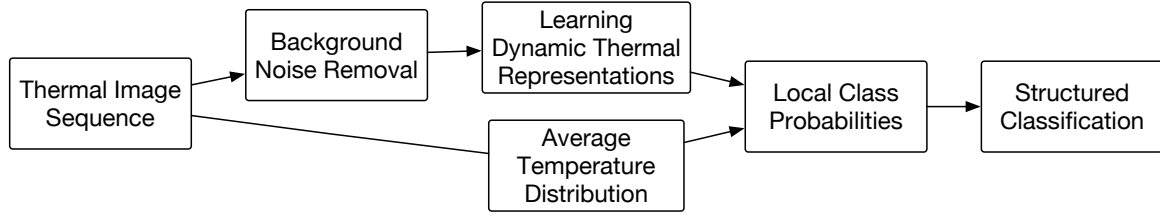
Figure 4.2.: Overview of the classification framework. (image source: OW A.1)

It has to be noted that the output of $f(c_i)$ is a lower-dimensional $d' \ll m$ compact representation of c_i meaning that the decoder $g(f(c_i))$ has to reconstruct the higher-dimensional c_i from a lower-dimensional projection $f(c_i)$. This approach preserves information while dropping noise terms. Recent developments aim to stack multiple AEs and train each layer independently[5]. The learning task is to minimize the reconstruction error of the input data whilst sparsity constraints are imposed to prevent overfitting[102]. Commonly, this learning is realized by minimizing a penalized squared loss function.

3. The probability distribution $p_i(y_i|f(c_i))$ of the unveiled high-level features for pixel i is then learned by a bagged random forest given a bootstrap sampled training set $(f(c_i), y_i)$ of $1 \leq i \leq n_t$ elements and labels $y_i \in \mathcal{Y}$ with $\mathcal{Y} = \{fg, bg\}$. In our case $p_i(y_i|f(c_i))$ represents the (un-)certainty that the encoded signal $f(c_i)$ belongs to state foreground $p(y_i = fg|f(c_i))$ or background $p(y_i = bg|f(c_i))$.

4. By exploiting the intrinsic regular structure of imaging data by a conditional random field we further improve the overall accuracy. A discriminative CRF model allows us to infer a global consistent state z_i depending only on the local probability $p_i(y_i)$ and of a probability distribution $p(z_f|y_f)$ factored given the neighbor's $f \in \mathcal{N}_i$ of pixel i. In general, the posterior distribution $p(Y|\mathcal{F}_C)$ of latent variables $y_i \in \mathcal{Y}$ and observations $f(c_i) \in \mathcal{F}_C$ can be formulated in terms of unary Ψ and pairwise terms Φ on a undirected graph $G = (V, E)$ as of

$$log\ p(Y|\mathcal{F}_C) = \sum_{i \in V} \Psi_i(y_i, f(c_i)) + \sum_{(i,i') \in E} \Phi(y_i, y_{i'}, f(c_i), f(c_{i'})) \tag{4.5}$$

Note that since only adjacent pixels i, i' are connected by an edge in E efficient factoring of equation 4.5 and therefore fast inference is achieved. The unary potential encodes the prior probability learned by the RF classifier whilst the pairwise potential encodes structural information. To simplify computations and exploit the structure of the imaged data we employ a Potts model:

$$\Phi(y_i, y_{i'}, f(c_i), f(c_{i'})) = C \cdot 1_{y_t = y_{t'}} \tag{4.6}$$

with indicator function 1 and C being a smoothness penalty. Since we are dealing with binary labels and Potts model equation 4.5 is submodular allowing the application of very efficient inference method based on graph cuts. Minimizing equation 4.5 now corresponds to finding a maximum a-posteriori estimate for the labeling y.

<div align="center">(a)   (b)</div>
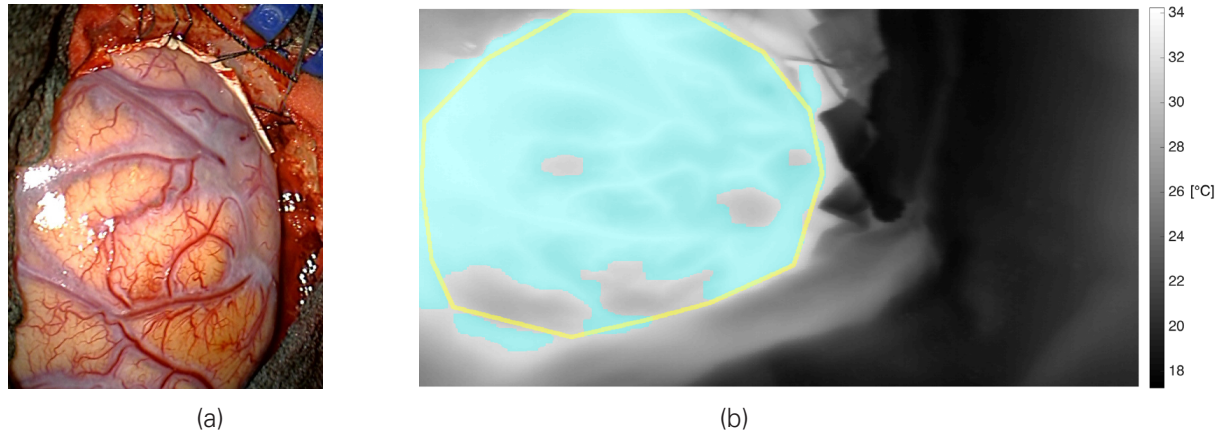
Figure 4.3.: Thermal neuroimaging is typically done just after exposure of the cerebral cortex as shown in **(a)**. This recording was then subject to the AE-CRF classifier and the results are shown in **(b)**. Expert classification of the cerebral cortex is indicated by the yellow solid line and the classification result is shown in turquoise. (image source: OW A.1)

4.1.2. RESULTS

In this work, we proposed a novel framework to learn characteristic thermal features. These are then used to analyze five intraoperative thermal recordings of the exposed cerebral cortex. We found that introducing latent feature representations yielded significant performance improvements compared to a temperature-based model for segmentation of foreground to background pixels. The results indicate that integrating thermodynamic behaviour of recorded objects allow more fine-grain differentiation. This approach might be a first step towards a

RF accuracy [%]	μT	BoW	PCA	AE	SAE
test	81.1	92.8	**96.5**	95.5	92.1
validation	81.1	87.4	**88**	87.3	85.1

Table 4.1.: Using a single Random Forest classifier, there is a clear gain in accuracy by the application of learned high-level dynamic thermal features.

more detailed tissue characterization by means of its dynamic temperature behaviour. In contrary to classical machine learning approaches, no explicit feature crafting is required since discriminative features are learned independently. Therefore, the framework is not limited to the discussed segmentation task but introduces enough flexibility to unveil various pathological patterns if these can be characterized by thermal behaviour.

CRF accuracy [%]	μT	BoW	PCA	AE	SAE
test	86.1	94.4	**98.5**	98	94.8
validation	87.7	89.1	88.8	**89.2**	88

Table 4.2.: The RF-CRF model compensates false negatives of the plain RF classifier and improves its performance considerably.
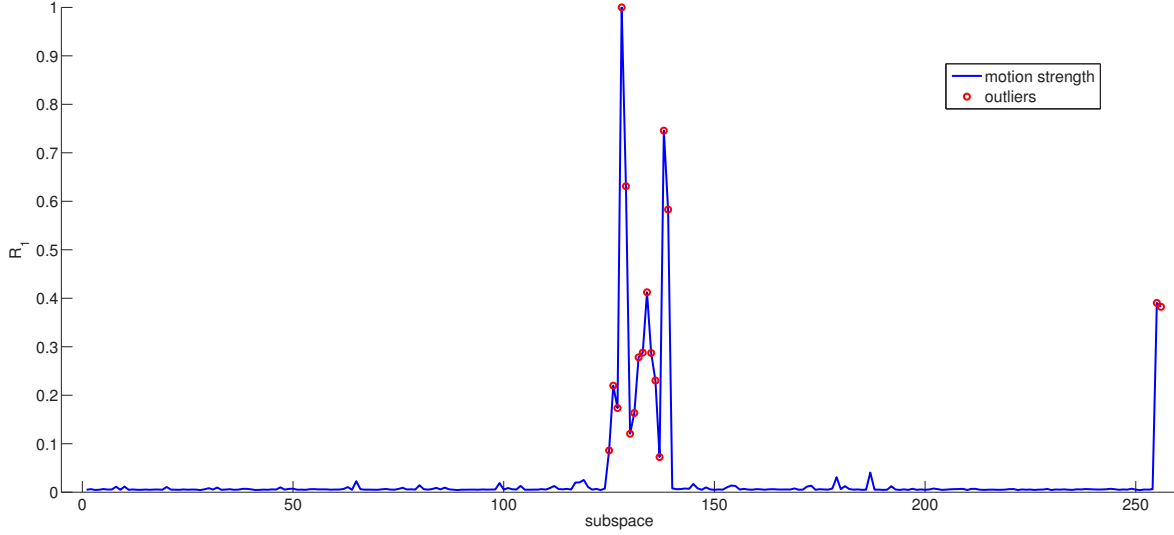
Figure 4.4.: The subspace contribution ratio *R* shows significantly outlying values in the case of an eigenvector resembling the characteristic pattern of motion artifacts. (image source: OW A.2)

4.2. FILTERING OF CAMERA MOVEMENT ARTIFACTS (OW A.2)

Intraoperative recordings of thermal imaging systems require object distances below 30cm to minimize the influence of external noise sources. This is achieved by mounting the camera at the operating table with a system consisting of several freely movable hinges. Yet this setup is prone to vibrations caused, for example, by the initial alignment of the camera or during electrical nerve stimulations for brain mapping. These vibrations induce a periodic shift of the whole camera which introduces artifacts into the time course of each pixel and affects subsequent time series analysis. In the case of weak signal to noise ratios the error might superimpose existing signals in the same frequency range.

4.2.1. WAVELET-BASED MOTION CORRECTION SCHEME

We compensate this error by exploiting the global characteristics of the introduced motion pattern using principal component analysis in time-frequency domain. The approach is sketched as follows:

1. The camera movement leads to a linear shift of all pixels in the same direction at small time scales. Therefore, all pixels follow the same trajectory and show similar behaviour. The amplitude of the error strongly depends on the pixels Jacobian matrix. High values and therefore distinct gradients induce strong artifacts.

2. Let the time course of *n* pixels be modeled by $X_{raw} \in \mathbb{R}^{n \times m}$ with $m = 2^{j_{max}+1}$ and $j_{max} \in \mathbb{N}^+$. Let us further denote $X^j \in \mathbb{R}^{n \times m}$ the wavelet transformed X_{raw} (see the previous section) at wavelet scale *j*. Various components superimpose the data in this domain, for example periodic heart rate patterns, neural activity and global motion artifacts. One approach to differentiate the latter artifacts from actual data is principal component

analysis. PCA requires an eigenvalue decomposition of the empiric covariance matrices of the wavelet coefficients $X^j \in \mathbb{R}^{n \times 2^j}$ at wavelet scales $1 \leq j \leq j_{max}$. Each of the $1 \leq k \leq 2^j$ eigenvectors v_k^j describes a characteristic frequency pattern. By a change of basis of X^j given $\Phi = [v_1^j \cdots v_{2^j}^j]$ into

$$W^j = X^j \Phi = \begin{bmatrix} w_1(1) & \ldots & w_{2^j}(1) \\ \vdots & \vdots & \vdots \\ w_{2^j}(n) & \ldots & w_{2^j}(n) \end{bmatrix}$$

we represent all pixel's wavelet coefficients at scale j in terms of the eigenvectors v_k^j and score w_k. Eigenvector k describes a global time-frequency pattern that contributes to the overall time-frequency content of pixel i by $w_k(i) \in \mathbb{R}$.

3. Now we can form two sets of pixels. One containing pixels in distinct $\mathcal{X}^+$ and another containing pixels in the rather smooth $\mathcal{X}^-$ neighborhoods. Distinct neighborhoods lead to larger amplitudes of the error pattern compared to the expected strength of the artifacts in smooth neighborhoods. We quantify this assumption by the subspace contribution ratio r_k (see figure 4.5):

$$r_k = w_k(\mathcal{X}^+) / w_k(\mathcal{X}^-) \tag{4.7}$$

4. Eigenvectors that resemble global motion artifacts lead to a skewed ratio of $w_k(\mathcal{X}^+)$ to $w_k(\mathcal{X}^-)$ hence cause significantly deviating values of r_k. In order to isolate these eigenvectors, we form a global motion impact factor $R^j = (r_1, r_2, ..., r_2^j)$ for each scale j. This factor is modeled as a Gaussian random variable: $R \sim N(ax + b, \sigma)$. The parameters are fitted using iteratively-reweighted least squares and outlying r_j's are found by a t-Test with Bonferroni corrected significance level $\alpha = 0.05/m$ and m being the number of tests (pixels). Eigenvectors with outlying r_j's are then wiped and the motion corrected estimate is achieved by inverse PCA and inverse discrete wavelet transform.

4.2.2. RESULTS

This procedure was applied to two intraoperative datasets. Since no ground-truth data is available, the average spectral density is used as a measure for motion correction. Dataset 1 was recorded during an ECoG measurement with high-frequent vibrations of the camera system at a spatial extent of 5 pixels ($\sim$ 1 cm). After application of the proposed method, any motion artifact visually disappeared. The average spectral density was further significantly lowered by the proposed method. The second dataset consists of weak motion artifacts but strong spatially independent thermal background noise. Even in this case, the average spectral density was highly reduced and any motion visually disappeared. In order to validate the method, we further employed a feature matching approach based on estimating and pairing SURF feature descriptors of adjacent frames. This approach yields good results in dataset 1, yet failed to recognize correct motion trajectories in dataset 2, causing deformations of the whole image. The results of both methods are shown in table 4.3. Using the discussed motion correction scheme, we are able to estimate the actual error pattern and integrate it into subsequent data analysis workflows. It furthermore allows us to differentiate global artifacts from local periodic effects with similar spectral bandwidth. The latter is especially useful
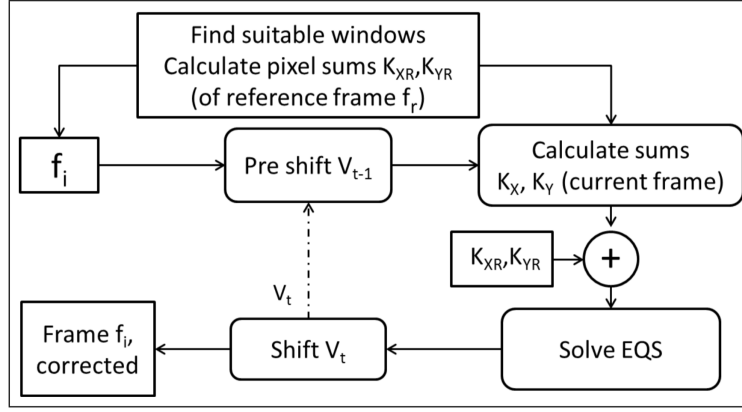
Figure 4.5.: The proposed FPGA-based workflow for online correction of motion artifacts is shown in this figure (image source: OW A.3).

since we are now able to differentiate motion terms from pulse rate frequency components.

spectral density	uncorrected	SURF	WSA-GT
Case 1	7541.724	1952.466	1285.724
Case 2	1951.909	116347.54	927.683

Table 4.3.: Evaluation of average spectral density of the algorithms with respect to two intra-operative cases.

4.3. OBJECT-BASED MOTION CORRECTION BY HARDWARE OPTICAL FLOW ESTIMATION (OW A.3)

In the last section we discussed an offline method for motion correction. The approach yields a reasonable performance and allows the estimation and correction of motion related artifacts by a novel multivariate statistical analysis framework in time-frequency domain. In the following, we extend these results by an online image analysis approach. Online methods are a favorable extension to offline methods such as those mentioned in the previous section, since they allow (near) real-time application and therefore do not introduce any further delay to intraoperative workflows. In OW A.3 we therefore extend the discussed approach of section 4.2 by a novel online method designed and aimed to develop an integrated device. It is implemented on an FPGA-based platform[11] optimized for cellular non-linear networks.

4.3.1. REALTIME OPTICAL FLOW ESTIMATION

The following approach is based on estimating optical flow in hardware to recover the global motion trajectory to compensate the previously discussed movement artifacts. Fortunately, this approach is easy to implement on CNN systems yet it imposes a constraint to the data: only marginal temperature gradients are allowed between adjacent frames. The whole algorithm is sketched as follows:

1. The translation $(\Delta x, \Delta y)$ of a pixel within one timestep is modeled as of

$$I(x, y, t + 1) - I(x, y, t) \approx \frac{\delta I}{\delta x} \Delta x + \frac{\delta I}{\delta y} \Delta y \qquad (4.8)$$

2. Object-based optical flow estimation requires a slight modification to the former equation yet yields an algorithm being more robust to noise. Suppose global motion has occurred and we are given pixels $k_i \in W$ with $1 \leq i \leq N$ of an arbitrary partition $W \in \mathcal{W}$ of the set $\mathcal{W}$ of pixels. By solving the basic equation of object-based optical flow estimation (equation 4.9) using least squares we can now recover an estimate for global motion in Δx and Δy direction within time points t and $t + 1$ by

$$\begin{bmatrix} K(t; w_1) \\ \vdots \\ K(t; w_4) \end{bmatrix} = \begin{bmatrix} K_{X1}(t) & K_{Y1}(t) \\ \vdots & \vdots \\ K_{X4}(t) & K_{Y4}(t) \end{bmatrix} \begin{bmatrix} \Delta x \\ \Delta y \end{bmatrix} \qquad (4.9)$$

given 4 windows, $K(t; w) = \sum_{p \in w} I_p(t + 1) - I_p(t)$ and K_{X_j}, K_{Y_j} being the summed partial derivatives of window j.

3. The choice of the window for motion estimation influences the sensitivity and specificity of the approach. In order to maximize the overall accuracy, we propose the following window selection strategy: apply a binarization procedure at decreasing threshold levels to a thermal image followed by an edge detection step. This leads to an increasing number of black pixels p_b in the image. We propose to use the cortex shape at the local minimum $min(p_b)$ for optical flow computation.

4.3.2. RESULTS

The approach was implemented on a novel CNN hardware platform for high-speed signal processing[11] and applied to intraoperative data. Run times of 4.7 ms (8Bit) and 13.3 ms (12 Bit) per frame validate the demanded online performance since the employed thermal imaging system records data at up to 50 Hz. The evaluation yielded results with accuracy being comparable to the previously discussed offline PCA-based method. We found that for larger cortex images, an improved window selection scheme must be employed in order to improve the overall performance. In summary, the approach is an efficient and generic scheme for hardware optical flow estimation and motion correction which is applicable to thermal imaging data recorded during arbitrary neurosurgical interventions.

Spectral Density	Uncorrected	WSA-GT	CNN
Case 1	7541.724	1285.724	1516.237
Case 2	1951.909	927.683	1355.013

Table 4.4.: Comparison of average spectral density between Wavelet and CNN/Hardware-based motion artifact filtering.

4.4. IMAGE FUSION OF INTRAOPERATIVE THERMAL IMAGING WITH PREOPERATIVE MRI (OW A.4)

Thermal images originate from the emitted heat of a body and are primarily influenced by cortical perfusion. Both factors lead to smooth images without distinct gradients which hamper the precise correlation of thermal imaging data with structural (anatomic) features of other neuroimaging technologies (for instance preoperative MRI or optical imaging) to some extent. In order to combine information recovered from analyzing the heat distribution with structural features, we propose to use image registration and fusion frameworks. In detail we approach this idea by a generic 2D-3D calibration based image registration and image fusion framework. A generic approach is desirable since medical neuroimaging typically combines various techniques, ranging from thermal imaging, ultrasound, optical- to fluorescence imaging. The combination of all information might yield further hints regarding the treatment of specific pathologies.

4.4.1. CALIBRATION-BASED MULTIMODAL IMAGE FUSION FRAMEWORK

Guided tumor resections are typically supported by intraoperative neuronavigation systems (INN). These systems require the registration of the patient with preoperative imaging modalities by matching the position of so called fiducial markers in preoperative datasets with their actual position on the patient's head during the op. Another feature of neuronavigation devices is tracking the spatial position of so called instrument adapters (IA), which in turn can be attached to arbitrary devices. The main task of the developed framework is to establish a projection of the spatial position of the instrument adapter to the position of the sensor array of the imaging device. This allows the projection of any coordinate in the device's coordinate system to the coordinate system of the neuronavigation system. Image fusion can now be carried out by projecting the coordinate from one coordinate system to the nearest coordinate in the other coordinate system and interpolating the data where required. The general approach is:

1. Mount the instrument adapter onto the imaging device to continuously track its position.

2. The projection of the spatial position of the instrument adapter to the position of the sensor array of the imaging device in INN coordinate space is established by an compound affine transformation T. The latter maps the spatial position of the instrument adapter onto the position of the imaging system's sensor array and corrects the dimensions of the virtual image plane:

$$T = M_{\text{scale}} * M_c * M_a * M_{\text{Brainlab}} \qquad (4.10)$$

The transformation requires estimates of the camera calibration matrix M_c, additional transformations M_a, the spatial position and orientation of the instrument adapter M_{Brainlab} and M_{scale} for correcting the size of the virtual image plane. The parameters are to be estimated once by an offline calibration scheme which is discussed in original work A.4.

3. The 2D coordinates of the thermal images are projected onto the isosurface of the other 3D modality by a texture mapping approach. The underlying 2D-3D point corre-

(a) Orthogonal Projection

(b) Image Fusion MRI - Thermography
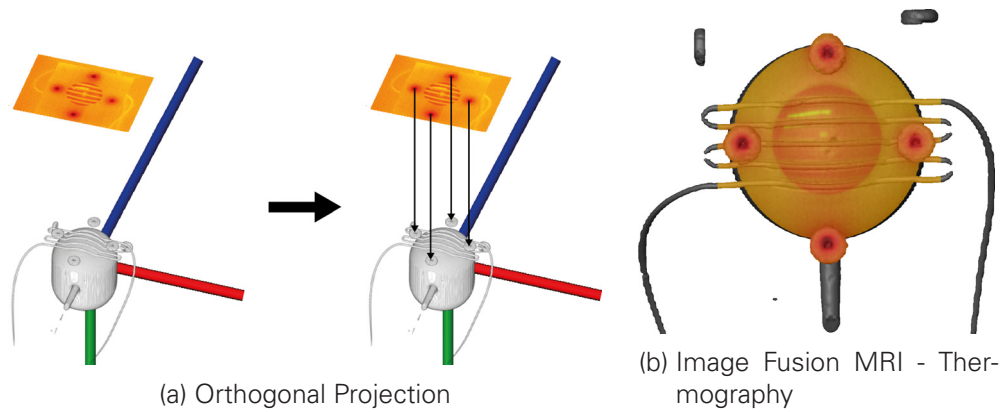
Figure 4.6.: By using an orthogonal projection as seen in (a), it is possible to map 2D planes onto 3D surfaces (b). (image source: OW A.4)

spondence problem is solved through an orthogonal projection, meaning that the 2D coordinate is projected along the image normal onto the surface of the 3D object as shown in figure 4.6.

4.4.2. RESULTS

The experiments were carried out by a novel imaging phantom[106] whose MRI dataset was acquired by a 3D MRI Siemens Magnetom Verio scanner. Accuracy analysis for a BrainLab VectorVision neuronavigation system was realized by an exhaustive evaluation suite to quantify influence factors to the system accuracy, such as calibration of the instrument adapter, tracking beam accuracy, MRI accuracy, orientation of the camera with respect to the surface. We identified that repeated mounting of the instrument adapter depicts the most influential factor to the system's overall accuracy. In order to estimate the worst-case accuracy, we placed the IA at extreme positions. This experiment yielded a worst-case inaccuracy of 1 cm. The average accuracy of the system was 2.46 mm. Further accuracy improvements can be achieved by using the so called microscope adapter of BrainLab's neuronavigation system. This (costly) IA doesn't require any re-calibration and also has an extra mounting bracket so that it can be easily attached to various imaging devices.

The discussed image registration and fusion framework enables the intraoperative multi-modal image fusion so that extracted information from 2D intraoperative imaging devices such as thermal- or optical imaging can be combined with and integrated into intraoperative neuronavigation systems. This allows the surgeon to validate the gained analysis results of 2D intraoperative imaging by means of their anatomic plausibility as well as to combine rather abstract thermal information with morphological structures. Another future approach depicts the extraction of anatomic and tissue information from preoperative 3D imaging modalities such as CTI or MRI and use this knowledge as prior to intraoperative data analytics frameworks. The influence of vascular diseases on the arrival time of perfusion tracers could now be modeled in terms of extracted structures from preoperative magnetic resonance angiography recordings. Another future aspect might be the utilization of specific information from human brain atlases such as the localization of Broadman areas relative to the exposed cerebral cortex for improved intraoperative brain mapping.

4.5. CLASSIFICATION OF PERFUSED BLOOD VESSELS BY GAUSSIAN MIXTURE MODELS (OW A.5)

The discussed calibration based method for multimodal registration is applicable in the case of guided neurosurgical interventions. Another approach to image registration and image fusion is feature matching. Features of the same scene but recorded from different orientations are extracted and correlated by optimizing a certain energy functional. In the case of unguided neurosurgical interventions, the previous approach is not applicable since a neuronavigation system is not available. Image fusion of thermal- with optical imaging is highly desirable since this combines perfusion and structural imaging. In the case of intraoperative optical imaging of the exposed cerebral cortex, vessel structures can be recognized as a foundation for feature based image fusion. In thermal imaging, small vessels are more difficult to reveal and large arteries are not likely to be visible as well. Vessels located in subarachnoid space are subject to motion caused by blood flow, which induces a characteristic signal into their time course.

4.5.1. DETECTION OF QUASI-PERIODIC PATTERNS FOR VESSEL SEGMENTATION

We now propose a method for the extraction of cortical vessels in thermal imaging recordings as a foundation for subsequent unsupervised feature-based image registration and fusion approaches. The required steps of the vessel detection framework are:

1. Recordings of the exposed cortex are mainly affected by two periodic components originating from respiratory and heartbeat activity. Respiratory cycles f_{RM} are fixed to 9 to 12 beats per minute whilst heartbeat cycles f_{HM} range from 40 to 120 beats per minute. Data analysis is carried into wavelet domain in order to recognize these time-frequency features. Suppose $j_H M$ and $j_R M$ denote the wavelet scale of heartbeat motion and respiratory motion. The wavelet coefficients $w^{j_{HM}}$ and $w^{j_{RM}}$ are computed by decimating the measured thermal signal (in case of fast discrete wavelet transform) meaning that the periodic signal in x has to be adjusted to the respective scale j and sampling frequency f_s for subsequent classification

$$f_{RM}^j = f_{RM} \cdot f_s / (j_{max} - j_{RM}) \qquad (4.11)$$

$$f_{HM}^j = f_{HM} \cdot f_s / (j_{max} - j_{HM}) \qquad (4.12)$$

2. The decimated quasi-periodic pattern can now be used for an efficient recognition scheme. These patterns contribute with significant power to the projection into time-frequency domain dominating other components of the same scale. Therefore we propose the following 2-Gaussian Mixture Model on the squared wavelet coefficients

$$p(w_{j_{HM}}^2 | \theta) = \sum_{i=1}^{2} \pi_i p_i(w_{j_{HM}} | \theta) \qquad (4.13)$$

with $\theta = \{\theta_1, \theta_2\}$ and $\theta_i = \{\mu_i, \Sigma_i, \pi_i\}$. The first component describes wavelet coefficients being affected by heartbeat motion which is approximated by initializing $\mu_1 = sin^2(2\pi f_{HM}^{-j})$ and $\Sigma_1 = \sigma_1 l_k$. The background component is modeled by $\mu_2 = \vec{0}$ and $\Sigma_2 = \sigma_2 l_k$. Parameter estimation and classification is achieved by the Expectation Maximization algorithm.
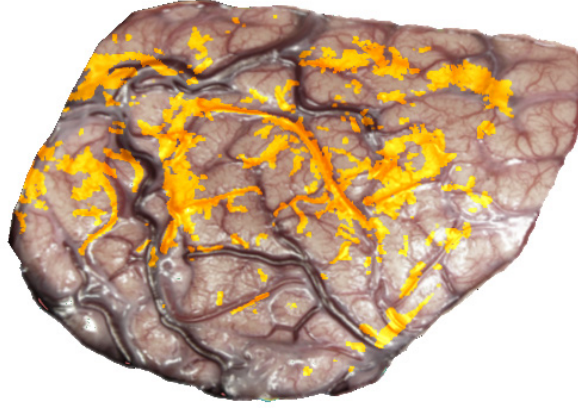
Figure 4.7.: Extracted cortical vessels registered to an optical imaging recording of the same scene. (image source: OW A.5

3. Heartbeat and respiratory motion is a priori unknown which requires an empiric estimation scheme. Let $\mathcal{F}(f)_+ = max\{|\mathcal{F}(f)_{p_1}|, \ldots, |\mathcal{F}(f)_{p_m}|\}$ be the maximum Fourier coefficient of frequency f evaluated at pixels p_k with $1 \leq k \leq m$ then we estimate $\widetilde{f}_{HM}$ by

$$\widetilde{f}_{HM} = \underset{f \in [0.5;2]\ Hz}{argmax} \{\mathcal{F}(f)_+\} \qquad (4.14)$$

4.5.2. RESULTS

The approach was applied to several intraoperative recordings with promising results. Nonetheless it has to be emphasized that vessels in subarachnoid space inherit the recognized cyclic motion pattern meaning that only a subset of all optically visible vessel structures were detected in thermal imaging. Motion is also assumed to dominate the thermal signal of cortical arteries because these are more affected by cortical blood flow than veins. Both points prevent the recovery of all cortical vessels by the discussed method, as can be seen in figure 4.7. Further advances now require a robust matching procedure to correlate the vessel structures from optical imaging with the segmented structures in thermal imaging. Since we have identified the spatial position of cortical arteries, we can now use this information for analysis of cortical blood flow, for example to recognize the first arrival time of applied temperature tracers ("cold bolus approach"[93]) by LDA beamformers[97] (see section 2.7 for details). In the case of perfusion disorders, this knowledge could be used to infer information about the pre- and post treatment perfusion state of cortical vessels.

4.6. SUMMARY

Medical imaging imposes several challenges and constraints to data scientists. Typical intraoperative workflows, especially in the case of emergency situations, don't allow for intense care to the imaging setup. One consequence is the introduction of motion artifacts to the whole camera setup which can be traced back to the mounting of the camera and rapid installations. These artifacts affect subsequent data analysis frameworks by superimposing medical signals, making a motion correction scheme necessary. In section 4.2 and 4.3 we

propose novel approaches to this issue that are optimized for intraoperative thermal imaging and minimized time complexity of the chosen approaches. We developed a realtime motion correction system using FPGA hardware in section 4.3. This now allows online motion correction and therefore doesn't delay subsequent data analysis. We further minimize the computational time of the overall medical decision support system by proposing a new efficient foreground - background segmentation scheme in 4.1. By integrating latent time-frequency features into a conditional random field we are able to differentiate cortical from non-cortical tissue. As a consequence, subsequent massively-univariate statistical analysis pipelines on the reduced data achieve significant performance improvements since larger quantities of the data do not need to be analyzed.

In order to correlate inferred knowledge of thermal images with other intraoperative and preoperative data, we also discussed a novel image registration and fusion framework in section 4.4. By a generic formulation of the calibration-based 2D-3D multimodal image registration and image fusion algorithm, it is possible to combine arbitrary imaging devices. Without loss of generality the method was evaluated on intraoperative 2D thermal imaging in conjunction with preoperative 3D MRI data. In section 4.5 a method for vessel segmentation is presented which yields the necessary tools for subsequent unsupervised and automatic featured-based image fusion of thermal images with concurrent optical imaging. Both image fusion approaches empower surgical personnel to better interpret yielded results from data analysis and therefore might lead to improved medical reasoning and patient's safety.

5. INTRAOPERATIVE APPLICATIONS OF THERMAL NEUROIMAGING

Thermal Imaging is a novel neurosurgical approach to analyze the emitted heat of the exposed cerebral cortex. This heat analysis enables inference regarding (sub-)cortical perfusion and tissue composition. The following applications are based on heat transfers caused by intracerebral perfusion. The steady cerebral perfusion depicts an important requirement for the preservation of tissue metabolism. The temperature gradient of blood disseminates through surrounding tissue whereas the actual dissemination characteristics correlate with the vessel's size and the tissue's composition. Since the whole cortex is composed of vessels at various scales, it is therefore possible to quantify its perfusion and use this information to infer knowledge regarding functional activity and structural abnormalities. All intraoperative procedures were approved by the Human Ethics Committee of the Technische Universität Dresden (no. EK 323122008). To the best of our knowledge, we are first to establish a method for the analysis of the cortical heat distribution of patients who suffered from an ischaemic stroke. As we will show, this approach allows a standardized characterization of the extent of hypoperfused cortical tissue.

Through neurovascular coupling (NVC) temporary changes in cortical perfusion are introduced in the case of focal neural activity. This altered perfusion also leads to a weak change in surface temperature. In our second application domain of intraoperative thermal neuroimaging, we develop a mathematically sound framework for the detection of statistically significant changes in mean temperature as those being caused by NVC. The model is tuned for thermal imaging by incorporating specific effects such as low- and high frequent non-linear baseline drifts with step discontinuities due to the non-uniformity correction.

5.1. PERFUSION CLASSIFICATION OF ACUTE ISCHAEMIC STROKES (OW A.6)

Active dynamic thermography denotes the method of applying temperature gradients to the surface of a evaluated subject for analysis of its time-dependent thermal behaviour. In medical thermal imaging, this method was employed to analyze burned skin[66] and to evaluate tumor tissue[34]. We extend these findings by a generic mathematical framework for detection and classification of arbitrary cooled NaCl irrigations of the cortex during continuous

recordings and following analysis of its heating behaviour. This framework is applied to the analysis of tissue perfusion of patients suffering acute ischaemic strokes with indicated decompressive hemicraniectomy. The measured temperature variations in intraoperative thermal imaging mainly originate from cortical perfusion. This fact can be used as marker for cell state and neural activity. In previous works, Steiner et al.[93] evaluated the cortical blood flow by a central venously applied ice-cold sodium chloride solution and subsequent multivariate analysis. We extend these findings by the evaluation of the heat distribution of the exposed cortex after application of a cold NaCl solution to infer standardized perfusion parameters and classification of tissue state. NaCl irrigation are a standard procedure in neurosurgery as they are harmless and prevent dehydration of exposed tissue and therefore do not require special effort or training of the surgeons.

In the following, we extend prior findings of Gorbach[34] by an approximate model of dynamic thermal behaviour of tissue and propose a machine learning method for tissue perfusion state classification. Another extension is a machine learning based streaming detector for online recognition of a wide variety of cooling events during continuous intraoperative recordings. This approach is new to Neurosurgery and depicts a novel method for intraoperative classification of tissue state of patients suffering acute ischaemic strokes.

5.1.1. STREAMING IRRIGATION DETECTOR

Cortical irrigations can be applied in very heterogeneous ways, making the streaming detection of irrigation events a challenging task. In the following we will give a schematic overview to the irrigation event detector for continuous thermal measurements. A detailed discussion can be found in the original work A.6.

1. An irrigation event denotes the point of time after which a cold NaCl solution was applied to the cortex. This event causes a characteristic pattern into sorted thermal data $s_i(p)$ of pixel p and index $i \in [1, .., n]$. The quality of an irrigation event of pixel p is denoted by $m(p)$:

$$m(p) = f_{\mathrm{norm}} \times \sum_{i=i_1}^{i_{step}} |T(p, s_i(p)) - corr(i)| < t_{\mathrm{div}} \tag{5.1}$$

given normalization factor f_{norm}, measured temperature $T(p, s_i(p))$ of pixel p at time index i. $corr(\cdot)$ denotes a correlation function (following the shapelet idea of Ye and Keogh[110]) that is used to compute the similarity of the measured thermal signal with a single exponential function relative to the threshold t_{div}. This exponential function can be seen as an approximation to tissue heating[66].

2. We integrate information about detected irrigation events of adjacent pixels into the framework by

$$\sigma(p_s, p_t) = f \times max(\Delta T_{p_s}, \Delta T_{p_t}) \tag{5.2}$$

with ΔT_{p_s} and ΔT_{p_t} being the maximum temperature differences in the analyzed temporal windows of pixels p_s and p_t while f represents the similarity of both cooling events. The weighted distance metric $\sigma(p_s)^{sum}$ integrates the local score of pixel p_s over its

neighbors $p_t \in \mathcal{N}(p_s)$ given a distance metric $\Delta(p_s, p_t) = 1/(ln\|p_s - p_t\|_2 + 1)$:

$$\sigma(p_s)^{sum} = \sum_{p_t \in \mathcal{N}(p_s)} \Delta(p_s, p_t) \times \sigma(p_s, p_t) \tag{5.3}$$

An irrigation event is flagged as detected if $\sigma(p_s)^{sum}$ is greater than a learned threshold.

3. Since several irrigations can occur during continuous thermal imaging, a selection scheme is required for comparable data analysis. The basic idea is to match the irrigation event's time stamp with an estimated reference time stamp t_{ref}

$$t_{ref} = \underset{t_j \in \mathcal{C}}{argmax} \left\{ \sum_{i=-2}^{i=2} h(t_{j+i}) \right\} \tag{5.4}$$

which resembles the time stamp of a cooling event that affected the highest number of pixels.

4. Parameter learning is achieved by a Metropolis-Hasting Markov Chain Monte Carlo sampler[32]. Details can be found in the original work A.6.

5.1.2. TISSUE STATE CLASSIFICATION

In the following we will discuss necessary steps in order to achieve a standardized quantitative representation of cortical perfusion. Following, a segmentation by a 3-Gaussian Mixture Model is employed to unveil latent tissue states.

1. Tissue perfusion is approximated by Antoni Nowakowski's double exponential model [66]:
$$T(t) = T_{equ} + \Delta T_1 exp(-t\lambda_1) + \Delta T_2 exp(-t\lambda_2) \tag{5.5}$$

wherein T_{equ} depicts the tissue's equilibrium temperature while ΔT_1 and ΔT_2 are scaling coefficients. The temperature decay constants λ_1 and λ_2 characterize the tissue's temperature change rate. At least two sources influence the tissue's heating behaviour: temperature change caused by the applied liquid and the temperature change induced by subcortical tissue and perfusion. We assume that λ_1 of the liquid is larger than λ_2 since liquid drains quite fast compared to tissue heating.

2. Suppose λ_2 describes the heating behaviour of underlying tissue, then very characteristic values in the case of ischaemic strokes can be expected, such as low values of λ_2 for hypo- and unperfused tissue. An increased or even hyperperfusion yields significantly highly values at these sites.
Now, λ_2 is sampled from latent tissue state $\mathcal{S} = \{ischaemic, uncertain, healthy\}$ depending normal distribution, whereas its actual value varies at different scales depending on the perfusion state. The expected behaviour of λ_2 is approximated by

$$\lambda_2^{ischaemic} \sim N(\mu_i, \sigma_i)$$
$$\lambda_2^{uncertain} \sim N(\mu_u, \sigma_u)$$
$$\lambda_2^{healthy} \sim N(\mu_h, \sigma_h)$$
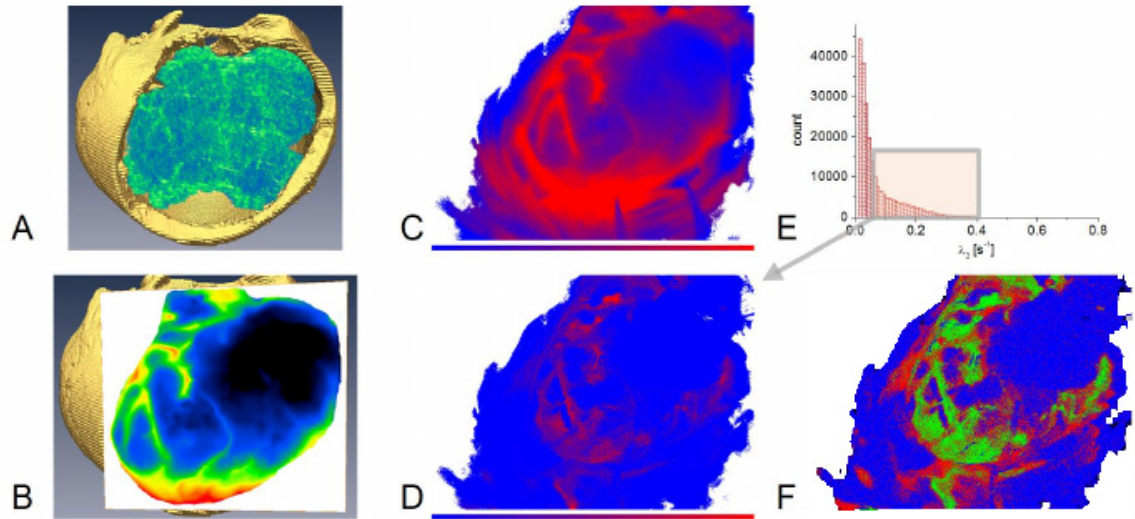
Figure 5.1.: This figure shows the results of dataset 5. In **A**, the infarct demarcation is segmented as green-blue in a post-operative CT recording. Subimage **B** shows the orientation of the thermal image to the CT dataset. **C** depicts the temperature distribution at equilibrium temperature after the irrigation. **D** displays the spatial distribution of λ_2 and **E** shows the histogram of all λ_2 values. **F** represents the segmentation as result of fitting the 3-Gaussian mixture model. Blue represents the ischaemic / low perfusion state, green the healthy state and red representing uncertainty. The estimated hypoperfused tissue state strongly correlates with post-operative infarct demarcation. Some tissue is located near well perfused arteries (green) and might indicate areas that may be affected by further ischaemic progression. Compared to the raw temperature image of **B** the results allow more detailed information regarding the tissue perfusion to be inferred.

The a priori unknown $\Theta = (\mu_i, \mu_u, \mu_h, \sigma_i, \sigma_u, \sigma_h)$ are estimated by the Expectation-Maximization algorithm. Lastly, the 3-GMM yields $p(\lambda_2^{\mathcal{S}} = \lambda_2; \Theta)$ which denotes the probability of λ_2 belonging to any of the expected classes. This allows the following greedy classification strategy:

$$\widetilde{s(p)} = \underset{s \in \mathcal{S}}{argmax}\ p(\lambda_2^{\mathcal{S}} = \lambda_2(p); \Theta) \qquad (5.6)$$

Each state's probability might be a reasonable indicator to infer further knowledge regarding the progression of the ischaemic demarcation.

5.1.3. RESULTS

We applied the proposed method to several cases suffering from severe ischaemic strokes that required decompressive craniectomy. The infarct demarcations were further segmented in pre- and postoperative CT measurements by a neurosurgeon. A qualitative evaluation of the resulting segmentations is based on the categories positive, questionable and negative. Two cases yielded rejected classifications caused by erroneous cortical irrigations, which enforces the requirement for more robust cooling protocol to prevent this issue from occur-

Case	Sex/Age	Pathology	Result	Comment
1	f/61	MCA infarct right	negative	too low contrast
2	f/61	MCA+ACA infarct right	negative	liquid hotter than surface
3	m/59	MCA infarct left	positive	
4	f/50	MCA infarct right	questionable	classification failed
5	f/63	vasoplastic infarct left	positive	
6	f/75	MCA infarct right	positive	

Table 5.1.: Overview of results from classifying the decay constant of tissue heating after application of an intraoperative cooling to the cortex.

ring. Analysis of one dataset yielded a questionable result, meaning that more tissue was classified as healthy than the CT infarct demarcations indicate. We suspect the necessity for more fine-grained classification of uncertain tissue states being related to this issue. In three cases we found a correlation of the segmented perfusion parameters with infarct demarcations as observed in pre- and postoperative CT measurements. The developed novel irrigation detection framework is based on optimized machine learning based detector to classify thermal characteristics of cortical irrigations with minimum delay. This detector allows us to quantify and analyze cortical perfusion (state) during cerebral infarction by a commonly used intraoperative approach, even in unperfused tissue. In conjunction with preoperative CT recordings, the framework provides the surgeon with information regarding the progression of infarct demarcations. The latter may be used a building block for research into future local intraoperative therapies.

5.2. SOMATOSENSORY ACTIVITY MONITORING BY SEMIPARAMETRIC REGRESSION (OW A.7)

Functional imaging is a common and important task in neuroscience (see section 2.2). In the case of brain tumor resections, high-grade anaplastic and infiltrative tumors are difficult to distinguish from healthy tissue. This task is especially difficult in case of a tumor near functional areas such as the primary somatosensory cortex. An exhaustive resection might lead to postoperative functional deficits and therefore decreased quality of life. This decrease might further affect the patient's mean survival time.

Established mathematical frameworks such as SPM allow the integration of specific experimental conditions into a linear model and apply statistical inference methods to recognize significant patterns correlating with neural activity. Our model is based on this idea, yet allows further integration of characteristic non-linear (noisy) patterns and time-behaviour of thermal imaging to occur, which would otherwise prevent reliable statistical inference.

5.2.1. SEMIPARAMETRIC MODELING OF DETERMINISTIC NEURAL ACTIVITY

Neural activity induces a neurovascular coupling chain (NVC) that leads to an increase of regional cerebral blood flow (rCBF) at functionally active sites. This change in rCBF also leads to small temperature changes that can be measured by thermal imaging. In the following, we extend prior findings of Gorbach et al.[34] by a sound mathematical model for thermographic

data and demonstrate the monitoring of somatosensory evoked activity. Generally speaking the semiparametric model consists of deterministic and random components. The random effects model high-frequent behaviour such as periodic motion and other artifacts, as well as the low frequent temporal drift behaviour. The method is described by the following steps:

1. NVC induces deviating thermal behaviour into thermal time courses caused by altered regional perfusion. This behaviour is typically propagated through several tissue layers. For this reason, we expect the thermal signal to resemble a smooth bell-like curve. We propose to approximate this curve with a Gaussian function with μ being the time-to-peak and σ the bell's width:

$$\frac{1}{\sigma\sqrt{2\pi}} exp((-(t_i - \mu)/2\sigma)^2) \tag{5.7}$$

2. The model contains two random effects with each resting upon B-Spline basis functions. The first random component consists of a very small number of knot points to approximate the low-frequent temporal drift. The second random component approximates unwanted high-frequent behaviour. The nonparametric random effects are modeled as degree k B-Spline by $Z_j = B._{,k}$ ($j \in \{1, 2\}$, see [20] for details). The experimental conditions are modeled as of repeated versions of equation 5.7 (depending on the actual experimental protocol) and plugged into X. All of them are stacked into $G = [X, Z_1, Z_2]$. In order to prevent the second component to account for low-frequent patterns and, in doing so, hiding the experimental conditions, we add an additional frequency penalty to the respective model formulation:

$$\min_{b} \|Gb - y\|_2^2 + \lambda\|PWGSb\|_2^2 \tag{5.8}$$

given the wavelet transformation matrix W and the signal estimate Gb containing fixed and random effects.

$$S = blkdiag(0_{noFixedEffects}, 1_{noRandomEffects}) \tag{5.9}$$
$$P = blkdiag(I_{128}, 0_{m-128}) \tag{5.10}$$

Finally, P and S restrict the penalty to lower wavelet scales (dyad 1 through 6) of the random effects to decrease the low-energy content of the respective estimate. The parameters can be estimated analytically by the penalized normal equations

$$\widehat{b}(\lambda) = (G^T G + \lambda S^T G^T W^T P^T PWGS)^{-1} G^T y \tag{5.11}$$

3. The non-uniformity correction of the thermal imaging system introduces regular discontinuity points into the data. To account for this issue, we estimate the temporal position t_js of each non-uniformity correction event and add an additional B-Spline knot at each t_j to the high-frequent B-Spline model. This approach introduces additional flexibility into the model since it is possible to account for steep changes at respective points in time.

4. Finally, hypothesis testing at Bonferroni corrected level α_{bonf} is employed to unveil statistically significant parameter estimates of the experimental conditions (see figure 5.2) that correlate with evoked neural activity.

5.2.2. RESULTS

The cohort consists of data recorded during tumor resection near the somatosensory cortex. The patients were under general anesthesia and focal activations were provoked by contralateral median nerve stimulations. The stimulation protocol consisted of 10 repeated 30 *s* stimulation and 30 *s* rest phases. Besides statistical analysis of thermal imaging data, further validation was accomplished by concurrent optical imaging measurements[60] allowing a qualitative comparison of the achieved results, by electrophysiological measurements (phase reversal) and anatomic localization of the estimated eloquent areas. We expect the accuracy of optical imaging to be better than thermal imaging since the method provides increased penetration depth compared to thermal imaging, yet at the cost of being sensitive to light scattering and reflection. In all cases we validated the occurrence of sensory activity on the exposed cortex by intraoperative phase reversal. The results of the proposed semiparametric regression framework are shown in table 5.2. By positive activation, we denoted a distinct statistically significant activation in thermal imaging (as shown in figure 5.2) and intraoperative optical imaging, whereas the focal activation centers correlated in both modalities. By weak activation, we denoted results with sparse clusters of active pixels whose spatial position correlates with optical imaging. Weak and positive classified results were further validated by their anatomic localization, meaning that this label is only preserved if the found eloquent site corresponds to the expected site being responsible for contralateral stimulations of median nerve. Negative means inconsistent results with thermal imaging, rejecting activity while optical imaging found activity. The only two negative results were caused by a suboptimal (skewed) orientation of thermal camera while the cortex showed strong convexity and Gyrus postcentralis being located at the boundary of the trepanation. All these suboptimal measurement conditions degrade the overall accuracy and therefore prevent the detection of weak signals.

We were able to successfully unveil statistically significant somatosensory activity with a new semiparametric regression framework that incorporates experimental conditions as well as artifacts of thermal imaging systems. The model further enables the scientists to adopt the experimental conditions to arbitrary stimulation protocols so that the application domain is not limited to the analysis of the primary somatosensory cortex. The surgeons get a tool to unveil and visualize cortical activity intraoperatively which, in the case of tumor resections near eloquent areas, supports the neurosurgical decision in terms of potential postoperative functional loss or limitations.

Case	Sex / Age	Pathology	Location	Preop. clinical condition	Activation TI	Comparison to IOI
1	m / 58	metastasis adeno-ca.	precentral l.	hemiparesis r. (4/5)	positive	correlation
2	f / 33	metastasis mamma-ca.	parietal l.	facioplegia	positive	no OI
3	m / 79	metastasis melanoma	frontoparietal r.	hemiparesis l. arm (3/5) l. leg (4/5)	weak	weak correlation
4	f / 72	glioblastoma	parietal r.	hemiparesis l. leg (3/5)	weak	correlation
5	m / 69	glioblastoma	parietooccipital l.	symptomatic seizures	positive	correlation
6	m / 72	astrocytoma grade III	parietal l.	hemiparesis brachiofacial	none	weak signal
7	f / 60	metastasis RCC	parietal l.	no paresis	weak	no OI
8	f / 70	glioblastoma	parietal l.	hypesthesia 4th and 5th finger r.	none	strong signal
9	f / 84	anaplastic meningioma	frontoparietal l.	progressing half-side-disability	positive	no OI

Table 5.2.: Results of intraoperative SSEP analysis.
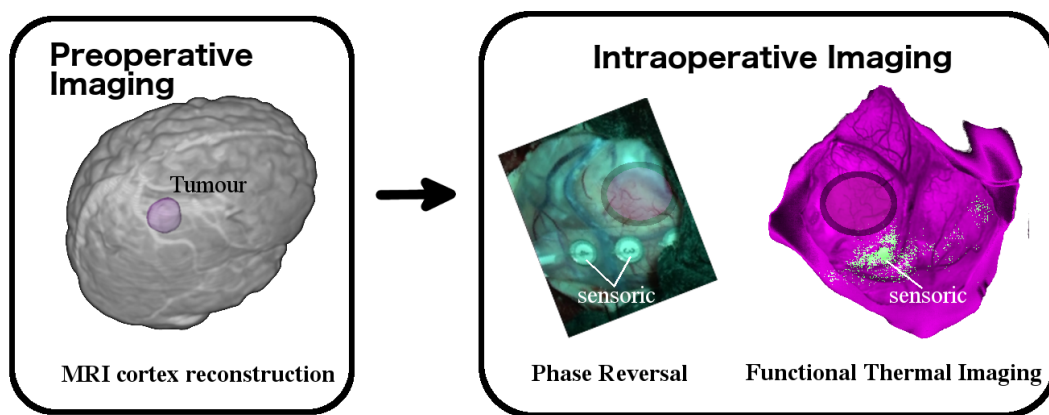
Figure 5.2.: The left image shows the 3D cortex reconstruction from a preoperative MRI dataset. The tumor is demarcated in purple color. Analyzing thermal imaging data with our novel semiparametric regression framework now allows us to unveil somatosensory activity at fine-grain resolution compared to prevalent phase reversal.

6. SUMMARY

Intraoperative thermal imaging is a neuroimaging technique that is based on measuring the body's emitted long-wave infrared radiation. This infrared radiation correlates with the object's temperature (Stefan-Boltzmann law). Modern, uncooled IR detectors are able to measure temperature gradients as low as 30 mK at spatial resolutions of 170 μm. In neurosurgery, the thermal radiation of the exposed brain depends on various metabolic as well as vascular factors. Analysis of each factor allows us to gain knowledge about their spatial distribution, spatial homogeneity and deviating behaviour. In contrary to existing methods, thermal imaging is a passive whitelight-independent, marker-free and passive technique which shortens lengthy and error-prone measurements and -protocols.

In this thesis we discussed the necessary extensions to establish thermal imaging as a flexible and robust neurosurgical decision support system. In order to improve predictive accuracy in respective application domains, thermal imaging specific challenges have to be characterized, modeled and corrected. The latter arise from various technical issues such as hysteresis effects caused by the microbolometer focal plane array of common thermal imaging devices. Periodic recalibration of the imaging system to prevent image distortions is another aspect that has to be modeled or corrected since the introduced points of discontinuity and non-uniform sampling of the thermal images would otherwise prevent meaningful statistical analysis.

Distinct artifacts are introduced to intraoperative thermal imaging by the initial orientation of the imaging device during the OP. With this orientation, the camera is set into a slight vibrational motion which introduces lateral shifts of the image plane. We approach these camera movement artifacts twofold. First, the actual error pattern is estimated and filtered by decomposing the signal in time-frequency domain using principal component analysis. This allows the detection of characteristic motion patterns that can then be integrated into subsequent analysis frameworks or just removed from the data. We extended this approach by a realtime motion correction scheme running on FPGA hardware. The lateral shift of the whole image is estimated by solving the object-based optical flow problem by least squares. The solution to this problem yields the shift in X and Y direction at small time steps which can then be used to interpolate motion free temperature values.

In order to correlate characteristic objects and functional information of preoperative volumetric scans (such as 3D MRI data) with results of intraoperative 2D imaging, we developed a multimodal image registration and image fusion framework. One application was demonstrated by joining intraoperative thermal imaging with preoperative 3D MRI recordings at a

mean accuracy of 2.46mm. This accuracy allows us to combine information of intraoperative measurements by thermal- or optical imaging with preoperative volumetric MRI data and integrate both into intraoperative neuronavigation systems. The latter means that multimodal and visually orthogonal information are integrated into a single view and then presented to the surgeon. This kind of visualization is crucial for intraoperative medical decision support systems since it decreases the required mental effort to correlate the results of all data and allows the medical personnel to focus on the gained actual medical information. Furthermore, we discussed a segmentation algorithm to isolate vessel structures in thermal imaging data by their characteristic thermal behaviour. In combination with recovering such structures in optical imaging data, feature-based co-registration of both modalities may be achievable so that the discussed 2D-3D framework is not limited to a single intraoperative 2D imaging device.

The proposed advances in analysis of intraoperative thermal neuroimaging data enhance and enable new application domains. In this work we focus on the characterization of dynamic thermal data of patients suffering from brain tumors and ischaemic strokes. Intraoperative differentiation of malign anaplastic tumor tissue imposes a challenging task, since the infiltrative growth hampers the decision about resection boundaries. The more tumor tissue is removed, the longer the patient's quality of life can be preserved, yet at the cost of potentially increased post-operative functional deficits. To decrease this risk, advanced methods for intraoperative differentiation of tissues and functional areas are required. Hence functional imaging techniques can be viewed as medical decision support systems that allow the surgeon to trade-off resection of potential tumor tissue with post-operative functional defects or respective limitations.

Contralateral somatosensory evoked potentials (SSEP) are a common method to provoke neural activity on the primary somatosensory cortex. Neural activity also causes weak changes in cortical perfusion that correlate with temperature changes in the emitted cortical heat. We analyze these temperature changes by an advanced semiparametric regression framework that incorporates deterministic experimental conditions and random components of low- and high-frequent background signals. The promising results were validated by concurrently acquired intraoperative optical imaging data. The latter approach was further improved by developing an advanced hardware setup for concurrent thermal and optical imaging with a single intraoperative microscope. To the best of our knowledge, we are the first to realize and use this kind of setup.

Ischaemic strokes, or shortages of neurons with blood, can cause severe long-term functional deficits if not treated appropriately. Various causes, such as blocked arteries or bleeding, can lead to a stroke. Each cause requires a specific treatment strategy. Severe strokes can cause a significant increase in intracerebral pressure that requires neurosurgical treatment by decompressive craniectomy. By providing new tools to quantify tissue perfusion, it is possible to monitor the progression of infarct demarcations. Another future aspect might be the localization of areas that may be subject to future specific local intraoperative therapies that preserve or even recover functionality. This long-term goal might decrease potential post-operative functional defects.

To approach these challenges, we developed a machine learning framework for online detection of intraoperative cortical NaCl rinsings. Cortical rinsings induce a temperature gradient to cortical tissue which is propagated into deeper tissue layers. After rinsing event classification, tissue heating is modeled and quantitatively analyzed to recover standardized perfusion parameters. In the case of patients suffering ischaemic strokes, the results indicate that the temperature decay time of heating processes allow conclusions about the tissue's perfusion

state to be drawn. We showed that these temperature decay constants correlate with the infarct demarcation, as seen in post-operative CT measurements of the same patient.

The methodical achievements of this thesis improve the predictive accuracy of thermal imaging and, in doing so, enhance and even allow novel demanding applications to be developed. Motion correction and multimodal image fusion depict important building blocks for medical decision support systems. The proposed semiparametric regression framework was employed to monitor somatosensory activity. The generic framework also enables the scientists to adopt the experimental conditions to arbitrary stimulation protocols so that the application domain is not limited to the analysis of the primary somatosensory cortex. Cortical activity is visualized intraoperatively to the surgeon, which in turn allows him to reason about potential postoperative functional deficits or limitations in the case of tissue resection.

The discussed approach to quantify cortical perfusion leads to a standardized representation of vascular processes. We expect that optimized rinsing protocols might allow more fine-grain differentiation of brain tissue in the future. Some experiments regarding tumor detection were already carried out and underline this potential future direction. The application of distributed parameter optimization schemes for the methods used in both application domains might be favorable extensions to decrease intraoperative delay. Distributed optimization might also allow the usage of the more complex Bioheat equations to model cortical and even subcortical tissue layers to establish intraoperative thermal tomography.

A. ORIGINAL WORKS

This work is based on several publications that were created by the author to solve several challenges ranging from motion correction to enabling novel intraoperative applications of thermal neuroimaging. The following publications describe the most significant achievements of this thesis in more detail. For this reason, we will provide a full-quote of these works.

A.1. CEREBRAL CORTEX CLASSIFICATION BY CONDITIONAL RANDOM FIELDS APPLIED TO INTRAOPERATIVE THERMAL IMAGING

N. Hoffmann, E. Koch, U. Petersohn, M. Kirsch, and G. Steiner. Cerebral cortex classification by conditional random fields applied to intraoperative thermal imaging. Current Directions in Biomedical Engineering. 2(1): 475-478, 2016.

Nico Hoffmann*, Edmund Koch, Uwe Petersohn, Matthias Kirsch, and Gerald Steiner

Cerebral cortex classification by conditional random fields applied to intraoperative thermal imaging

Abstract: Intraoperative thermal neuroimaging is a novel intraoperative imaging technique for the characterization of perfusion disorders, neural activity and other pathological changes of the brain. It bases on the correlation of (sub-)cortical metabolism and perfusion with the emitted heat of the cortical surface. In order to minimize required computational resources and prevent unwanted artefacts in subsequent data analysis workflows foreground detection is a important preprocessing technique to differentiate pixels representing the cerebral cortex from background objects. We propose an efficient classification framework that integrates characteristic dynamic thermal behaviour into this classification task to include additional discriminative features. The first stage of our framework consists of learning this representation of characteristic thermal time-frequency behaviour. This representation models latent interconnections in the time-frequency domain that cover specific, yet a priori unknown, thermal properties of the cortex. In a second stage these features are then used to classify each pixel's state with conditional random fields. We quantitatively evaluate several approaches to learning high-level features and their impact to the overall prediction accuracy. The introduction of high-level features leads to a significant accuracy improvement compared to a baseline classifier.

Keywords: intraoperative thermal imaging, 2D B-Spline, discrete wavelet transform, representation learning, conditional random fields, machine learning

*Corresponding Author: Nico Hoffmann: TU Dresden, Faculty of Medicine, Clinical Sensoring and Monitoring, Fetscherstraße 74, D-01062 Dresden, Germany. e-mail: nico.hoffmann@tu-dresden.de. Tel: +49 351 458 6443. Fax: +49 351 458 6325
Uwe Petersohn: Applied Knowledge Representation and Reasoning, TU Dresden, D-01062 Dresden, Germany
Edmund Koch, Gerald Steiner: Clinical Sensoring and Monitoring, TU Dresden, D-01307 Dresden, Germany
Matthias Kirsch: Department of Neurosurgery, University Hospital Carl Gustav Carus, D-01307 Dresden, Germany

1 Introduction

Intraoperative thermal neuroimaging denotes an non-invasive and contactless imaging technique that measures the emitted temperature radiation of tissue during neurosurgical interventions. In neurosurgery, temperature gradients derive from heat transfers being caused by (sub-)cortical perfusion and neuronal activity. Gorbach et al. [4] and Shevelev et al. [6] showed the application of intraoperative thermography for tumour diagnostics. Steiner et. al. [7] demonstrated the detection of a ice-cold saline solution applied through a central line as a tool for perfusion diagnostics.

High-level feature representations are extracted from data in time-frequency domain so that they unveil time-dependent thermal behaviour of the human cortex. We further evaluate two common approaches to this feature representation learning task and finally analyse their influence to the overall performance. Latter is also compared to a simple baseline method.

2 Methods

Dynamic thermal signals can be described by a combination of several non-stationary characteristic signal components. These components originate from physiological sources as well as from noise. To approach this challenge subsequent signal analysis and classification is done in time-frequency domain to decompose the signal into its characteristic time-dependent components. As the physiological influences of cortical and subcortical perfusion as well as tissue composition are unknown and difficult to estimate there is no parametric model about cortical heat emission. For what reason we propose a machine learning framework that extracts empirical knowledge from learning data using linear feature representation schemes for pixelwise latent state prediction. The research related to human use has been complied with all the relevant national regulations, institutional policies and in accordance the tenets of the Helsinki Declaration,

all intraoperative procedures in this work were approved by the Human Ethics Committee of the Technische Universität Dresden (no. EK 323122008). Informed consent has been obtained from all individuals included in this study.

2.1 Preliminaries

The global thermographic signal $T \in \mathcal{R}^{n \times m}$ respectively $T_i \in \mathcal{R}^m$ of any recorded pixel $1 \leq i \leq n$ and m time points is superimposed by several components such as physiological signals and thermic background noise $T^{bg} \in \mathcal{R}^{n \times m}$. In order to prevent learning background signals the latter component has to be separated from T prior to further analysis.

The approximation of background noise is done by exploiting its rather smooth nature by a two dimensional B-Spline model[1] to estimate and remove the background signal. Suppose we are given two one-dimensional B-Spline bases $B_{xy} \in \mathcal{R}^{m_1 \times n}$ and $B_t \in \mathcal{R}^{m_2 \times m}$ consisting of local B-Spline functions given m_1 and m_2 knots to interpolate the data in spatial B_{xy} and temporal B_t domain. Adjacent local B-spline functions are joined at m_1 resp. m_1 *knots* with $m_1 \ll n$ and $m_2 \ll m$. Let further $vec(T) \in \mathcal{R}^{nm}$ be the column stacked version of our measured temperature data T and $B_{2d} = B_{xy} \otimes B_t$ the tensor product $\otimes$ of both 1D B-Spline bases. The smooth background signal $T^{bg} = B_{2d}\widehat{\alpha}$ can now be estimated by regressing $vec(T) = B_{2d}\alpha$ using least squares given the normal equations:

$$\widehat{\alpha} = (B_{2d}^T B_{2d})^{-1} B_{2d}^T vec(T)$$

In order to catch dynamic thermographic effects that correlate with the actual imaged object subsequent analysis is done in time-frequency domain by applying the Discrete Wavelet transform to the data. Given a frequency band (scale) j, index k and wavelet ψ, the background corrected wavelet coefficients $c_i(j, k)$ of pixel i read

$$c_i(j, k) = \sum_j \sum_k (T_i(k) - T_i^{bg}(k)) 2^{-j/2} \psi(2^{-j} n - k)$$

The transformation is done in linear time using the fast wavelet transform based on pyramid algorithm. In the following we will drop (j, k) to simplify the notation if both are clear from context.

---

1 Further details regarding B-Spline regression can be found in [3], [2].

2.2 Representation Learning

Now we can proceed to finding a high-level representation of the thermal characteristics of our physiological signals. The representation should be robust to noise while preserving as much information as possible. In the following we will discuss two common approaches to learn a representation $f(c_i)$ of the wavelet transformed thermal data c_i.

2.2.1 Bag of Frequency Words

A common approach to unveil representative features is the bag of words model. In terms of wavelet coefficients $c_i \in \mathcal{R}^m$ for n pixels, we solve

$$\mu = \underset{\{\mu_1, \ldots, \mu_p\}}{argmin} \sum_{i=1}^n \sum_{\mu_j \in S_j} ||c_i - \mu_j||_2^2$$

and get representative frequency *words* $\mu_j \in \mathcal{R}^m$ that describe our training dataset. The k-Means algorithm provides one solution to this task, so that our dictionary μ is defined by $\mu = [\mu_1..\mu_p]^T$. This allows us to represent the L_2 distance of any new vector c_i to each of the p words $\mu_j \in \mathcal{R}^m$ $(1 \leq j \leq p)$ in terms of our dictionary $\mu = [\mu_1, \ldots, \mu_p]^T$ by

$$f(c_i) = ||c_i \otimes \vec{1}_p - \mu||_2^2$$

with length p column vector of ones $\vec{1}_p$ and $\otimes$ denoting the Kronecker product.

2.2.2 PCA

In the past, PCA was applied to learn a representation of neuroimaging data [5]. Suppose we measure n correlated m-dimensional wavelet transformed time-series stored as n rows in matrix $C \in \mathcal{R}^{n \times m}$. PCA now gives a set of m orthogonal vectors $v_j \in \mathcal{R}^m$ and weights $w_j \in \mathcal{R}^n$ with $1 \leq j \leq m$ so that $c_i = \sum_j w_j v_j$. It can be shown that these orthogonal vectors v_j correspond to the eigenvectors $\Phi = [v_1, v_2, \ldots, v_m]$ of the empirical covariance matrix $\Sigma_C = C^T C \in \mathcal{R}^{m \times m}$ so that $\Sigma_C \Phi = \Phi \Lambda$. Each eigenvector v_j now describes a characteristic high-level thermal behaviour of the data. The feature vector c_i of pixel i is represented by

$$f(c_i) = \Phi_p c_i \tag{1}$$

with $\Phi_p = [v_1 \ldots v_p]^T$ given dictionary size p.

(a) Thermal image of the cerebral cortex

(b) Cortex classification
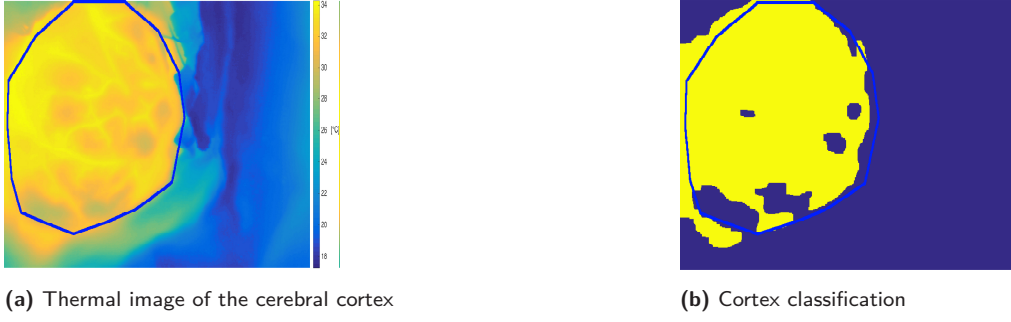
Figure 1: This validation dataset was subject to the PCA-CRF classifier and the results are shown in **(b)**. Yellow colour indicate pixels with label cerebral cortex. Expert classification of the cerebral cortex is indicated by the blue solid line in both images.

2.3 Learning Unary Potentials

Suppose each pixel i has latent state $y_i \in \mathcal{Y}$ given $f(c_i)$. In case of BoW, $f(c_i)$ denotes the distance of c_i to the learnt p representative frequency words μ_k (or analogously for the PCA approach v_k) with $1 \le k \le p$. The set of states $\mathcal{Y} = \{fg, bg\}$ now denotes the two classes of the pixels. Those pixels belonging to the cerebral cortex are classified as foreground (fg) the others as background (bg). The probability $p_i(y_i|f(c_i))$ of each pixel belonging to state y_i given the feature representation can now be learnt by a Random Forests (RF)[1] consisting of t decision trees. The trained RF yields a measure of certainty (probability) that an observed encoded representation $f(c_i)$ belongs to state y_i as of $p(y_i = fg|f(c_i))$ or $p(y_i = bg|f(c_i))$. An ensemble decision regarding the actual state y_i of the RF is obtained by averaging the output $p_i^k(y_i|f(c_i))$ of each single decision tree k:

$$p(y_i|f(c_i)) = 1/t \sum_{k=1}^{t} p_i^k(y_i|f(c_i))$$

The probability distribution is estimated by training each of the t decision trees on a bootstrap sample of our training data. This strategy effectively prevents overfitting as discussed by [1].

2.4 Structured Classification of Thermal Neuroimaging Data

In order to incorporate structural information into the classification process we propose a conditional random field (CRF) model. In this framework, the posterior distribution $p(Y|\mathcal{F}_\mathcal{C})$ of our latent variables $y_i \in \mathcal{Y}$ and observations $f(c_i) \in \mathcal{F}_\mathcal{C}$ can be formulated in terms of unary factors Ψ and pairwise factors ϕ on a undirected graph $G = (V, E)$ as of

$$log\, p(Y|\mathcal{F}_\mathcal{C}) = \sum_{i \in V} \Psi_i(y_i, f(c_i)) + \sum_{(i,i') \in E} \phi(y_i, y_{i'}) \quad (2)$$

with V being the set of pixels and E the set of edges between adjacent pixels i and i'. By fulfilling the local Markov property, this function can be factored so that $p(Y|\mathcal{F}_\mathcal{C})$ only depends on its direct neighbours. The unary potential $\Psi_i(y_i, f(c_i))$ encodes the prior probability learnt by the RF classifier whilst the pairwise potential $\phi(y_i, y_{i'})$ enforces spatial homogeneity of the inferred labelling. Computations were further simplified by integrating the regular structure of the imaged data through a Potts model function

$$\phi(y_i, y_{i'}) = C \cdot 1_{y_t = y_{t'}}$$

with indicator function $1_{y_t = y_{t'}}$ yielding one if $y_t = y_{t'}$ and zero otherwise. C is a smoothness penalty so that low values of C lead to rough solutions whilst the estimated labelling is getting smoother by increasing C. Since we are dealing with binary labels and Potts pairwise terms equation 2 is submodular what allows the application of very efficient inference method based on graph cuts. Minimizing equation 2 now corresponds to finding a maximum a-posteriori estimate of the labelling y.

3 Results and Discussion

The results were achieved by evaluating five intraoperative thermal measurements of five different cases of length 1024 frames (20 s). For this purpose thermal neuroimaging data was acquired just after exposure of the cerebral cortex during neurosurgical tumour resections. Three out of these datasets were used for training plus testing and two for validation. The training sample consists of 30% equally sampled data points of all three test datasets equally representing cortical and background pixels.

All computations were done on a workstation with dual Intel Xeon E5-2630, 128 GB Ram and Nvidia Geforce GTX Titan Black graphics card.

We evaluated both PCA and the Bag of Words model for feature representation learning. Baseline performance was quantified by training a RF on the average temperature distribution μT. The accuracy was computed by

$$acc = \frac{TC + TB}{C + B}$$

given multiple labeled datasets. TC denotes the number of true cortical-, TB the number of true background- and C as well as B represent the number of cortex and background pixels. These labellings were acquired by a medical expert. The results of both approaches are shown in tables 1 and 2. By introducing high-level features into the classification process a significant improvement in accuracy between the baseline classifier and the extended version can be observed. The introduction of learnt high-level thermal features provides additional discriminative information resulting from characteristic thermal signatures. Structural information shrink the difference in accuracy between our baseline classifier and the extended ones. This is caused by temperature inhomogeneities correlating with tissue composition and perfusion which are compensated by the Potts model. In the present cortex classification task this behaviour seems favourable. Yet, in case of smaller objects like tumours or vessels further attention has to be paid to this behaviour in order to achieve reasonable true-positive rates.

4 Conclusion

Intraoperative thermal neuroimaging is a novel technique to image time-dependent cortical temperature variations during neurosurgical interventions. The main cause of temperature changes is cortical perfusion which is influenced by cell metabolism and tissue composition. The thermal processes of the exposed brain are not well understood, yet they provide valuable information to characterize tissue. In this work thermal process signatures are employed to improve the differentiation of pixels of the cerebral cortex to background pixels. For this purpose we propose a novel machine learning framework for analysis of intraoperative thermal neuroimaging data. The learning goal is to recognize dynamic temperature behaviour of the imaged human cortex. These high-level features are then incorporated into a subsequent tissue classification stage based on conditional random fields improving overall classification accuracy. In the future, this framework

RF accuracy [%]	μT	BoW	PCA
test	86.4	93.1	<u>96.5</u>
validation	81.3	86.6	<u>88.1</u>

Table 1: The Random Forest classifier with PCA and BoW feature learning significantly outperform the baseline classifier on three training/testing as well as two validation datasets.

CRF accuracy [%]	μT	BoW	PCA
test	88.7	96	<u>98.5</u>
validation	87.7	89.1	<u>89.2</u>

Table 2: Extending the classifier by structural constraints further improves the overall accuracy of the baseline- and both feature learning approaches. For reasons of comparison the approaches were applied to the same data as described in table 1.

might enable a more fine-grain characterization of tissue composition based on its dynamic thermal behaviour.

Acknowledgment

References

[1] L. Breiman. Random forests. *Machine learning*, 45(1):5–32, 2001.

[2] M. Durban, I. Currie, and P. Eilers. Multidimensional P-spline Mixed Models : A unified approach to smoothing on large grids. 1(2006):2–5.

[3] P. H. Eilers, I. D. Currie, and M. Durban. Fast and compact smoothing on large multidimensional grids. *Computational Statistics & Data Analysis*, 50(1):61–76, Jan. 2006.

[4] A. M. Gorbach, J. D. Heiss, L. Kopylev, and E. H. Oldfield. Intraoperative infrared imaging of brain tumors. *Journal of Neurosurgery*, 101(6):960–969, 2004.

[5] H. Lu, K. N. Plataniotis, and A. N. Venetsanopoulos. MPCA: Multilinear principal component analysis of tensor objects. *IEEE Transactions on Neural Networks*, 19(1):18–39, 2008.

[6] I. A. Shevelev, E. N. Tsicalov, A. M. Gorbach, K. P. Budko, and G. A. Sharaev. Thermoimaging of the brain. *Journal of Neuroscience Methods*, 46(1):49–57, 1993.

[7] G. Steiner, S. B. Sobottka, E. Koch, G. Schackert, and M. Kirsch. Intraoperative imaging of cortical cerebral perfusion by time-resolved thermography and multivariate data analysis. *Journal of Biomedical Optics*, 16(1):016001–016001–6, 2011.

A.2. WAVELET SUBSPACE ANALYSIS OF INTRAOPERATIVE THERMAL IMAGING FOR MOTION FILTERING

N. Hoffmann, J. Hollmach, C. Schnabel, Y. Radev, M. Kirsch, U. Petersohn, E. Koch, and G. Steiner. Wavelet subspace analysis of intraoperative thermal imaging for motion filtering. Lecture Notes in Computer Science, 8815:411 – 420, 2014.

Wavelet Subspace Analysis of Intraoperative Thermal Imaging for Motion Filtering

Nico Hoffmann[1], Julia Hollmach[1], Christian Schnabel[1], Yordan Radev[2], Matthias Kirsch[2], Uwe Petersohn[3], Edmund Koch[1], and Gerald Steiner[1]

[1] Technische Universität Dresden, Department of Anesthesiology and Intensive Care Medicine, Clinical Sensoring and Monitoring, D-01307 Dresden, Germany
`nico.hoffmann@tu-dresden.de`
[2] Technische Universität Dresden, Department of Neurosurgery, D-01307 Dresden, Germany
[3] Technische Universität Dresden, Applied Knowledge Representation and Reasoning, D-01062 Dresden, Germany

Abstract. Intraoperative thermography allows fast capturing of small temperature variations during neurosurgical operations. External influences induce periodic vibrational motion to the whole camera system superimposing signals of high-frequent neuronal activity, heart rate activity and injected perfusion tracers by motion artifacts. In this work, we propose a robust method to eliminate the effects induced by the vibrational motion allowing further inference of clinical information. For this purpose, an efficient wavelet shrinkage scheme is developed based on subspace analysis in 1D wavelet domain to recognize and remove motion related patterns. The approach does not require any specific motion modeling or image warping, making it fast and preventing image deformations. Promising results of a simulation study and by intraoperative measurements make this method a reliable and efficient method improving subsequent perfusion and neuronal activity analysis.

1 Introduction

Thermal imaging is a contact-less, marker-free, white light independent and non-invasive method for online measurement of temperature variations up to 30 mK. Since thermography records the emitted heat of bodies, local dynamic behavior due to heat flow and convection effects are likely, leading to highly variate images even of static scenes. In neurosurgery, small temperature gradients are caused by perfusion or neuronal activity related heat transfers and respiratory and pulse motion of the exposed cortex. The neurosurgical application of thermography covers, among others, the detection of functional areas and brain tumors [1]. In a previous work, we have shown the direct link between temperature gradients and an injected ice-cold saline solution to investigate the cerebral blood flow [2]. Because of its temporal resolution, thermography might also allow inference about triggers of focal epilepsies.

The thermal imaging system is mounted at the operating table by an adjustable mount and a supporting arm. This supporting arm has three freely

Fig. 1. During Neurosurgery, the exposed human cortex can be easily identified by its warm and smooth temperature profile ($\geq 30°C$) in thermographic recordings. Yet, near cortical electrodes (arrow) or perfused blood vessels strong gradients are visible. Especially at these sites, vibrations of the camera system lead to a superposition of the time course of the affected pixels with time and neighborhood-dependent patterns, hampering subsequent data analysis.

orientable spheroidal joints enabling the surgeon to align the camera just before the recording. This setup makes intraoperative recordings at low object distances – typically 20 to 30 cm – feasible consequently minimizing the influence of background heat sources and allows spatial resolutions between 170 to 250 μm. This setup is prone to vibrations originating, among others, from the patient's respiratory motion and the surgeon's initial alignment of the camera. Such short-time periodic displacement of the whole thermographic camera leads to changing point-to-point mappings of consecutive thermographic images what introduces characteristic patterns into the data. This not only hampers the analysis of high-frequent neuronal activity or heart rate patterns in the same frequency band. Also thermographic signals of injected ice-cold saline solutions are overlain by these motion artifacts, especially in parenchyma near well perfused cortical arteries with strong temperature gradients, hampering their detection and hereby the analysis of cortical blood flow for medical decision support.

2 Related work

Digital video stabilization algorithms aim to eliminate unwanted motion artifacts from video streams, for example caused by hand-held cameras. Common approaches can be divided into intensity-based (direct) and feature matching algorithms. Latter match robust features of adjacent images to align the images [3] [4]. Intensity-based approaches in general minimize a cost function on the pixel's intensity to align the images or rather smooth the between-frame motion trajectory [5] [6]. Further subsequent analysis then allows the differentiation between local and global motion. A comprehensive review of image alignment methods can be found in [7].

Most of these approaches originate from whitelight imaging, which is an orthogonal modality to thermal imaging. Thermographic sequences inherit a nonstationary spatially varying heteroscedastic behavior, leading to local non-linear temperature shifts between adjacent frames, which is not necessarily related to

any motion. Pixels with strong temperature gradients can be superimposed by air flow or heat transfers, which is easily misinterpreted as motion of the affected areas. For robust and time-efficient correction of camera vibration artifacts, we therefore propose a signal based method. This multivariate post-processing approach is not affected by local motion artifacts, between-frame temperature dynamics or long term drifts and prevents unwanted image deformations. The analysis is carried into a sparse frequency domain and exploits the spatial characteristics of motion artifacts to identify respective frequency components.

3 Motion filtering in wavelet subspace

Temperature series contain non-linear trends and time varying frequency components at differing amplitude and frequency, for example at pulse or respiration frequency. Therefore, the time-resolved multi-resolution analysis is a desirable approach for the detection of dynamic frequency components. One such component originates from vibrations of the camera system, hereby inducing characteristic artifacts into the data. In what follows, the spatial distribution of the motion induced frequency pattern is exploited by pixel-wise change of basis into frequency domain by means of the 1D real-valued discrete wavelet transform (DWT) [8][4] and following subspace analysis using the Karhunen-Loève transform (KLT).

3.1 Feature description

Vibrations of the camera system lead to periodic translations of the whole image. The trajectory of these shifts is the same for all pixels of a single frame, whereas the amplitude of the artifact depends on the neighborhood of a pixel. To quantify this effect, the gradient image is examined. Let ∇I_c denote the gradient magnitude of the recordings first frame I at discrete pixel coordinate c. The set $\mathcal{X}^+$ contains the coordinates of a pre-specified amount of k pixels of maximum gradient, for example those indicated by the arrow in figure 1,

$$\mathcal{X}^+ = \arg\max_{\{c_1,...,c_k\}} \sum_i |\nabla I(c_i)|$$

while the counterpart $\mathcal{X}^-$ contains pixels of minimal gradient while being in a smooth neighborhood[5]

$$\mathcal{X}^- = \arg\min_{\{c_1,...,c_k\}} \sum_i |\nabla I(c_i)| \quad \text{subject to} \quad c_i \notin B_p(\mathcal{X}^+)$$

---

[4] There are complex valued extensions to the wavelet transform, for example CWT and dual-tree WT, yet these double the space requirements and are therefore not further considered here.

[5] $B_p(y)$ denote the n-dimensional p-ball of a space $\mathbb{M}$: $B_p(y) := \{x \in \mathbb{M} \mid ||x-y|| < p\}$. $B_p(\mathcal{Y})$ extends this definition to a set of p-Balls: $B_p(\mathcal{Y}) := \cup_{y \in \mathcal{Y}} B_p(y)$.
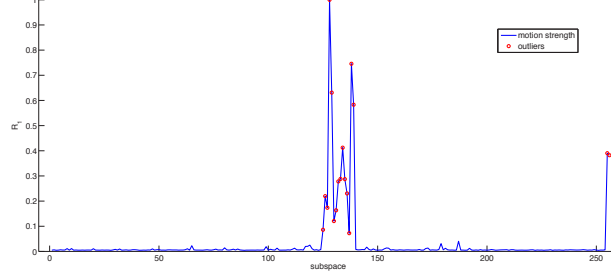
Fig. 2. The normalized motion impact R_n contains some strongly deviating values. These outliers indicate that the affected subspace inherits significant activity at locations with strong gradients caused by camera motion.

Smooth regions are described by low spatial gradients, thus if the spatial position of a single pixel is periodical changing in this neighborhood, only weak motion artifacts are induced into the time course.

3.2 Motion analysis

The time course of n pixels $X \in \mathbb{R}^{n \times m}$ with $m = 2^{j_{max}+1}$ frames contains various components with some being related to camera movement. In order to isolate time-varying motion artifacts, the data is pixel-wise projected into the sparse frequency domain by the DWT. Following, the KLT is used to identify global frequency patterns and quantify their local weight. The wavelet coefficients $X_F^j \in \mathbb{R}^{n \times 2^j}$ at scales $1 \leq j \leq j_{max}$ are projected into 2^j n-dimensional subspaces $W^j = [w_1^j \cdots w_{2^j}^j]$. The number of subspaces is determined by j and the KLT, since latter decomposes X_F^j into a linear combination of all 2^j eigenvectors, that are stored as columns of $\Phi \in \mathbb{R}^{2^j \times 2^j}$, of its empirical covariance matrix $\Sigma_{X_F^j}$. This change of basis into $W^j \in \mathbb{R}^{n \times 2^j}$ is done by $W^j = X_F^j \Phi$. Subspace w_i^j along with eigenvector $v_i^j \in \mathbb{R}^{2^j}$ describe the distribution of a frequency pattern, that contributes to the global variance of the respective wavelet coefficients at scale j weighted by its eigenvalue $\lambda_i \in \Lambda$. Hereby we are able to identify global patterns, that contribute to all pixels at varying extent. The local weight of pixel c in subspace i is denoted by $w_i(c)$. The mean contribution $w_i(\mathcal{Y})$ of specific pixels $y \in \mathcal{Y}$ to subspace i is given by

$$w_i(\mathcal{Y}) = \frac{1}{|\mathcal{Y}|} \sum_{y \in \mathcal{Y}} |w_i(y)|$$

For the identification of motion related subspaces, it is necessary to take the spatial characteristics of motion artifacts into account. For this purpose, the subspace contribution ratio r_i

$$r_i = w_i(\mathcal{X}^+) \; / \; w_i(\mathcal{X}^-)$$

is used to quantify the effect of motion artifacts at areas with strong gradients, like electrodes, cortical arteries or the boundary of the trepanation. Subspaces i related to camera motion artifacts show significant contributions $w_i(c)$ at pixels c in distinct neighborhoods, compared to pixels in smooth neighborhoods. This behavior leads to deviating r_i in the across subspace motion impact $R = (r_1, r_2, ..., r_{2^j})$ (see figure 2), which are subject to the subsequent detection scheme.

3.3 Outlier detection for subspace filtering

As discussed, frequency patterns related to motion artifacts have a characteristic spatial footprint, inducing outliers into R. For their identification, the motion impact $R = (r_1, r_2, ..., r_m)$ is modeled as a linear Gaussian random variable $R \sim N(aX + b, \sigma)$. Robust estimation schemes (e.g. iteratively reweighted least squares (IRLS)) are further needed, since R is expected to contain outliers making its variance heteroscedasticity. These outliers are found by applying a t-Test on the model residuals with respect to Bonferroni corrected significance level $\alpha = 0.05/m$.

This outlier detection scheme yields a set $\mathcal{K}$ of motion related subspace indices, that are now filtered by zeroing the weights of the respective subspaces $w_k = \mathbf{0}$ for all $k \in \mathcal{K}$. Lastly, the corrected data is recovered by back-projection from KLT space and inverse wavelet transformation. In order to halve the required maximum amount of memory, the algorithm is separately applied to each wavelet scale. The proposed motion correction scheme is sketched in algorithm 1. It assumes a periodized and orthogonal wavelet transform with symmlet4 basis, which is denoted by (I)DWT_PO_SYMM4.

4 Results

We will simulate deterministic motion conditions without heat flow and convection for performance comparison under optimal conditions. Afterwards, the proposed method is evaluated on two representative intraoperative cases, whereas case 1 inherits fast motion of large spatial extent and case 2 contains weak gradients leading to low amplitude motion artifacts while also having strong thermic dynamics. In order to compare the wavelet subspace analysis (WSA) with a common approach of whitelight imaging, matching of SURF features[6] is employed. Hereby, SURF features of a frame with respect to a reference frame or its motion corrected predecessor are matched[7] and an affine transformation matrix is computed to correct the motion artifacts. In order to further quantify the effect of the proposed outlier detection scheme, a one-class Support Vector Machine [10] (RBF kernel) is employed to infer unlikely values of R. Latter is

---

[6] SURF feature matching was done using the *matchFeatures* routine of Matlab implementing the nearest neighbor distance ratio method described by Mikolajczyk et al. [9].

[7] Best results are chosen.

Algorithm 1: Wavelet domain subspace motion correction algorithm.

    input: data set, $X \in \mathbb{R}^{n \times m}$

    input: number of gradient points, $k \in \mathbb{N}^+$

    output: motion stabilized data set, $X^* \in \mathbb{R}^{n \times m}$

    estimate pixel coordinate sets $\mathcal{X}^+, \mathcal{X}^-$ with $|\mathcal{X}^+| = |\mathcal{X}^-| = k$;

    $X_F = [X_F^1 \cdots X_F^{jMax}] = DWT\_PO\_SYMM4(X)$;

    for $j \leftarrow 1$ **to** j_{max} **do**

        $solve\ \Sigma_{X_F^j} \Phi = \Lambda \Phi^T$;

        $W^j = [w_1^j \ ... \ w_{2^j}^j] = X_F^j \Phi$;

        $\forall i \in [1, 2^j] \ : \ r_i^j = w_i^j(\mathcal{X}^+) \ / \ w_i^j(\mathcal{X}^-)$;

        $R^j = [r_1^j \cdots r_{2^j}^j]$;

        $\mathcal{K} = outlierDetection(R^j)$;

        $\forall k \in \mathcal{K} \ : \ w_k^j = 0$;

        $X_F^{j^*} = W^j \Phi^{-1}$;

    $X_F^* = [X_F^{1^*} \cdots X_F^{j_{max}^*}]$;

    $X^* = IDWT\_PO\_SYMM4(X_F^*)$;

denoted as *WSA-1SVM*, whereas the outlier detection approach of section 3.3 is denoted as *WSA-GT* and employs IRLS with a bisquare weighting function as robust estimation scheme.

For performance evaluation, an intensity-based as well as an frequency-based metric is employed. The root mean squared error (RMSE) quantifies to deviation of the estimated video $\widetilde{I}$ to the ground truth image sequence I. The average spectral density (SD) of all pixels $c \in \widetilde{I}$ describes the global energy content

$$SD = \frac{1}{|I| \times |fc|} \int \int_{2Hz}^{10Hz} \left| \int_{-\infty}^{\infty} |\widetilde{I}_c(t)| exp(-i\omega t) dt \right|^2 d\omega dc$$

of pixel intensities $I_c(t)$ at coordinate c, frame t and number of frequency coefficients $|fc|$ between 2 and $10Hz$. For reasons of comparison, the image sequences are cropped after the application of the motion correction schemes, since several rows and columns are lost after the application of SURF feature matching.

4.1 Simulation study

The expected camera motion is modeled as a sinusoidal coordinate displacement over time. Let $A(t) = I_3 = [a_1(t)^T a_2(t)^T a_3(t)^T] \in \mathbb{R}^{3 \times 3}$ be an affine transformation operator to simulate periodic displacement of $3D$ homogeneous coordinates

as a function of time t. Let further be $a_3(t) = (a_3(t)^1, a_3(t)^2, a_3(t)^3)$ the last column vector of A. Now define the periodic sinusoidal coordinate displacement at time t and displacement period p_d as

$$a_3^1(t) = a_3^2(t) = \gamma \sin(2\pi t/p_d)$$

This model is applied to a static thermographic image to simulate the expected behavior. The parameter γ allows for modeling the spatial extent[8] of the camera motion and is chosen from $[1;10]$, whereas the frequency p_d is fixed to 20 since its influence is negligible.

	$\gamma = 1$		$\gamma = 2$		$\gamma = 3$		$\gamma = 4$		$\gamma = 10$	
	RMSE	SD	RMSE	SD	RMSE	SD	RMSE	SD	RMSE	SD
SURF	0.03	26.71	0.06	10.74	0.08	143.31	0.1	56.6	0.21	36.17
WSA-GT	0.03	0.28	0.04	4.35	0.06	4.1	0.07	19.43	0.16	13.48
WSA-1SVM	0.03	0.33	0.04	4.23	0.06	12.94	0.07	19.53	0.16	13.48

Table 1. Evaluation of mean-squared error and integrated frequency band of the proposed simulation study. For this a static thermographic frame of case 1 was continously shifted by the discussed periodic motion model.

The results indicate the applicability of motion correction approaches from whitelight imaging to thermographic image sequences of the simulation model when no heat transfers or convection are prevalent. Real data typically show non-stationary and highly dynamic development, for what reason the feature-based approach will lose performance. Since the subspace analysis exploits more information about the motion pattern, its better performance is not surprising.

4.2 Intraoperative data

The algorithms are applied to raw recordings of two intraoperative cases and the average spectral density is compared. The evaluation of the RMSE is discarded, since the ground truth is a dynamic time-varying unknown. The first case was recorded during an intraoperative ECoG measurement of a patient with suspicion of frontal lobe epilepsy, wherein high-frequent vibrations of the camera system at a spatial extent of 5 pixels ($\sim$ 1cm) are recognizable. After application of the methods the motion visually disappeared, yet the SURF corrected dataset contains some deformed frames caused by mismatched features. Case 2 denotes a tumor case whereas less motion but strong spatial varying thermic background activity is dominating the data. This leads to a mean temperature drift of 0.45K in 41s at an average activity of $\sigma = 0.2435$K. An increase of the SURF point detection threshold several times was necessary, since no feature matching between adjacent frames was possible. Hereby, enough corresponding

---

[8] Intraoperative, $\gamma = 10$ depicts a maximum displacement of 5cm.
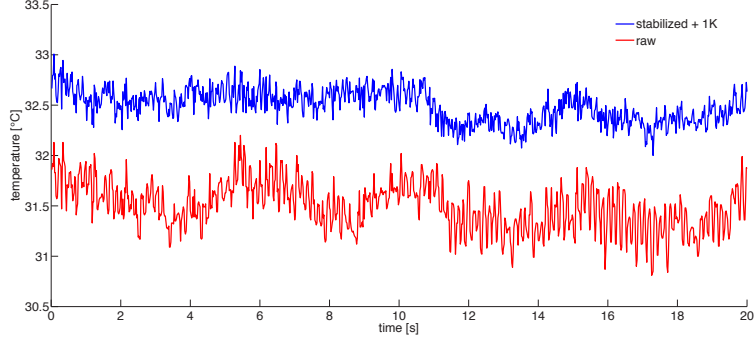
Fig. 3. Example of a single pixel time course of case 1 before (lower curve) and after motion correction (upper curve, increased by 1 K for visual reasons).

features were found, yet the estimated transformation matrix was prone to errors yielding skewed frames. In contrary, in both datasets, the wavelet subspace analysis was not affected by respiratory, heart rate and other local motion artifacts or thermic background activity. This results in a higher reduction of energy content in the relevant frequency band as shown in table 2 and a visual disappearance of global motion.

The average spectral density in the high-frequency band of case 1 and case 2 was significantly lowered after the application of the wavelet subspace analysis approach, yet some activity was preserved suggesting local activity independent of camera motion artifacts. Further contrast analysis of the video sequences of case 1 shows, that wavelet subspace analysis lowers the mean contrast[9] of the raw video $\bar{c} = 0.0741$ ($\sigma = 0.0012$) to $\bar{c}_{wsa} = 0.0732$ ($\sigma_{wsa} = 0.0012$) while the SURF approach resulted in $\bar{c}_{SURF} = 0.0694$ ($\sigma_{SURF} = 0.004$). This indicates, that some smoothing was introduced, yet since thermographic images do not show sharp edges, the visual effect is considerably small and the gain in data quality dominates. In case of SURF feature matching, the high variance and low mean contrast is expected to be caused by mismatched features resulting in non-perfect geometric transforms and therefore wrongly interpolated pixel values. A retrospective global optimization over the matched SURF features might improve the quality of the estimated transform and yield better results. Furthermore, the accuracy of wsa strongly depends on features that introduce gradients into the thermal images, thus if no such features are detectable, the algorithm will not work efficiently. Yet, since the boundary of the trepanation of the cortex is always visible, this situation is negligible.

The mean per-frame computation time was 0.08s (SURF), 0.04s (WSA-1SVM) and 0.06s (WSA-GT), whereas it is important to notice that the wavelet

---

[9] The mean contrast is computed by $\bar{c} = \frac{1}{|T| \cdot |\mathcal{C}|} \sum_{t \in T} \sum_{c \in \mathcal{C}} \nabla I_c(t)$ over all pixels $c \in \mathcal{C}$ and frames $t \in T$.

spectral density	uncorrected	SURF	WSA-GT	WSA-1SVM
Case 1	7541.724	1952.466	1285.724	1279.722
Case 2	1951.909	116347.54	927.683	937.244

Table 2. Evaluation of average spectral density of the algorithms with respect to two intraoperative cases.

subspace analysis requires a dyadic length sequence of frames as input, while SURF feature matching allows registration of subsequent frames. Yet, a global optimization to improve SURF feature matching will affect this advantage. Since the fast wavelet transform has linear complexity, the KLT primary contributes to the time-complexity of WSA by the eigenvalue decomposition of the covariance matrix at each wavelet scale:

$$\Theta(n \sum_{j=1}^{j_{max}} 2^{2j}) \approx \Theta(2n2^{2j_{max}})$$

with n pixels and highest wavelet scale j_{max}. The performance of WSA-GT and WSA-1SVM is comparable, whereas the time-complexity of IRLS significantly affects the runtime making the one-class SVM the better outlier detection scheme.

The mounting of the camera at the operating table decreases the degrees of freedom of the camera movement trajectory. This constrains the motion artifacts to short-term quasi-periodic behavior (see figure 3), which affects all pixels and can be identified and removed by exploiting its multi-resolution- and spatial characteristics. In general, the results on intraoperative as well as on synthetic data demonstrate the advantages of the wavelet subspace analysis. The proposed posterior removal of global camera movement artifacts in frequency domain is therefore a reliable and fast method for compensation of this kind of artifacts. This makes the proposed approach a valuable tool for intraoperative decision support systems.

5 Conclusion

Vibrational motion of the whole camera system leads to a degradation of signal to noise ratio. Common image stabilization algorithms cannot be employed directly to thermal imaging since the data originates from the emitted mid to long-wavelength infrared radiation of the captured objects making it highly dynamic. Heat flow, convection, perfusion as well as neuronal activity are typical causes of temperature variations causing image gradient changes that do not relate to any change of the observed scene. We therefore propose a robust and fast framework for the identification of global frequency patterns by analyzing their spatial distribution. One application of this approach is the estimation and removal of camera motion artifacts. This roots on the assumption, that motion artifacts can be described in sparse time-frequency domain of all pixels at varying power depending on their local neighborhood. A simulation study was

done in order to compare the approach with a well known method from white-light imaging for video stabilization under deterministic conditions. The results of this study as well as intraoperative data clearly suggest the application of the wavelet-subspace analysis framework for posterior global motion correction. Since the general framework is expendable by adapting the feature selection step to domain specific needs, its applications for the compensation or extraction of other kinds of spatially characteristic patterns are possible.

Acknowledgment

References

1. A. M. Gorbach, J. D. Heiss, L. Kopylev, and E. H. Oldfield, "Intraoperative infrared imaging of brain tumors," *Journal of Neurosurgery*, vol. 101, no. 6, pp. 960–969, 2004, pMID: 15599965.
2. G. Steiner, S. B. Sobottka, E. Koch, G. Schackert, and M. Kirsch, "Intraoperative imaging of cortical cerebral perfusion by time-resolved thermography and multivariate data analysis," *Journal of Biomedical Optics*, vol. 16, no. 1, pp. 016 001–016 001–6, 2011.
3. S. Battiato, G. Gallo, G. Puglisi, and S. Scellato, "Sift features tracking for video stabilization." in *Image Analysis and Processing, 2007. ICIAP 2007. 14th International Conference on*, 2007, pp. 825–830.
4. R. Hu, R. Shi, I. fan Shen, and W. Chen, "Video stabilization using scale-invariant features," in *Information Visualization, 2007. IV '07. 11th International Conference*, July 2007, pp. 871–877.
5. A. Litvin, J. Konrad, and W. C. Karl, "Probabilistic video stabilization using kalman filtering and mosaicking," in *Proceedings of SPIE Conference on Electronic Imaging*, 2003.
6. Y. Matsushita, E. Ofek, W. Ge, X. Tang, and H.-Y. Shum, "Full-frame video stabilization with motion inpainting," *IEEE TRANSACTIONS ON PATTERN ANALYSIS AND MACHINE INTELLIGENCE*, vol. 28, 2006.
7. R. Szeliski, "Image alignment and stitching: A tutorial," Microsoft Research, Tech. Rep., 2006.
8. S. Mallat, *A Wavelet Tour of Signal Processing*, 3rd ed. Academic Press, 2008.
9. K. Mikolajczyk and C. Schmid, "A performance evaluation of local descriptors," *Pattern Analysis and Machine Intelligence, IEEE Transactions on*, vol. 27, no. 10, pp. 1615–1630, Oct 2005.
10. B. Schölkopf, J. C. Platt, J. C. Shawe-Taylor, A. J. Smola, and R. C. Williamson, "Estimating the support of a high-dimensional distribution," *Neural Comput.*, vol. 13, no. 7, pp. 1443–1471, Jul. 2001.

A.3. MOTION CORRECTION OF THERMOGRAPHIC IMAGES IN NEUROSURGERY: PERFORMANCE COMPARISON

V. Senger*, N. Hoffmann*, J. Müller, J. Hollmach, C. Schnabel, Y. Radev, J. Müller, M. Kirsch, U. Petersohn, G. Steiner, E. Koch, and R. Tetzlaff. Motion correction of thermographic images in neurosurgery: Performance comparison. In Biomedical Circuits and Systems Conference (BioCAS), pages 121 – 124, 2014. [* both authors contributed equally to this work.]

Motion Correction of Thermographic Images in Neurosurgery: Performance Comparison

Vanessa Senger§, Nico Hoffmann*, Jens Müller§, Julia Hollmach*, Christian Schnabel*, Yordan Radev†,
Jan Müller§, Matthias Kirsch†, Uwe Petersohn‡, Gerald Steiner*, Edmund Koch* and Ronald Tetzlaff§

*Clinical Sensing and Monitoring,
Faculty of Medicine, Technische Universität Dresden, Dresden, D-01307 Germany.
Email: nico.hoffmann@tu-dresden.de
†Department of Neurosurgery, University Hospital, Technische Universität Dresden, Dresden, D-01307, Germany
‡Applied Knowledge Representation and Reasoning,
Faculty of Computer Science, Technische Universität Dresden, Dresden, D-01062 Germany
§Chair of Fundamentals of Electrical Engineering,
Faculty of Electrical and Computer Engineering, Technische Universität Dresden, Dresden, D-01062 Germany.
Email: vanessa.senger@tu-dresden.de

Abstract—**In this paper, the correction of motion-induced high frequency artifacts on sequences of thermographic images by a real-time capable approach based on Cellular Nonlinear Networks (CNN) is evaluated. For comparison, an offline analysis of frequency subspaces is presented and results will be compared. Both simulated data sets as well as data sets recorded during neurosurgery are considered as inputs and two measures are evaluated.**

I. Introduction

A. Medical Applications of Thermography

Thermography is an imaging technique for contactless, marker-free and non-invasive measurement of temperature variations. Current devices employ infrared microbolometers that detect long-wave infrared radiation. Emission of such radiation depends on the object temperature and – in case of non-black body objects – on its emissivity. The microbolometers are arranged as a focal plane array, providing a spatially-resolved temperature image. Convection and other heat transfers primarily cause temperature gradients, making thermography a highly stochastic and nonlinear imaging process.

In medical applications, characteristic changes in tissue perfusion support the diagnosis of anomalies such as fever, breast cancer and vascular disorders [1]. Neuronal activity and cerebral perfusion can be detected based on thermographic imagery obtained during neurosurgery. This allows the detection of functional areas and brain tumors [2]. Additionally, we investigated the spatio-temporal distribution of an injected ice-cold saline solution and were able to extract information on cerebral blood flow [3].

For intraoperative recordings, the thermographic camera is mounted at the operating table using a supporting arm and an adjustable mount. This setup enables the surgeon to align the camera just before the measurement. Since the supporting arm is connected to the operating table, it is prone to vibrations. Thermographic signals of neural activity and perfusion changes have low signal-to-noise ratios. Because of this, the motion-induced artifacts hide valuable diagnostic information and hamper further applications of thermography as a medical decision support system. Therefore, the detection and removal of those artifacts is the first step in any analysis of data obtained during neurosurgery. As our aim is to realize an integrated device capable of recording and analyzing thermographic data in real time during neurosurgery, a real time capable motion artifact filtering is necessary.

B. Cellular Nonlinear Networks

The concept of CNN was introduced by Chua and Yang in 1988 [4]. CNN are constructed from comparatively simple dynamical systems – cells – which are locally coupled. Even though there are no restrictions regarding coupling laws and dynamics, translation invariant state equation known as the standard CNN equation is used. It is given by

$$\dot{x}_{ij}(t) = -x_{ij}(t) + \sum_{|k|,|l| \le r} a_{kl} \cdot y_{i+k,j+l}(t) + w_{ij}, \quad (1)$$

with the offset

$$w_{ij} = \sum_{|k|,|l| \le r} b_{kl} \cdot u_{i+k,j+l} + z. \quad (2)$$

The term x_{ij} denotes the state, y_{ij} the output, z a constant bias and u_{ij} the input of the cell C_{ij}. Considering a neighborhood radius of $r = 1$, a standard CNN can be described by input and output weights and a bias z which form a set of 19 parameters. Despite their simple structure, CNN are well suited to modeling complex behavior far beyond that of a single cell.

Due to its massively parallel processing, CNN hardware implementations and FPGA emulations combine high computational performance with low electrical power consumption. Therefore, an implementation of a movement correction algorithm on CNN hardware is a promising first step towards a platform capable of providing intraoperative feedback to a

surgeon.

II. METHODS

Video image stabilization in white light imaging is a well-researched field with a broad range of approaches to re-aligning adjacent images or smoothing motion trajectories [5]. Yet, the preconditions of algorithms tailored to white light imaging do not necessarily apply to thermal imaging because of its highly stochastic nature. In this work we therefore present an offline method to efficiently circumvent this problem in real time.

A. Offline Motion Artifact Filtering

At pixel level, unaligned frames induce artifacts with varying intensity into the time course of the data, whereas the error depends on the smoothness of the local neighborhood. Suppose we have two sets, $\mathcal{X}^+$ and $\mathcal{X}^-$, containing coordinates of pixels with distinct ($^+$) and smooth ($^-$) neighborhoods and we have a measure $w(\mathcal{X})$ of motion artifacts, then the ratio

$$r = w(\mathcal{X}^+)/w(\mathcal{X}^-)$$

is maximized in case of present camera motion artifacts.

Let $X \in \mathbb{R}^{n \times m}$ denote the measurement matrix consisting of n pixels at $m = 2^{j_{max}+1}$ equally-spaced sampling points. The pixel wise 1-D discrete wavelet transform[1] of this matrix at wavelet scale $1 \leq j \leq j_{max}$ is denoted by $X_F(j) \in \mathbb{R}^{n \times 2^j}$. At each scale, $X_F(j)$ is superimposed by several signals with camera motion artifacts among them. In order to filter motion artifacts, the wavelet transform of scale j is decomposed into 2^j subspaces w_i by means of the Karhunen-Loève-Transform (KLT). The decomposed wavelet transform is denoted by $W(j) = [w_1 \cdots w_{2^j}]$ with

$$W(j) = \Phi X_F(j)$$

and the matrix Φ with the eigenvectors of the empirical covariance matrix $\Sigma_{X_F(j)}$ as its columns. In order to quantify the assumed motion artifacts to subspace i, the average energy contribution $w_i(\mathcal{Y})$ of subspace i at pixel coordinates $y \in \mathcal{Y}$ is formed. The subspace motion impact $R(j) = \{r_1, r_2, \cdots, r_{2^j}\}$ with

$$r_i = w_i(\mathcal{X}^+)/w_i(\mathcal{X}^-)$$

now models the intensity of motion artifacts in i.

Despite their amplitude, motion artifacts show location independent frequency characteristics, resulting in a small subset of all subspaces (their indices are elements of a set $\mathcal{K}$ with $|\mathcal{K}| \ll 2^j$) of frequency patterns related to camera motion [6]. This allows the application of 1-D outlier detection schemes on R to find deviating $r_k \in R$ (compare [7]). The respective w_k are then filtered by $w_k = \vec{0}$ and the motion corrected data is back-projected from KLT-space and by inverse wavelet transform.

[1]In this work, we employ a periodized and orthogonal DWT with Symmlet4 basis. Since each wavelet scale spans a unique time-frequency space, the scales are analyzed independently to save computational time.

B. Optical Flow Estimation & Motion Compensation

1) Algorithm: A real-time motion correction algorithm should be suitable to be implemented on an FPGA-based CNN hardware. Our approach is based on the estimation of the optical flow in the images. With the assumption that the intensity change of the frames is slow compared to the motion, a translation $(\Delta x, \Delta y)$ of a pixel can be calculated using the equation of the optical flow given by

$$(I(x,y,t+1) - I(x,y,t)) \approx \frac{\partial I}{\partial x}\Delta x + \frac{\partial I}{\partial y}\Delta y \quad (3)$$

and defined for each pixel of the image. Obviously, the resulting equation system is under-determined and can only be solved by taking into account conditions like smoothness or discontinuity. [8]

A direct estimation of the optical flow is sensitive to noise and low image contrast. Therefore a different, object based approach is used. Assume a simple object moving in front of a uniform background. If the shift of f_i to a reference frame f_r is constant over all pixels $p \in w$ within a given window $w \in f_i$, the equation system

$$\begin{bmatrix} I_1(t+1) - I_1(t) \\ \vdots \\ I_N(t+1) - I_N(t) \end{bmatrix} = \begin{bmatrix} \frac{\partial I_1}{\partial x} & \frac{\partial I_1}{\partial y} \\ \vdots & \vdots \\ \frac{\partial I_N}{\partial x} & \frac{\partial I_N}{\partial y} \end{bmatrix} \cdot \begin{bmatrix} \Delta x \\ \Delta y \end{bmatrix} \quad (4)$$

for all N pixels $p \in w$ can be formulated by using a bi-linear estimation for subpixel shifts. Here, I_p denotes the intensity of the image at pixel p.

Let K_y and K_z denote the sum of all partial derivatives of all pixels in the window. By formulating the equation system (EQS) (4) for two suitable windows w_1 and w_2 and adding up the equations, a modified EQS

$$\begin{bmatrix} K_{XR} \\ K_{YR} \end{bmatrix} = \begin{bmatrix} K_{X1} & K_{Y1} \\ K_{X2} & K_{Y2} \end{bmatrix} \cdot \begin{bmatrix} \Delta x \\ \Delta y \end{bmatrix} \quad (5)$$

can be derived and solved directly, where $K_{XR} = \sum_{p \in w_1} I_p(t+1) - I_p(t)$ and $K_{YR} = \sum_{p \in w_2} I_p(t+1) - I_p(t)$, respectively. In order to obtain higher robustness of the algorithm, four direction-sensitive windows are selected instead of just two, and the resulting EQS is then solved using a least-squares approach. The derived shifting vector $(\Delta x, \Delta y)$ can then be applied to correct the motion.

2) Window Selection: The algorithm proposed here relies on the sensitivity and specificity of the selected windows with respect to movement in x and y directions, respectively. In order to automatically obtain such windows, a calibration procedure is carried out in suitable intervals – later to be synchronized with shuttering of the thermographic camera – throughout the motion correction. Executing a threshold operation using decreasing bias values followed by an edge detection will lead to an increasing number of remaining black pixels p_b in the image. Once the sharp edge between cortex and surrounding background is reached, p_b decreases as remaining holes are filled. After all holes have been filled, a local minimum $min(p_b)$ is reached. The number of black pixels

will increase again once the shape obtained after thresholding surpasses the cortex.

The shape after thresholding at the local minimum $min(p_b)$ is selected, remaining holes are filled, after which suitable windows are extracted by applying a sobel filter in the desired direction and enhancing the resulting lines by several pixels.

3) CNN-based Implementation: A flow diagram of the algorithm is depicted in Fig. 1. After initialization and calculation of the pixel sums K_{XR}, K_{YR} over the reference frame f_{ref}, a frame f_i is shifted by shifting vector V_{t-1} obtained for the previous frame. Afterwards, window sums K_X, K_Y for f_i are calculated, the resulting EQS (5) is solved for the current shift vector V_t. It is then applied and used for updating V_{t-1}.
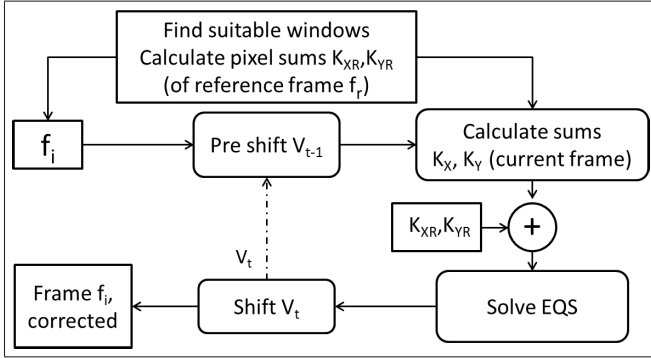

Fig. 1. Flow chart of the execution of the algorithm. After a pre-shift, window sums K_x, K_y are calculated and the EQS is solved for shift V_t.

The algorithm has been implemented on a recently-proposed CNN hardware platform that is suitable for high-speed and real-time signal processing using the massively parallel NERO architecture [9]. The architecture is considered a very efficient and performant digital emulation of CNN dynamics. Based on this architecture, an FPGA prototyping system has been built using a Xilinx Zynq-7000 AP System-on-Chip (SoC).

For performance analysis, we implemented two different hardware configurations, each emulating a network of 640×480 cells using 640 processing elements (PE). In configuration 1, a common 8 bit data width is used, allowing a clock frequency of 150 MHz on the Xilinx XC7Z045 FPGA. The data precision is increased to 12 bit in configuration 2, accompanied by a very high utilization of on-chip memory. The achievable clock for this configuration is 100 MHz.

Although the algorithm is running correctly in principle when implemented on the 8 bit hardware platform, the numerically induced quantization error outweighs the advantage of the stabilized image data. In accordance with offline fixed-point simulations, a data precision of at least 12 bit has turned out to be necessary for a robust hardware implementation of the proposed algorithm. Even further increasing the internal data precision does not necessarily result in a better performance, as the underlying thermographic data is containing a considerable amount of noise and is affected by a time-dependent global temperature drift.

TABLE I
COMPUTING TIMES OF THE CNN ALGORITHM IMPLEMENTED ON AN FPGA HARDWARE PLATFORM.

Task	Conf. 1: 8 bit	Conf. 2: 12 bit
Pre-shift V_{t-1} [*]	0.7 ms	1.8 ms
Get K_X, K_Y [*]	3.3 ms	9.6 ms
Shift V_t [*]	0.7 ms	1.8 ms
Solve EQS [+]	2 μs	2 μs
Others [+]	4 μs	4 μs
Correction total	**4.7 ms**	**13.3 ms**

Tasks performed by the CNN kernel are marked [*]

Tasks performed by the ARM coprocessor are marked [+]

Some high-level computing tasks, like solving the EQS and the calculation of the actual shift vectors from (5), are performed on an ARM processor embedded in the FPGA. However, most of the computation is assigned to the CNN processor. A performance estimation of the algorithm implemented on the respective hardware configurations is given in Table I.

III. RESULTS

In the following, results for both the wavelet based offline motion artifact filtering (WSA) and the proposed CNN approach (as matlab implementation) are presented. Firstly, the performance is analyzed based on synthetic data with varying shift of fixed frequency and increasing amplitude. Secondly, both movement correction procedures are applied to two real data sets recorded during neurosurgery.

In order to compare results, two measures are considered. For synthesized data, the summed-up frame-wise root mean squared error (RMSE) is calculated. Additionally, the average spectral density (SD)

$$SD = \frac{1}{N} \int \int_{2\,\mathrm{Hz}}^{10\,\mathrm{Hz}} \left| \int_{-\infty}^{\infty} |I_c(t)| \, exp(-i\omega t) dt \right|^2 d\omega dc \quad (6)$$

with

$$N = |I| \times |f_c| \quad (7)$$

of pixel intensities $I_c(t)$ at coordinate c, frame t and number of frequency coefficients $|f_c|$ between $2\,\mathrm{Hz}$ and $10\,\mathrm{Hz}$ is considered.

In intraoperative recordings, the undesired high frequency movements overlay with breathing, pulse and other physiological effects that interfere with movement correction. The RMSE is particularly sensitive to slow changes of image series caused by such effects, and will therefore only considered as a performance measure for synthesized data sets.

A. Synthetic data

In order to simulate the camera motion, we define a time-dependent affine transformation matrix

$$A(t) = I_3 = [a_1(t)^T a_2(t)^T a_3(t)^T] \in \mathbb{R}^{3 \times 3} \quad (8)$$

of homogeneous coordinates with $a_i(t) = [a_i^1(t)\ a_i^2(t)\ a_i^3(t)]$. The periodic displacement of adjacent frames in x and y direction is modeled by

$$a_3^1(t) = a_3^2(t) = \gamma sin(2\pi t/p_d)$$

at time t and displacement period p_d. Using γ we parametrize the spatial extent of the camera motion. In the following, we assume a fixed frequency and compare the approaches at varying γ.

TABLE II
RMSE AND SD FOR SYNTHESIZED DATA WITH A MAXIMUM
DISPLACEMENT OF $0.2\,\mathrm{cm}(\gamma = 1)$, $0.4\,\mathrm{cm}(\gamma = 2)$, $0.6\,\mathrm{cm}(\gamma = 3)$.

	$\gamma = 1$		$\gamma = 2$		$\gamma = 3$	
	RMSE	SD	RMSE	SD	RMSE	SD
WSA	0.03	0.28	0.04	4.35	0.06	4.1
CNN	0.09	141	0.33	780	0.44	2615

The CNN based approach is highly sensitive to the maximum amplitude of the synthetically induced movement. Therefore, results for both RMSE and SD in Tab. II diverge by several magnitudes. However, artifacts caused by camera movements observed in real data sets are usually quite small. Therefore, two typical examples of real data sets will be used to further evaluate the data.

B. Intraoperative Data

Two exemplary cases are used to further evaluate the methods. Fig. 2 shows the frame-wise RMSE of a sequence of 240 frames from case 1, corresponding to $5.8\,\mathrm{s}$ in time. For uncorrected data, high-frequency oscillations caused by camera movements can be seen in addition to slower changes of the frame-wise RMSE; therefore an average RMSE value will be omitted in Tab. III. In this typical example, the motion-induced artifacts are effectively removed after the application of both methods.
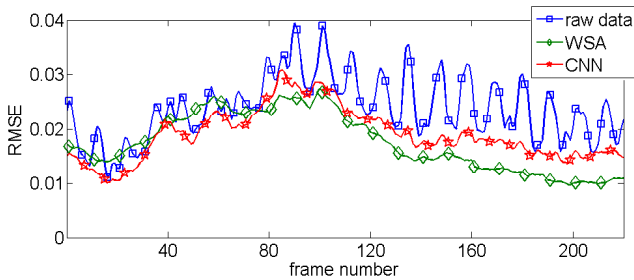

Fig. 2. Framewise RMSE of raw data (blue, $-\square-$), WSA-corrected data (green, $-\diamond-$), CNN-shift-corrected data (red, $-\bigstar-$).

The average SD values can be found in Tab. III. For case 1, the value of the SD for uncorrected data is around 3.8 times higher than for case 2. Here, it is important to compare results after movement corrections to the SD value obtained for raw data – in real data sets, the undesired high frequency

TABLE III
SD FOR TWO REAL DATASETS, DIFFERENT INTRAOPERATIVE SETUP,
DIFFERENT MOVEMENT

SD	uncorr.	WSA	CNN
dataset 1	7541.724	1285.724	1516.237
dataset 2	1951.909	927.683	1355.013

movements overlay with other effects and predictably, WSA SD values are much higher than for simulated data. This is not the case for the CNN based approach: Even though SD values of our CNN shift approach are still higher than for the WSA-approach, a quite similar ratio of SD values can be achieved for data set 1. Results for data set 2 indicate that for larger cortex silhouettes, the initialization described in Sec. II-B2 should be improved.

IV. CONCLUSION

Motion artifacts degrade signal-to-noise ratios and hide valuable diagnostic information about perfusion and neural activity. In order to decrease time delay required for analyzing the data, we propose a CNN-based motion correction algorithm. It is compared to a much more complex posterior analysis of frequency subspaces. First results indicate that while results obtained for artificial data sets show the superiority of the complex analysis, a similar performance of both methods is obtained for real data sets. Further investigations will address movements caused by breathing and pulse as well as a real-time analysis of patterns caused by different pathologies.

REFERENCES

[1] B. Lahiri, S. Bagavathiappan, T. Jayakumar, and J. Philip, "Medical applications of infrared thermography: A review," *Infrared Physics & Technology*, vol. 55, no. 4, pp. 221 – 235, 2012.
[2] I. A. Shevelev, E. N. Tsicalov, A. M. Gorbach, K. P. Budko, and G. A. Sharaev, "Thermoimaging of the brain," *Journal of Neuroscience Methods*, vol. 46, no. 1, pp. 49 – 57, 1993.
[3] G. Steiner, S. B. Sobottka, E. Koch, G. Schackert, and M. Kirsch, "Intraoperative imaging of cortical cerebral perfusion by time-resolved thermography and multivariate data analysis," *Journal of Biomedical Optics*, vol. 16, no. 1, pp. 016 001–016 001–6, 2011.
[4] L. O. Chua and L. Yang, "Cellular Neural Networks: Theory," *IEEE Transactions on Circuits and Systems*, vol. 35, pp. 1257–1272, 1988.
[5] R. Szeliski, "Image alignment and stitching: A tutorial," Microsoft Research, Tech. Rep., 2006.
[6] N. Hoffmann and G. S. et Al, "Wavelet subspace analysis of intraoperative thermal imaging for motion filtering," *Lecture Notes in Computer Science*, p. in print, 2014.
[7] B. Schölkopf, J. C. Platt, J. C. Shawe-Taylor, A. J. Smola, and R. C. Williamson, "Estimating the support of a high-dimensional distribution," *Neural Comput.*, vol. 13, no. 7, pp. 1443–1471, Jul. 2001.
[8] D. Fleet and Y. Weiss, "Optical flow estimation," in *Handbook of Mathematical Models in Computer Vision*. Springer, 2006.
[9] R. Braunschweig, J. Müller, J. Müller, and R. Tetzlaff, "NERO mastering 300k CNN cells," in *Circuit Theory and Design (ECCTD), 2013 European Conference on*, 2013, pp. 1–4.

A.4. FRAMEWORK FOR 2D-3D IMAGE FUSION OF INFRARED THERMOGRAPHY WITH PREOPERATIVE MRI

N. Hoffmann, F. Weidner, P. Urban, T. Meyer, C. Schnabel, U. Petersohn, E. Koch, S. Gumhold, G. Steiner, and M. Kirsch. Framework for 2D-3D image fusion of infrared thermography with preoperative MRI. Biomedical Engineering / Biomedizinische Technik, 2017.

Nico Hoffmann*, Florian Weidner, Peter Urban, Tobias Meyer, Christian Schnabel,
Yordan Radev, Gabriele Schackert, Uwe Petersohn, Edmund Koch, Stefan Gumhold,
Gerald Steiner and Matthias Kirsch

Framework for 2D-3D image fusion of infrared thermography with preoperative MRI

Abstract: Multimodal medical image fusion combines information of one or more images in order to improve the diagnostic value. While previous applications mainly focus on merging images from computed tomography, magnetic resonance imaging (MRI), ultrasonic and single-photon emission computed tomography, we propose a novel approach for the registration and fusion of preoperative 3D MRI with intraoperative 2D infrared thermography. Image-guided neurosurgeries are based on neuronavigation systems, which further allow us track the position and orientation of arbitrary cameras. Hereby, we are able to relate the 2D coordinate system of the infrared camera with the 3D MRI coordinate system. The registered image data are now combined by calibration-based image fusion in order to map our intraoperative 2D thermographic images onto the respective brain surface recovered from preoperative MRI. In extensive accuracy measurements, we found that the proposed framework achieves a mean accuracy of 2.46 mm.

Keywords: image fusion; image-guided neurosurgery; infrared thermography; magnetic resonance imaging; neurosurgery.

---

*Corresponding author: Nico Hoffmann, Technische Universität Dresden, Faculty of Medicine, Anesthesiology and Intensive Care Medicine, Clinical Sensoring and Monitoring, D-01307 Dresden, Germany, E-mail: nico.hoffmann@tu-dresden.de
Florian Weidner, Christian Schnabel, Edmund Koch and Gerald Steiner: Technische Universität Dresden, Faculty of Medicine, Anesthesiology and Intensive Care Medicine, Clinical Sensoring and Monitoring, D-01307 Dresden, Germany
Peter Urban and Stefan Gumhold: Technische Universität Dresden, Faculty of Computer Science, Computer Graphics and Visualisation, D-01062 Dresden, Germany
Tobias Meyer, Yordan Radev, Gabriele Schackert and Matthias Kirsch: Technische Universität Dresden, Faculty of Medicine, Neurosurgery, D-01307 Dresden, Germany
Uwe Petersohn: Technische Universität Dresden, Faculty of Computer Science, Applied Knowledge Representation and Reasoning, D-01062 Dresden, Germany

Introduction

Infrared thermography measures the emitted infrared radiation of the exposed cerebral cortex during neurosurgical interventions. According to the Stefan-Boltzmann law, this radiation correlates with the temperature of the object. In neurosurgery, the temperature distribution of the brain's surface may help to differentiate between healthy and tumor tissue [6]. One such application was demonstrated by Steiner et al. [22] who unveiled the cortical perfusion by intraoperative infrared thermography. However, thermographic images are difficult to analyze as the infrared camera operates on a different spectrum than human visual perception. This introduces additional challenges when transferring information from infrared thermography to surgical staff. As intraoperative infrared thermography is used as a medical decision support system, it is important for non-technical personnel to interpret thermographic images as well as results originating from data analysis workflows. One approach to this challenge is to fusion the novel infrared thermography with prevailing imaging modalities.

Image fusion denotes the process of joining multiple image sources to one image. The images show the same scene, yet they may have been recorded by different modalities or contain overlapping parts or both. Image fusion requires the images to be aligned such that structures being visible in each appear at the same spatial position. This transformation is called image registration and requires establishing a coordinate transform [16] by feature matching [2, 3], optimizing a similarity measure [12, 15] or by calibration-based approaches [13]. The latter relies on external tracking systems, pre-calibrated instruments or manual measurements. An exhaustive taxonomy of image registration methods can be found in [11].

Feature-based image registration is done by extracting features in all images and solving the correspondence problem. Intensity-based features [7] rely on the detected intensities of pixels or groups of them. In contrast, shape-based features often rely on spatial relationships. Extracting features and solving the correspondence problem is a process that might introduce considerable computational

complexity. If the application requires real-time or near-real-time performance, it is necessary to use features that can be calculated and correlated very fast. Furthermore, feature extraction will only work if all images represent similar structures or processes. As thermographic images are mainly influenced by cerebral perfusion while MRI images represent anatomical structures, the identification of corresponding features is cumbersome [4, 20].

Calibration-based image registration approaches are based on offline estimation of camera parameters. These parameters can be enriched by camera tracking information to establish an efficient coordinate transformation [13]. Contrary to feature-based approaches, there is no need for solving potentially expensive correspondence problems or minimization of similarity measures. Sergeeva et al. [21] demonstrate guided intraoperative resection during neurosurgery by calibration-based image registration. The probe of an ultrasound device is tracked by a neuronavigation system. Given the calibration parameters and the tracking data, the tip of the probe and the acquired ultrasound data can then be correlated with the 3D imaging data of the neuronavigation system. The absence of feature extraction and matching makes calibration-based image registration more robust when registering multimodal images. For this reason, we employ calibration-based image registration to join intraoperative 2D thermographic images with preoperative volumetric MRI data.

After successful image registration, the images are aligned and overlayed. In the affine transformation case covered in this study, the required parameters for projecting the 2D thermographic image onto the MRI dataset's surface require a translation, rotation and a scaling operation. The position of the virtual 2D thermographic image relative to the 3D model resembles the position of the infrared camera's sensor relative to the subject. In order to fusion both datasets, a projection step is necessary. Projection finds, for each pixel of the 2D thermographic image, the corresponding voxel of the 3D MRI dataset, and fuses the thermographic information with the anatomical information seen in the 3D MRI. By assuming a pin-hole camera model, a projective mapping of every pixel to its corresponding voxel depends on depth information of the imaged 2D scene [23]. If the scene is sufficiently planar, depth information can be recovered from the camera's focal distance. Other approaches require use of stereo camera systems [20] or light field cameras [24]. Another efficient [17] approach is called texture mapping [4], which was used in [1] for the image fusion of thermographic images with 3D models. Yet, contrary to ray casting [9] or projective mappings, occluded pixels are assigned a color.

Therefore, the 3D model is enriched by interpolated information which have not been measured by the infrared camera. In this work, we use texture mapping as it is a fast approach and promises good results.

Kaczmarek et al. [10] perform image fusion in order to analyze burnt skin during cardio surgery and for thermal mammography. For this purpose, they combine information of a 3D object model acquired via 3D scanning and triangulation with 2D thermographic images from an infrared camera. Contrary to the proposed calibration-based method, their approach relies on manual selection of corresponding points in the 3D mesh and the thermographic image. Additionally, their approach relies on a fixed camera position and requires recalibration once the camera's orientation is changed. In Sanches et al. [19] also propose to improve the diagnostic usefulness of thermal imaging data by CTI and MRI.

The contribution of this study is an efficient framework for 2D-3D image registration and image fusion framework to enhance 2D thermographic images by anatomical structures of preoperative MRI recordings and vice versa. The presented method relies on performing calibration-based 2D-3D image registration of infrared thermography and MRI. By this, the calibration parameters have to be estimated only once and image registration and image fusion is primarily reduced to robust and computationally efficient coordinate transformations.

Materials and methods

Image-guided neurosurgery requires referencing the patient undergoing brain surgery with respect to his or her preoperative MRI dataset. This procedure is specific to the employed neuronavigation system. It is achieved by placing fiducial markers on the patient's head prior to acquiring the MRI dataset. Afterwards, the surgeon has to manually define or segment the position of these fiducial markers in the recorded MRI dataset. During surgery, the surgeon touches each fiducial marker by the neuronavigation system's pointing device. Hereby, a coordinate transform between the intraoperative scene and the preoperative MRI dataset is established. By attaching an instrument adapter (IA) to the infrared camera, the neuronavigation system now continuously provides us the position and orientation of the IA relative to the referenced patient.

In the discussed application domain, image registration denotes the process of estimating and using a transformation function to map 2D points from the infrared camera's coordinate system to the MRI's 3D coordinate system. This means that the spatial position and orientation of the virtual 2D thermographic image plane with respect to the surface of the MRI dataset resembles the relative position and orientation of the infrared camera to the exposed brain during neurosurgery. Subsequently, the image is projected onto the surface by texture mapping. The whole workflow is sketched in Figure 1. As affine functions are linear in homogeneous coordinates, we represent
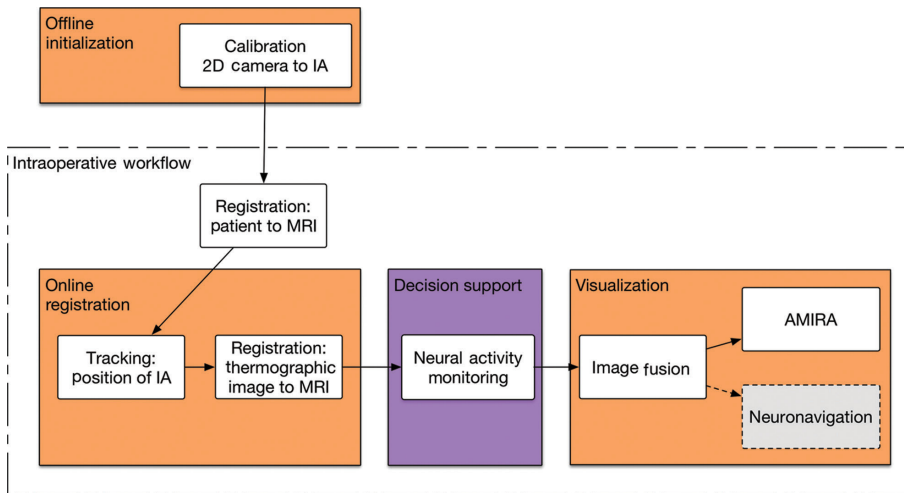
Figure 1: The parameters for image registration have to be estimated once in a calibration step.
Intraoperatively, each 2D image is then annotated by the 3D position of the 2D imaging device in the referenced 3D MRI coordinate system. This allows us to fusion the results of intraoperative data analysis workflows (purple) with preoperative MRI data. Lastly, the results are visualized using Amira.

all 3D Euclidean coordinates $p = (x, y, z)$ by 4D homogeneous coordinates $p' = (x' = \lambda x, y' = \lambda y, z' = \lambda z, \lambda)$ (see [8] for details) to simplify notation and computations. Note that p can be recovered from p' by

$$p = \left(\frac{x'}{\lambda}, \frac{y'}{\lambda}, \frac{z'}{\lambda} \right).$$

Infrared camera tracking

Neuronavigation systems provide several IAs for tracking arbitrary devices of unknown dimension. One such adapter is attached to the infrared camera and is recognized by the neuronavigation system. In order to prevent the usage of inaccurate calibration parameters, the chosen IA has to be re-calibrated at first sight in each image-guided session. This calibration is done by Brainlab's ICM4 calibration tool and an additional calibration device. The latter had to be developed to enforce a specific orientation of the IA when attached to the calibration device.

Image registration

Tracking the IA allows us to estimate the spatial position and orientation of the infrared camera's sensor array. In order to project the acquired 2D thermographic image onto the position and orientation of the camera's sensor array in the MRI coordinate system $\vec{v}' \in \mathbb{R}^4$ we have to estimate the parameters of the compound affine transformation $T: \mathbb{R}^4 \to \mathbb{R}^4$:

$$\vec{v}' = T(\vec{v}) = M_{scale} \cdot M_c \cdot M_a \cdot \vec{v} \tag{1}$$

$M_c \in \mathbb{R}^{4 \times 4}$ describes the calibration matrix while $M_a \in \mathbb{R}^{4 \times 4}$ handles additional transformations. Vector $\vec{v} \in \mathbb{R}^4$ resembles the position and direction of the IA. By ignoring M_c and M_a, the thermographic image would be centered at the position of the IA. M_{scale} corrects the virtual pixel size to the real pixel size depending on the object distance. The whole image registration process consists of three elements:

1. Tracking position adjustment
2. Thermographic image plane adjustment
3. Pixel size correction

Tracking position adjustment: The calibration matrix M_c consists of translational and rotational components $M_{TCalib} \in \mathbb{R}^{4 \times 4}$ and $M_{RCalib} \in \mathbb{R}^{4 \times 4}$, respectively:

$$M_c = M_{RCalib} \cdot M_{TCalib} \tag{2}$$

and describes the orientation adjustment of the image plane with respect to the orientation of the infrared camera (see Figure 2A). The rotational parameters compensate the directional difference between the axis of the IA and the surface normal of the infrared camera's sensor:

$$M_{RCalib} = R_x(\alpha) \cdot R_y(\beta) \cdot R_z(\gamma) \tag{3}$$

Rotation matrices $R_x \in \mathbb{R}^{4 \times 4}$, $R_y \in \mathbb{R}^{4 \times 4}$ and $R_z \in \mathbb{R}^{4 \times 4}$ realize rotations in the X, Y and Z planes given 4D homogenous coordinates. Parameter estimation is achieved by the following two steps: first, the infrared camera is oriented, such that it points vertically downwards (as sketched in Figure 2B). The orientation is validated by comparing the respective dimension of all three non-coplanar point pairs P_1, P_2 and P_3 (see Figure 2B). Physically, these points are represented by fiducial markers attached to the infrared camera. Once the camera is oriented correctly, the two points of pairs P_1, P_2 and P_3 yield the same y, z or x coordinate, respectively. Second, a configuration of rotational parameters ($\alpha \in \mathbb{R}$, $\beta \in \mathbb{R}$ and $\gamma \in \mathbb{R}$) is estimated manually, such that the normal vector of the infrared camera's image plane points in the same direction as the physical device (downwards). We chose to realize this process by a graphical user interface that provides feedback about the actual orientation of P_1, P_2 and P_3 as well as the orientation of the normal vector and allows altering rotational parameters.

The required translation parameters are estimated using spatially referenced MRI data of an imaging phantom which is imaged by the infrared camera (see Figures 3 and 4). The parameters (t_1, t_2 and t_3)(are determined manually such that the distance between

A

B
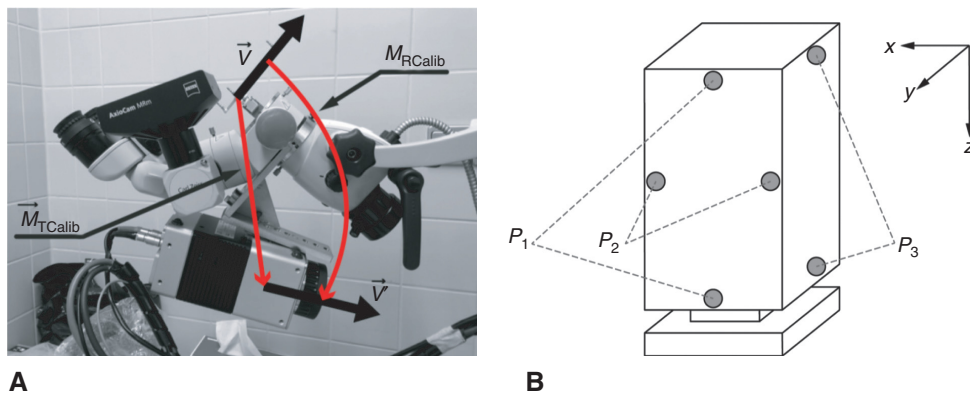
Figure 2: The tracked position of the attached instrument adapter is projected onto the position of the camera's sensor.
The required operations (translation M_{TCalib}, rotation M_{RCalib}) to project the instrument adapter's position $\vec{v}$ onto the infrared camera's sensor position $\vec{v}'$ is shown (A). Image (B) visualizes the required point pairs P_1, P_2 and P_3, and for estimating rotational parameters for tracking position adjustment (refer to "Tracking position adjustment").
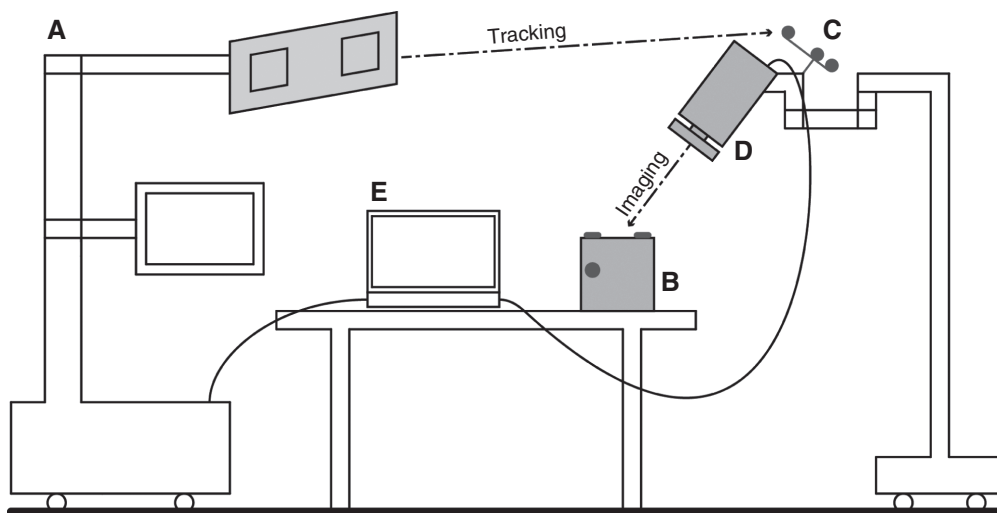
Figure 3: Setup for 3D-2D image fusion.
(A) Neuronavigation system. (B) Imaging phantom with fiducial markers. (C) Instrument adapter. (D) Infrared camera. (E) Laptop running Amira to process tracking and image data.

A

B
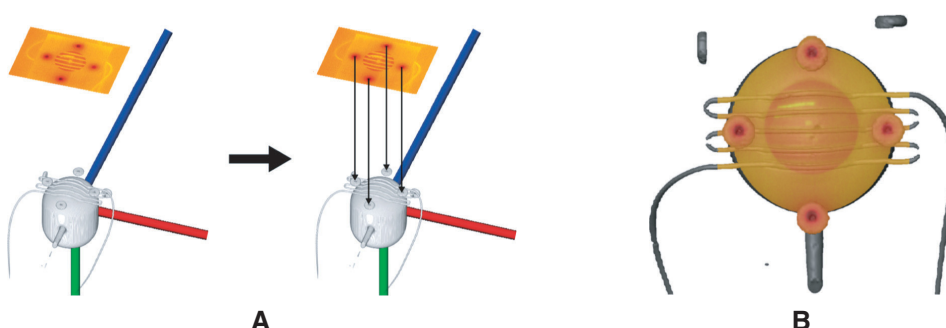
Figure 4: Thermographic images are joined with volumetric MRI data by parallel projection.
Texture mapping allows us to directly fusion the thermographic image onto the spatial referenced imaging phantom (A). Gray voxels of (B) originate from an MRI dataset of the imaging phantom, while yellow-to-red colored pixels encode its surface temperature distribution that had been detected by the infrared camera.

the spatial positions of the imaging phantom in the MRI coordinate system with its imaged surface in the 2D thermographic image is minimized.

$$M_{\text{TCalib}} = \begin{pmatrix} 1 & 0 & 0 & t_1 \\ 0 & 1 & 0 & t_2 \\ 0 & 0 & 1 & t_3 \\ 0 & 0 & 0 & 1 \end{pmatrix} \tag{4}$$

Thermographic image plane adjustment: The framework uses two additional transformations to ease handling of the 2D thermographic image, which are collapsed into $M_a \in \mathbb{R}^{4\times4}$. $M_{\text{TranslateCenter}} \in \mathbb{R}^{4\times4}$ translates the virtual origin of the image from the corner to its center. After this translation, the center of scaling and rotation is at the center of the image. Second, the image is rotated by 180° around the global x- and y-axes by rotation matrix $R_{XY180} \in \mathbb{R}^{4\times4}$ as the infrared camera provides us a mirrored image.

$$M_a = R_{XY180} \cdot M_{\text{TranslateCenter}} \tag{5}$$

Pixel size correction: Image fusion using orthogonal projection requires us to rescale the virtual 2D image such that the pixel resolution of the MRI dataset and thermographic images match. This process depends on estimating the object distance between the infrared camera and the imaged cortical surface. The correlation between the focal point $p_F \in \mathbb{R}$ and object distance $f(p_F):\mathbb{R} \to \mathbb{R}$ is modeled by

$$f(p_F) = \text{HH} + (\text{FAC}/p_f - \text{INF}) \tag{6}$$

$\text{INF} \in \mathbb{R}$ represents the maximum observable distance, $\text{HH} \in \mathbb{R}$ approximates the lens' front principal point and $\text{FAC} \in \mathbb{R}$ denotes a scaling factor. By creating a training set of focus-point-to-object distance pairs, the parameters {HH, FAC, INF} can be estimated by least-squares.

As we know the horizontal and vertical fields of view of the infrared camera's lens $\text{FOV}_h \in \mathbb{R}$, $\text{FOV}_v \in \mathbb{R}$, we are able to calculate the actual vertical $d_v \in \mathbb{R}$ and horizontal image size $d_h \in \mathbb{R}$ at an arbitrary focus value $F \in \mathbb{R}$

$$d_h = 2 * \sin(\text{FOV}_h) * f(F) \tag{7}$$

$$d_v = 2 * \sin(\text{FOV}_v) * f(F) \tag{8}$$

Both estimates contribute to the image scaling matrix $M_{\text{scale}} \in \mathbb{R}^{4\times4}$:

$$M_{\text{Scale}} = \begin{pmatrix} \dfrac{d_h}{640} & 0 & 0 & 0 \\ 0 & \dfrac{d_v}{480} & 0 & 0 \\ 0 & 0 & 1 & 0 \\ 0 & 0 & 0 & 1 \end{pmatrix} \tag{9}$$

This matrix allows us to scale the image's width and height to appropriate size. The constants 640 and 480 originate from the infrared camera's focal plane array detector size of 640×480 elements (pixels). This transformation, therefore, restores true image dimensions and enables subsequent image fusion.

Image fusion

At this point, the image is transformed such that it is located on the infrared camera's sensor array, with its size corresponding to the
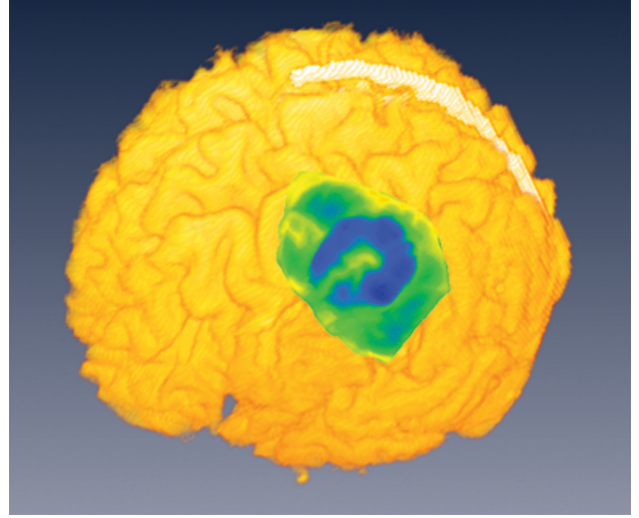
Figure 5: The proposed framework allows the combination of intraoperative thermographic images with the extracted isosurface of the human brain.
The thermographic image was acquired during the resection of a hypotherm renal cell carcinoma metastasis (blue color).

extent of the infrared camera frustum at the focal plane. The final task depicts the projection of the 2D thermographic image onto the surface of the 3D MRI dataset. Hereby, spatial information of the 3D MRI dataset is merged with temperature information extracted from the thermographic image. In the discussed neurosurgical application, an isosurface of the cerebral cortex has to be computed from preoperative MRI data. Brain segmentation algorithms (see [3]) fulfill this task by removing voxels not representing brain tissue. After successful brain segmentation, an isosurface of the cerebral cortex can be computed. As the registered 2D thermographic image is at the correct spatial position, orientation and scale, we are now able to map it onto this isosurface. As discussed, we realize this projection by texture mapping. Hereby, a 2D image patch is projected onto the 3D surface by mapping the image to surface coordinates. In our case, an orthogonal projection can be used to project the registered 2D thermographic image coordinates along the image normal vector onto the isosurface [1] (see Figure 5).

Results

The validation MRI dataset was acquired by a Siemens Magnetom Verio MRI scanner imaging a novel phantom [26] (see Figure 4). The phantom consists of three parts of plastics, an inner balloon, a tube set-up and two syringes as well as necessary connectors. The casing of the phantom simulates the head of a patient. The lid with a circular hole simulates a trepanation. Fiducial markers are attached to three sides of the imaging phantom. Thermographic images were recorded with an InfraTec VarioCAM HD head 680 S infrared camera. We further

employed the neuronavigation system BrainLab Vector-Vision 2.1.1 cranial, BrainLab iPlanNet 3.0 and respective IAs. Image registration and image fusion was done in Amira 5.5 [5].

MRI

The 3D MRI dataset of the imaging phantom has a resolution of $160 \times 512 \times 512$ voxels. The used Siemens Magnetom Verio 3T MRI scanner (Siemens Healthcare GmbH, Erlangen, Germany) achieves a voxel resolution of $1 \text{ mm} \times 0.48828 \text{ mm} \times 0.48828 \text{ mm}$. Therefore, quantization errors during image acquisition lead to a maximum error of twice the resolution. This error also defines a lower bound on the maximum achievable accuracy of the whole image registration and fusion framework as fine-grained structures are smoothed due to the loss of spatial information during MRI data acquisition. State-of-the-art 11.7 T MRI scanners [25] achieve spatial resolutions up to 0.1 mm and could, therefore, significantly minimize this error term.

Tracking beam accuracy

In this test, the imaging phantom was registered three times by Brainlab's data registration procedure. This procedure consists of two steps. First, the location of the fiducial markers had to be defined in VectorVision iPlanNet 3.0. Second, these markers were touched by BrainLab's pre-calibrated pointing device. Now, the distance between the position of the pointer tip at the fiducial markers and the respective positions in the 3D MRI dataset were computed (see Figure 2A). For this purpose, the center of each fiducial marker was touched by the pointing device three times in order to quantify the axial error of the coordinates of the pointer tip to the real position in the MRI dataset (see Table 1). We identified two main factors contributing to the tracking beam accuracy. First, the definition of the fiducial marker's virtual position in VectorVision iPlan-Net: this step is typically done manually by the medical personnel and requires great care, in order to ensure that

the defined center of the fiducial marker is exactly at its MRI counterpart.

Secondly, we found a maximum axial error of 0.99 mm in the z-direction which is triple the error in the x- and y-directions. As the z-direction of the coordinate system was nearly parallel to the viewing direction of BrainLab VectorVision2's tracking camera, we conclude that recovering depth information is less accurate. Therefore, the tracking camera should be oriented so that its viewing direction is not parallel to any dimension of the fiducial markers.

IA

To track the spatial position and orientation of the infra-red camera, it is necessary to attach an IA to the camera. The employed IA has to be calibrated in every image-guided session in order to prevent the usage of incorrectly calibrated devices. Brainlab VectorVision Cranial 2.1.1 provides information about the angular and axial error resulting from calibrating the IA. This procedure was performed 10 times and the respective results are shown in Table 2. An average angular error of 0.2° influences the image fusion process. The orientation of the IA affects the determination of the calibration parameters and, therefore, decreases the accuracy of the image registration process.

Following this calibration step, the IA was attached to a pre-existing mounting of the infrared camera (see Figure 6). The camera was kept at a fixed position while the orientation of the IA was evaluated for 10 mountings. While repeatedly mounting the IA, we found a standard deviation of 0.5° of the IA's orientation. This translates to a variable axial offset depending on the distance between the IA and the subject.

Object distance estimation

The focus value of the IR camera has to be set manually by medical personnel and is used for object distance estimation. Due to periodically occurring non-uniformity

Table 1: Factors independent of the imaged object also contribute to the overall accuracy of the presented data.

	X (mm)	Y (mm)	Z (mm)
MRI maximum error	2	0.97656	0.97656
Tracking beam accuracy	0.37 ± 0.31	0.43 ± 0.31	0.99 ± 0.79

Table 2: Calibrating the instrument adapter and mounting it to the infrared camera introduces inaccuracies to the image registration process due to manufacturing inaccuracies.

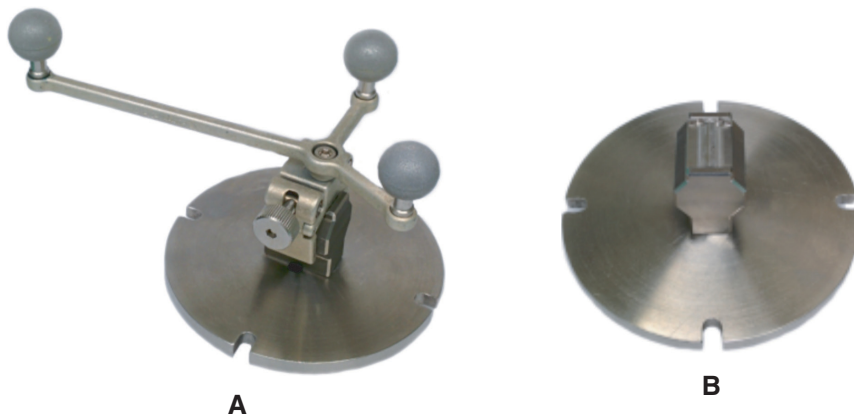|	Angle (°)	Tip (mm)
Calibration	0.2 ± 0.1	0.1 ± 0.1
IA mounting	96 ± 0.5	479.4 ± 0.4

Figure 6: Manufacturing tolerances affect the overall accuracy.
Image (A) shows the mounted instrument adapter, while the actual mounting can be seen in (B). Due to manufacturing tolerances, the instrument adapter can be tilted slightly to the left and the right, decreasing the overall accuracy. This issue can be circumvented by using specialized instrument adapters and mountings that weren't available for this study.

correction of the infrared camera, the focus value deviates even for a fixed object distance. In order to quantify this effect, the camera was placed at a typical intraoperative object distance of 30 cm and was manually focused for 10 times. The digital focus value was 6573 ± 112. This results in an estimated object distance between 27.84 and 29.16 cm causing image size variations ranging from $14.36 \text{ mm} \times 10.91 \text{ mm}$ to $15.05 \text{ mm} \times 11.43 \text{ mm}$. This gives a horizontal inaccuracy of 0.69 mm and a vertical inaccuracy of 0.52 mm.

Discussion

Calibration-based image registration requires a fixed alignment of our 2D camera and the IA. Furthermore, tracking information have to be provided by a neuronavigation system. Both requirements are commonly fulfilled in image-guided surgery. The whole framework was implemented as a C++ plugin for the visualization software Amira 5.5 [5]. Limitations of Amira forced us to approximate the physically accurate pinhole camera model by an orthogonal projection for image fusion. The missing perspective distortion is compensated by the previously discussed scaling operation M_{scale}. The proposed procedure works well under the assumption that the mapped surface is close to the focal plane. The actual projection is realized by texture mapping, meaning that the 2D thermographic image could be efficiently projected on any surface. The main drawback of texture mapping is that covert objects also get texturized by interpolated information. Yet, as we are imaging the approximately convex surface of the human brain, this drawback can be neglected.

We found that the calibration and the attachment of the IA to the imaging device is the most critical factor for the overall accuracy. To quantify this observation, the IA was placed at two extreme positions, denoted by $-\varphi$ and $+\varphi$. $+\varphi$ refers to the extreme position, where the adapter is tilted to the right, whilst $-\varphi$ represents the opposite direction. This kind of attachment is possible as the mechanism to attach the IA to the mounting has a minimal manufacturing tolerance. In the worst case, this effect degrades the overall accuracy to 10.06 mm (see Table 3).

Further, the calibration strongly depends on the quality of the tracking data. Inaccurate spatial referencing of the patient or target as well as inaccurately defined fiducial marker positions degrade the overall accuracy. For best accuracy, it is necessary to refine calibration parameters of the image registration transform each time the IA is recalibrated to the neuronavigation system and re-mounted to the camera. Otherwise, the average error increases to 9 mm. By using pre-calibrated IAs and special mountings, an accuracy of 2.46 mm is achievable without refinement of calibration parameters.

Finally, we determined the overall error at varying orientations of the IR camera with optimal mounting of the IA. The camera was rotated such that it points orthogonal,

Table 3: Manufacturing inaccuracies of the instrument adapter's mounting significantly contribute to the overall error.

	$-\varphi$ error (mm)	$+\varphi$ error (mm)
Overall maximum error	7.94 ± 0.52	10.06 ± 0.68

These inaccuracies allow slight variations of the instrument adapter's position to the right $-\varphi$ and left $+\varphi$.

Table 4: The incidence angle of the infrared camera with respect to the imaged surface as well as the object distance influence overall performance.

Orientation			Object distance
	48.48 cm error (mm)	29.30 cm error (mm)	15.02 cm error (mm)
0°	0.62±0.16	0.52±0.26	0.64±0.08
30°	2.70±0.82	2.90±1.27	3.07±0.76
60°	3.58±0.90	3.80±0.50	4.30±1.54

Increased incidence angles also degrade the amount of detected thermal radiation; thus, orthogonal orientation of the infrared camera (0°) with respect to the imaged object is to be preferred.

Table 5: The mean error of 0.59 mm increases with increasing incidence angle caused by inaccurate calibration parameters (optimized for orthogonal orientations) as well as by texture mapping.

Camera orientation	0°	30°	60°	Average
Overall mean error (mm)	0.59	2.89	3.89	2.46

30° and 60° to the imaged object. The distance of the fiducial markers visible in the fusioned thermographic image plane to the respective position in the 3D MRI dataset was computed. The results at various orientations of the IR camera indicate a cumulative error of 2.46 mm (approximately 2.5–5 voxels) including all preceding influential factors (see Tables 4 and 5), while the accuracy is maximized if the camera points orthogonally to the imaged scene. An orthogonal orientation of the infrared camera also depicts a common intraoperative configuration as the signal-to-noise ratio of infrared cameras strongly depends on the angle of incidence of the measured infrared radiation. In this case, no perspective distortions are prevalent as well.

The whole framework is optimized for computational efficiency in order to enable the application in time-critical settings. It further allows subsequent data analysis methods to incorporate anatomical and functional information from preoperative MRI measurements (for example, tumor position or localization of eloquent areas of the cerebral cortex). Furthermore, medical personnel get a tool to validate intraoperative thermographic imaging data by their expectations from prevailing volumetric imaging.

Clinically, most of the required steps for registration and fusion can be done preoperatively. The infrared camera with attached IA has to be calibrated once in order to establish the mapping between the IA's position and orientation and the camera's sensor position and orientation. Prior to the actual surgery, the MRI dataset has to be imported into Amira followed by brain segmentation. Intraoperatively, the patient has to be referenced to the neuronavigation system. Attaching a sterile IA to the covered 2D infrared camera now enables the actual image registration and image fusion. All the required software is executed on a laptop. The communication between Amira and the neuronavigation system is handled by the developed Amira plugin via the standardized OpenIGTLink interface. This means that the software is not limited to neuronavigation systems of BrainLab and can be used with any neuronavigation system that implements OpenIGTLink. It might be favorable to either display the fusioned data on a laptop screen or to output the Amira window to the neuronavigation system by its video connector.

Summary

The proposed calibration-based image registration and image fusion framework allows the combination of intraoperative 2D imaging and preoperative 3D MRI data. In neurosurgery, joining intraoperative perfusion information with neuroanatomy provides valuable information to the surgeon. For this purpose, we propose a framework for image registration and image fusion of 3D MRI with 2D thermographic imaging data. The employed calibration-based image registration algorithm transforms the intraoperatively tracked position and orientation information of our 2D infrared camera into the 3D coordinate system originating from preoperative volumetric imaging. By application of an orthogonal projection, the 2D image is projected onto the respective surface of the 3D dataset. In order to quantify the projection accuracy and unveil further potential improvements of the framework, we applied an extensive evaluation scheme. The results indicate a mean accuracy of 2.46 mm given an appropriate setup. We further estimated an upper bound of the accuracy at 10.06 mm. Further work will focus on minimizing this upper bound in order to achieve reasonable accuracy especially when using surgical microscopes with sub-millimeter resolutions.

References

[1] Akhlou M, Verney B. Multimodal fusion system for NDT and Metrology. 12th Int Conf Quant Infrared Thermogr 2014; 7.

[2] Berkels B, Cabrilo I, Haller S, Rumpf M, Schaller K. Co-registration of intra-operative photographs and pre-operative MR images. Int J Comput Assist Radiol Surg 2014; 9: 387–400.

[3] Bichinho GL, Gariba MA, Sanches IJ, Gamba HR, Cruz FPF, Nohama P. A computer tool for the fusion and visualization of thermal and magnetic resonance images. J Digit Imaging 2009; 22: 527–534.

[4] Catmull EE. A subdivision algorithm for computer display of curved surfaces. University of Utah 1974.

[5] FEI Visualization Sciences Group. Amira 5.5 2013.

[6] Gorbach AM, Heiss JD, Kopylev L, Oldfield EH. Intraoperative infrared imaging of brain tumors. J Neurosurg 2004; 101: 960–969.

[7] Goshtasby AA. Image registration – principles, tools and methods. London: Springer-Verlag 2012.

[8] Hartley RI, Zisserman A. Multiple view geometry in computer vision. 2nd ed. Cambridge: Cambridge University Press 2004.

[9] Jenkinson M, Pechaud M, Smith S. BET2: MR-based estimation of brain, skull and scalp surfaces. 11th Annu Meeting Organ Hum Brain Mapp 2005.

[10] Kaczmarek M. Integration of thermographic data with the 3D object model. 12th Int Conf Quant InfraRed Thermogr 2014.

[11] Maintz JBA, Viergever MA. A survey of medical image registration. Med Image Anal 1998; 2: 1–36.

[12] Mani VRS, Arivazhagan S. Survey of medical image registration. J Biomed Eng Tech 2013; 1: 8–25.

[13] Markelj P, Tomaževič D, Likar B, Pernuš F. A review of 3D/2D registration methods for image-guided interventions. Med Image Anal 2012; 16: 642–661.

[14] Mitrović U, Markelj P, Likar B, Milošević Z, Pernuš F. Gradient-based 3D-2D registration of cerebral angiograms. Proc SPIE 2011; 7962.

[15] Mitrović U, Špiclin Z, Likar B, Pernuš F. 3D-2D registration of cerebral angiograms: a method and evaluation on clinical images. IEEE Trans Med Imaging 2013; 32: 1550–1563.

[16] Modersitzki J. Numerical methods for image registration. 1st ed. New York: Oxford University Press Inc., 2003.

[17] Moons T, Gool LV, Vergauwen M. 3D Reconstruction from multiple images part 1: principles. Found Trends Comp Graph Vision 2010; 4: 287–404.

[18] Oswald-Tranta B, O'Leary P. Fusion of geometric and thermographic data for automated defect detection. J Electron Imaging 2012; 21: 021108-1–021108-8.

[19] Sanches IJ, Gamba HR, De Souza MA, Neves EB, Nohama P. Fusão 3D de imagens de MRI/CT e termografia. Rev Bras Eng Biomed 2013; 29: 298–308.

[20] Saxena A, Schulte J, Ng A. Depth estimation using monocular and stereo cues. Proc 20th Int Joint Conf Artif Intell 2007; 2197–2203.

[21] Sergeeva O, Uhlemann F, Schackert G, Hergeth C, Morgenstern U, Steinmeier R. Integration of intraoperative 3D-ultrasound in a commercial navigation system. Zentralbl Neurochir 2006; 67: 197–203.

[22] Steiner G, Sobottka SB, Koch E, Schackert G, Kirsch M. Intraoperative imaging of cortical cerebral perfusion by time-resolved thermography and multivariate data analysis. J Biomed Opt 2011; 16: 016001.

[23] Tan S, Dale J, Anderson A, Johnston A. Inverse perspective mapping and optic flow: A calibration method and a quantitative analysis. Image Vision Comp 2006; 24: 153–163.

[24] Tao MW, Hadap S, Malik J, Ramamoorthi R. Depth from combining defocus and correspondence using light-field cameras. Proc 2013 IEEE Int Conf Comp Vision 2013; 673–680.

[25] Vedrine P, Gilgrass G, Aubert G, et al. Iseult/INUMAC whole body 11.7 T MRI magnet. IEEE Trans. Appl. Superconductivity 2015; 25.

[26] Weidner F, Hoffmann N, Radev Y, et al. Entwicklung eines Gehirn-Phantoms zur Perfusions- und Brain Shift Simulation. Reports on Biomed. Eng. – Band 2: 5. Dresdner Medizintechnik-Symposium. 2014; 111–113.

A.5. GAUSSIAN MIXTURE MODELS FOR CLASSIFICATION OF PERFUSED BLOOD VESSELS IN INTRAOPERATIVE THERMOGRAPHY

N. Hoffmann, Y. Radev, J. Hollmach, C. Schnabel, M. Kirsch, G. Schackert, U. Petersohn, E. Koch, G. Steiner. Gaussian mixture models for classification of perfused blood vessels in intraoperative thermography. Biomedical Engineering / Biomedizinische Technik. 59(S1):596 - 599, 2014.

Gaussian mixture models for classification of perfused blood vessels in intraoperative thermography

N. Hoffmann[1], Y. Radev[2], J. Hollmach[1], C. Schnabel[1], M. Kirsch[2], G. Schackert[2], U. Petersohn[3], E. Koch[1], G. Steiner[1]

[1]Technische Universität Dresden, Klinisches Sensoring und Monitoring, Dresden, Germany, nico.hoffmann@tu-dresden.de
[2]Technische Universität Dresden, Klinik und Poliklinik für Neurochirurgie, Dresden, Germany
[3]Technische Universität Dresden, Angewandte Wissenverarbeitung, Dresden, Germany

Structure: **1. Introduction / 2. Vessel classification / 3. Results / 4. Conclusion**

Abstract

Thermography allows real-time and high-frequency capturing of small temperature variations of the exposed cortex during neurosurgical operations. One cause of temperature gradients depicts the cerebral blood flow, which leads to cyclic temperature variations. We now propose a unsupervised method to identify perfused blood vessels from thermographic image sequences by their characteristic pattern. For this purpose we employ the discrete wavelet transform on thermographic sequences and analyze its wavelet coefficients by a Gaussian mixture model. This allows the classification of cortical vessels for the analysis of cortical blood flow and correlation with white light imaging. The proposed approach is further on independent of haemodynamic parameters, resulting in a fast and robust scheme for intra-operative use.

1 Introduction

Thermal imaging is a contactless, marker-free, white light independent and non-invasive method for online measurement of temperature variations up to $30mK$. Current generation devices use infrared microbolometer focal plane arrays (FPA) sensing temperature variations at spatial resolutions of $250\mu m$ at 50 frames per second. These FPAs detect the electromagnetic radiation in the long-wavelength infrared range ($7.5 - 14\mu m$ wavelength). A black body with a temperature above $0K$ emits electromagnetic radiation in the long infrared spectral range. The power of this radiation depends on the temperature (Stefan-Boltzmann law) and in case of non-black body objects on its emissivity. The infrared radiation is then computed into temperature values and stored into a three-dimensional data cube. This data cube contains the spatial and time-resolved temperature distribution of the recorded scene.

The registered temperature variations are caused not only physiologically but also by extrinsic and environmental effects. In medical application, physiological causes are assumed to support the diagnosis of pathologies, like fever, breast cancer and vascular disorders [1]. In brainsurgery the causes of temperature variations can be divided into perfusion- and neuronal activity related heat transfers. Thus, thermography has been employed for the detection of functional areas and brain tumors [2],[3]. Because of its time resolution, thermography allows inference of diagnostic information like triggers of focal epilepsies or to distinguish functional from pathological tissue. In a previous work, we have shown that there's a direct link between temperature gradients and an injected cold bolus (ice-cold saline solution), which was used to quantify the cerebral blood flow [4]. This method enables the analysis of the cortical perfusion under cerebral ischemia.

However, thermal images are usually characterized by low gradients and exhibit weak contrasts of morphological features (see Image 1). Also boundaries do not necessarily correspond to morphological edges as seen in visible light and show dynamic behaviour due to heat transfers in several frequency bands. During OP the surgeon usually has an augmented microscopic view to the cerebral cortex enabling the matching of white light images with for example fluorescence microscopy. In this work, we demonstrate a method to extract vessels from thermographic recordings, by exploiting blood flow specific artifacts. This approach depicts the first step towards the unsupervised multimodal image fusion of white light or microscopic to thermal images. It is further possible to monitor the perfusion state of vessels without any contrast agent.

2 Vessel classification

This section at first focuses on the temperature variations of a single pixel and how to exploit its characteristics. Afterwards we develop a mechanism to automatically identify vessels in thermographic image sequences. Each pixel's timeseries of temperature values typically inhibit a non-stationarity nature while it is influenced by time varying frequencies with differing amplitude and period. Therefore we employ the wavelet transform making the multiscale analysis of signals with non-constant frequency components tractable. Hereby we are able to detect dynamic frequency components at specific points in time.

2.1 Discrete wavelet transform

The one-dimensional wavelet transform decomposes a given signal x into a space spanned by the signal convolved with some chosen base vectors (wavelet) ψ. The wavelet's shape and scale mainly determine its time-frequency resolution. Small scales result in coarse frequency localization capabilities but good time localization. [5]
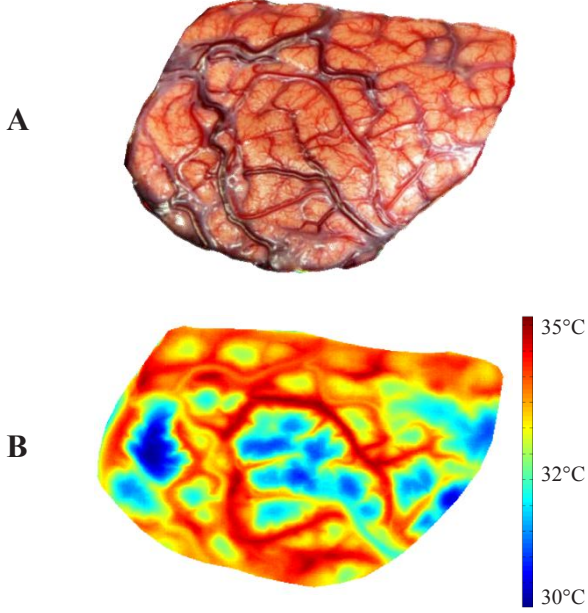

Image 1 Intraoperative recording of the exposed cortex. A shows a white-light image taken during surgery and B depicts the thermographic image of the same scene.

The discrete wavelet transform (DWT) of a discrete-time signal $x[t] \in R^n$ depicts a computationally efficient method for expanding x as wavelet series composed of weighted time localized wavelet functions. [6] describes this transform as decomposition of a $x[t]$ with $n = 2^{J+1}$ onto $J+1$ scales $j = 0,..,J$ and $k \in Z$ sampling points, as of

$$x[n] = \sum_{j=1}^{\infty}(\sum_k c_{j,k}h_j[n-2^jk] + \sum_k b_{j,k}g_j[n-2^jk]) \qquad (1)$$

$$c_{j,k} = \sum_n x[n]h^*[n-2^jk] \qquad (2)$$

with $c_{j,k}$ being detail wavelet coefficients and $b_{j,k}$ being approximation wavelet coefficients with corresponding "synthesis wavelet" $h_j[.]$ and "scaling sequences" $g_j[.]$. The fast discrete wavelet transform algorithm is a fast implementation of the DWT that applies the transformation by successive decimation and convolution operations. The frequency filter characteristics are mainly determined by the chosen discrete wavelet. The transform results in a

multi-scale analysis of $x[n]$, wherein each scale j spans a subspace V_j with [5]

$$L^2(R) \supset V_J \supset V_{J-1}... \supset V_0... \supset 0 \qquad (3)$$

Each subspace contains information about frequency components at half nyquist frequency of the superordinate subspace. This allows the time localized characterization of dynamic events. [6]

2.2 Modeling wavelet coefficients

The wavelet transform depicts a multi-resolution analysis of a signal. At scale (frequency band) j there are $K = 2^j < n$ time localized wavelet coefficients to be evaluated. In comparison the fourier transform characterizes each frequency by one single coefficient, hereby hampering inference about dynamic signals.

Since wavelet coefficients at scale $1 \leq j \leq J$ originate from decimating $x[n]$, we have to adjust the heart rate with respect to scale j

$$f_{HR}^j = f_{HR} \cdot fs/(J-j+2) \qquad (4)$$

with sampling rate fs and heart rate f_{HR}. Using equation (4) we can describe the squared wavelet coefficient of scale j at time k as

$$w_{j,k}^2 = sin^2(2\pi k/f_{HR}^j) \qquad (5)$$
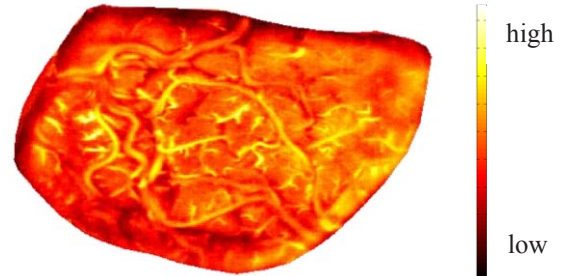
Image 2 Sum of squared wavelet coefficients at j_{HR}. Pixels with high values exhibit high activity in the heart rate frequency band. The strongest activity reveals a structure that resembles the vessels of Image 1.

2.3 Cluster analysis of wavelet coefficients

Using the described model we now propose a Gaussian mixture model for classification of pixels with cyclic patterns. Gaussian mixture models (GMM) depict a well understood approach and provide a good compromise between fast computations and model capabilities. The general definition of a GMM is given as follows:

$$p(w_j|\theta) = \sum_i \pi_i p_i(w_j|\theta_t) \qquad (6)$$

with $w_j \in R^K$ describing all wavelet coefficients at scale j, $\theta = \{\theta_i \mid i \geq 1\}$ with $\theta_i = (\mu_i, \Sigma_i, \pi_i)$ consisting of

mean vectors $\mu_i \in R^K$, covariances $\Sigma_i \in R^{K \times K}$ and component weights π_i. As we expect only heart rate artifacts and background activity at scale j we model two components. Component 1 depicts the heart rate pattern with mean $\mu_1 = \sin^2(2\pi \tilde{f}_{HR}^j)$ of equation (5) and covariance matrix $\Sigma_1 = \sigma_1 \cdot I_K$. The background component has mean $\mu_2 = \vec{0}$ and covariance matrix $\Sigma_2 = \sigma_2 I_k$. By omitting the squares, equation (5) also allows the introduction of specific phase parameters, allowing further differentiation between cortical arteries and veins.

The model is fitted to the data using the expectation maximization (EM) algorithm [7]. The EM algorithm is a well developed method for parameter estimation of models with unobservable variables Z. It estimates the parameter vector θ and hereby the segmentation Z by iteratively maximizing the data likelihood with respect to θ and Z. Derivations in the case of gaussian mixture models are described elsewhere [8].

3 Results

The method has been tested on a set of intra-operative recordings, which originated from patients with brain tumors. The thermal camera was mounted on the operation table, what only allows the application of uncooled thermal cameras that unlikely induce a temperature drift into the data. The temporal drift is compensated by modeling this low-frequent time behavior by a smooth penalized spline with polynomial basis functions.

Since equation (5) depends on the heart rate $\tilde{f}_{HR}$, we have to estimate it. Let $F(f)_+$ denote the maximum fourier coefficient of frequency f computed at m pixels as of

$$F(f)_+ = \max\{F(f)_1; F(f)_2; ....; F(f)_m\} \qquad (7)$$

then the heart rate can be recovered by solving

$$\tilde{f}_{HR} = \underset{f \in [0.5; 2]}{\arg\max} \{F(f)_+\} \qquad (8)$$

The origin and progression of cerebral heat transfers are not well understood as there is no deterministic model about future temperature gradients. The heat transfers typically induce spatially and temporally varying components below 0.1 Hz. Another component of thermographic timeseries depict heart rate and respiratory activity related artifacts. During OP, the heart rate can vary by up to 10 beats per minute depending on the pathology whereas the respiration rate is quasi-constant.

Perfused cortical vessels located in the subarachnoid space move on a pixel to subpixel level at pulse rate inducing specific temperature variations in the respective time series which allow the determination of the affected pixels. In image 3, the segmentation result of detected heart rate pattern is shown is shown in red. The structured elements turn out to match vessels as seen in the white light image. The detected vessels are a subset of the visible vessels. This is
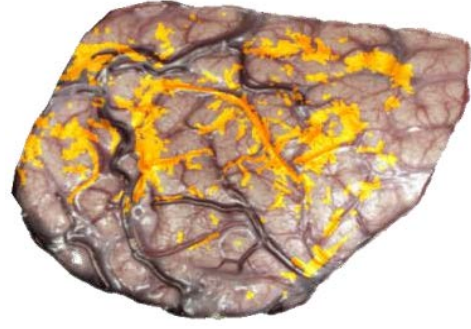
Image 3 Montage of the segmented vessels overlain to a white light recording of the exposed cortex

caused by the fact, that smaller vessels are located ontop of the cortex and thus motion below the spatial resolution or temperature gradients below camera sensitivity might occur. We further expect the periodic pattern to occur dominantly at pixels of cortical arteries, whereas veins are less affected.

Yet the method reveals vessel structures making following multimodal image fusion possible. Comparing to white-light imaging, further quantification and evaluation of the cerebral blood flow gets possible without injecting any fluid just by passively recording the cortical temperature variations. In case of aneurysm or cerebral ischemias this knowledge could be used to infer information about the pre- and post treatment perfusion state of vessels.

4 Conclusion

The temperature of blood vessels exhibits a characteristic pattern of cyclic temperature variations caused by cerebral blood flow. For analysis, the wavelet transform is applied to account for non-stationary frequencies. The subsequent classification of the cyclic pattern is done by a computationally efficient 2-Gaussian mixture model. This model is fitted to the data by the expectation maximization algorithm. The classification result depicts a map of blood vessels located in the subarachnoid space. The approach provides a fast and scalable solution to the identification of vessels in temperature time series without the need to pre-specify any haemodynamic parameters.

In further studies, this map will be employed to infer the arrival time and characteristic pattern of thermal tracers (cold bolus approach as demonstrated in [4]) in order to quantify its spatio-temporal distribution. Another application depicts the image fusion of thermal images with white light and microscopic views using the determined vessel structure. In white light imaging thresholding wrt. to the vessel's color characterics yields a binary representation consisting of vessels and background. By non-linear registration methods the extracted vessels of the thermographic- and whitelight image can then be joined providing a transformation matrix allowing the unsupervised fusion of both modalities. This enables monitoring the perfusion state of blood vessels by a combination of blood flow driven ther-

mographic sequences with morphological information from white light images.

References

[1] B. Lahiri, S. Bagavathiappan, T. Jayakumar, and J. Philip, "Medical applications of infrared thermography: A review," Infrared Physics & Technology, vol. 55, no. 4, pp. 221 – 235, 2012.

[2] A. M. Gorbach, J. D. Heiss, L. Kopylev, and E. H. Oldfield, "Intraoperative infrared imaging of brain tumors," Journal of Neurosurgery, vol. 101, no. 6, pp. 960–969, 2004.

[3] I. A. Shevelev, E. N. Tsicalov, A. M. Gorbach, K. P. Budko, and G. A. Sharaev, "Thermoimaging of the brain," Journal of Neuroscience Methods, vol. 46, no. 1, pp. 49 – 57, 1993.

[4] G. Steiner, S. B. Sobottka, E. Koch, G. Schackert, and M. Kirsch, "Intraoperative imaging of cortical cerebral perfusion by time-resolved thermography and multivariate data analysis," Journal of Biomedical Optics, vol. 16, no. 1, pp. 016 001–016 001–6, 2011.

[5] S. Mallat, a wavelet tour of signal processing. Academic Press, 1998.

[6] O. Rioul and P. Duhamel, "Fast algorithms for discrete and continuous wavelet transforms," IEEE Transactions on Information Theory, vol. 38, no. 2, pp. 569–586, 1992.

[7] A. P. Dempster, N. M. Laird, and D. B. Rubin, "Maximum likelihood from incomplete data via the em algorithm," JOURNAL OF THE ROYAL STATISTICAL SOCIETY, SERIES B, vol. 39, no. 1, pp. 1–38, 1977.

[8] C. M. Bishop, Pattern Recognition and Machine Learning. Springer, 2006.

A.6. QUANTIFICATION AND CLASSIFICATION OF CORTICAL PERFUSION DURING ISCHEMIC STROKES BY INTRAOPERATIVE THERMAL IMAGING

Quantification and Classification of Cortical Perfusion during Ischemic Strokes by Intraoperative Thermal Imaging

Nico Hoffmann*, Georg Drache*, Edmund Koch†, Gerald Steiner†, Matthias Kirsch‡§¶ and Uwe Petersohn*

*Applied Knowledge Representation and Reasoning, Faculty of Computer Science,Technische Universität Dresden, Dresden, Germany

†Clinical Sensing and Monitoring, Faculty of Medicine Carl Gustav Carus, Technische Universität Dresden, Dresden, Germany

‡Neurosurgery, University Hospital Carl Gustav Carus, Technische Universität Dresden, Dresden, Germany

§CRTD/DFG-Center for Regenerative Therapies Dresden Cluster of Excellence, Technische Universität Dresden, Dresden, Germany

¶Nationales Centrum für Tumorerkrankungen (NCT), Dresden, Germany

Abstract—**Thermal imaging is a non-invasive and marker-free approach for intraoperative measurements of small temperature variations. In this work, we demonstrate the abilities of active dynamic thermal imaging for analysis of tissue perfusion state in case of cerebral ischemia. For this purpose, a NaCl irrigation is applied to the exposed cortex during hemicraniectomy. The cortical temperature changes are measured by a thermal imaging system and the thermal signal is recognized by a novel machine learning framework. Subsequent tissue heating is then approximated by a double exponential function to estimate tissue temperature decay constants. These constants allow us to characterize tissue with respect to its dynamic thermal properties. Using a Gaussian mixture model we show the correlation of these estimated parameters with infarct demarcations of post-operative CT. This novel scheme yields a standardized representation of cortical thermodynamic properties and might guide further research regarding specific intraoperative diagnostics.**

I. Introduction

Ischemic strokes denote the shortage of substrates of delimited areas of the brain by a blockage of vessels (embolism or thrombosis). Severe strokes lead to a swelling of brain tissue, which raises the intracranial pressure (ICP) yielding a bad or fatal prognosis if not treated appropriately. Hemicraniectomy can be considered as last resort to decrease the ICP.

In brain tissue, temperature variations are primarily caused by heat transfers originating from cerebral perfusion. In fact, the local cerebral blood flow correlates with cell metabolism and can be used as marker for tissue state and neural activity. Intraoperative thermal imaging now allows the inference of diagnostic information about perfusion- and neural activity related disorders. In general, thermal imaging is a contactless, marker-free, white-light independent and non-invasive method for online measurement of temperature variations up to $30~\mu K$. Current uncooled devices use infrared microbolometer focal plane array detectors measuring a field of view of 16 x 12 cm with an underlying spatial resolution of $250~\mu m$ per pixel at a framerate of 50 Hz. The detected infrared radiation arriving at the microbolometer array is processed and stored as two-dimensional image.

In the past, Gorbach et al. provided a method to distinguished tumor tissue from normal tissue based on thermal imaging[1]. Additionally, Steiner et al. visualized the cortical blood flow by analyzing the spatial distribution of a cold bolus applied through a central line with multivariate analysis tools[2].

In this work, we propose an alternative approach to the cold bolus method of Steiner et al. in order to characterize the perfusion state of cortical tissue. In general, we describe a machine learning framework to recognize cortical irrigations. Furthermore, a mathematical model is designed such that it allows us to quantify the time-dependent thermal behavior during the treatment of ischemic strokes. The proposed method allows the selective analysis of cortical tissue and integrates seamlessly into current intraoperative workflows. In contrast to the cold bolus approach, our method is not limited to perfused areas and provides us to control the signal-to-noise ratio of our target pattern. Finally, we extend prior findings of Gorbach et al.[3] by a straightforward intraoperative approach with a sound mathematical approximation of the time-dependent behavior of cortical tissue.

II. Related Work

In the last years, sensor technology for uncooled thermal imaging has developed in terms of accuracy. This enables a wide range of applications for thermal imaging. Branemark et al. found that diabetes correlates with reduced body temperatures[4]. These findings were supplemented by Sun et al. who investigated the thermal behavior of human extremities under diabetes. They found a significantly elevated average temperature of the human feet which might be a marker for early diabetic neuropathy[5].

Blood pressure monitoring as discussed by Cesaris et al. is another possible application field of thermal imaging[6]. Thermography was even employed in the field of dentistry[7]. Since fever typically leads to an increased face temperature, it was shown that thermal imaging can be used to recognize SARS [8].

Active dynamic thermography depicts an approach that requires the utilization of a temperature gradient to a surface in
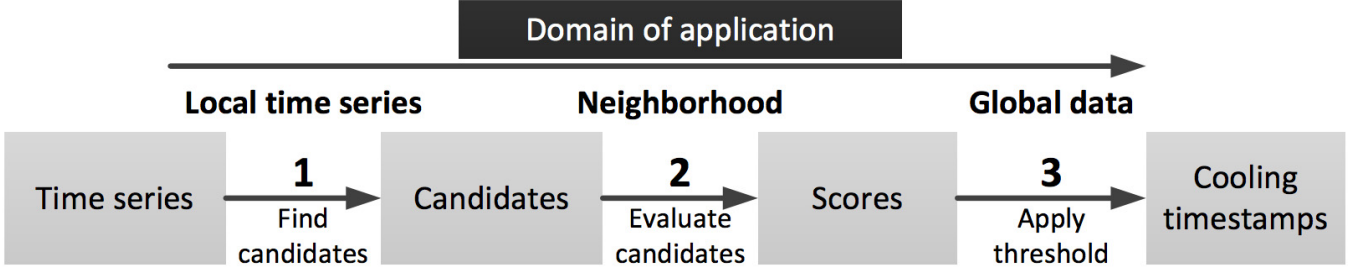
Fig. 1. Overview of the proposed irrigation detection framework.

order to inspect its structures. Since heat transfers propagate into the depth of an object, varying the amplitude of the temperature gradient allows inspecting different object layers and thereby enables some sort of thermal tomography[9]. This idea was also brought into medical domain. Deng and Liu[10] evaporated a 75% ethanol solution on tissue and found that it might be an indicator for subsurface breast cancer. Gorbach et al.[3] irrigated the exposed cerebral cortex with ice cold saline solution for two seconds. He then recorded the temperature increase and found that tumor tissue took more time to reach the equilibrium temperature compared to healthy tissue. He concluded dynamic thermal imaging might be suitable for the analysis of tissue displacement during surgery.

In this wor, we contribute an approach that integrates seamlessly into intraoperative workflows and a sound mathematical framework to get a standardized representation of tissue heating behavior. The approach doesn't require any external input of surgical personal for the detection of irrigation events and subsequent visualization of the results.

III. MATERIALS AND METHODS

Gorbach et al. proposed irrigating the surface of cortical tissue for some time to propagate heat through several tissue layers[3]. In contrast, we employ available intraoperative tools to prevent the need for additional sterile tools. The surgeon typically has a tool (e.g. syringe) to purge sterile sodium chloride (NaCl) onto tissue. Hereby, it is possible to selectively apply NaCl to a delimited area of the exposed cortex for a specific duration.

This irrigation induces a steep drop in temperature followed by a temperature increase caused by heat transfers. In human tissue, this heating correlates with thermodynamic properties of the underlying tissue, thermal conductivity and tissue perfusion state. By modeling this behavior and estimating respective parameters, it is possible to characterize the imaged tissue.

A. Approximation of Dynamic Thermal behavior

In 1948, Pennes[11] proposed the biologically inspired "Bioheat equation". He proposed the following model to describe internal as well as external influences to the heat distribution in living tissue:

$$c_p \rho \frac{\delta T(x,y,z)}{\delta t} = \kappa \nabla^2 T(x,y,z,t) + q_b + q_m + q_{ex} \quad (1)$$

with the specific heat c_p, material density ρ, the temperature distribution $T(x,y,z)$ at time t $T(x,y,z,t)$ and thermal inductivity κ. He further added biological parameters describing the heat power density of q_b blood flow, q_m metabolism and external power density q_{ex}.

Several authors have shown the discretization of Penne's equation (see for example Gutierrez et al.[12]). In our case, we are facing several a priori unknown parameters, whose estimation schemes would introduce significant computational complexity and potentially inaccurate estimates. To counter these challenges, we employ Nowakowski's approach to approximate tissue's thermal behavior by a double exponential function[13]:

$$T(t) = T_{equ} + \Delta T_1 exp(-t\lambda_1) + \Delta T_2 exp(-t\lambda_2) \quad (2)$$

In this equation, T_{equ} represents the tissue's equilibrium temperature, ΔT_1 and ΔT_2 are the scaling coefficients of both exponential functions. The decay constants λ_1 and λ_2 with unit s^{-1} represent the amplitude of the tissue's temperature change rate. This model approximates the tissue heating following the application of a cold cortical irrigation with NaCl. Hereby, we are able to quantify the cortical perfusion as it correlates with the rate of temperature change.

By application of a liquid to the exposed cortex, we expect to observe at least two different components that are well described by this double exponential function. One component represents the temperature changes of the applied cool fluid. The other component describes the temperature change of the affected underlying tissue. The latter dominates the temperature change after the fluid drained from the surface. The elevated ICP in case of cerebral ischemia results in the cortex having a convex shape with high curvature. Therefore, we expect the applied fluid to drain continuously. This means that λ_1 of the fluid is larger than the temperature rise, λ_2, of the underlying tissue yielding a reliable estimate of λ_2. However, it is essential to apply a significant temperature gradient to the cortex for accurate parameter estimation, otherwise the dynamic temperature behavior caused by the draining NaCl solution can't be differentiated from tissue heating. This would prevent any subsequent analysis based on λ_2.

Two factors affect the accuracy of the proposed method: the temperature difference between liquid and cortex and the

application time of the fluid before its drainage.

A high curvature of the cortex leads to a fast fluid drain and low irrigation impact requiring longer application times. Also, an accumulation of fluid is to be prevented since this would hamper any reliable estimate of λ_2. Note that the model applies to single time series, what allows for heterogeneous application pattern of the liquid - as long as ΔT_2 is maximized.

B. Irrigation Detector

The potential heterogeneous selective irrigation of specific parts of the exposed cortical surface requires to unveil all timepoints of irrigation events for each pixel in order to analyse its dynamic thermal behavior.

This recognition task is difficult because of the variety of irrigation patterns, the caused temperature decrease can also be very low and hard to distinguish from background noise. In order to solve these issues, we propose a framework consisting of three steps (see Fig. 1):

1) Irrigation Window Determination
2) Spatial Scoring
3) Warming Period Detection

The first step depicts a fast approximate search for possible irrigation events. Afterwards, the events are correlated with events of adjacent pixels to improve detection accuracy. In a last step, a main irrigation event is estimated for subsequent heating analysis given our double exponential model.

1) Irrigation Window Determination: An irrigation event denotes the whole time frame when a cold liquid is being applied to the exposed cortex. This irrigation event causes a rapid change in temperature followed by a slow temperature rise. Since we aim to analyze the heating behavior following an irrigation, we have to estimate a precise irrigation timestamp. In order to improve the speed of this process, we employ a hierarchical estimation scheme. First, the stream of thermal images is partitioned into overlapping windows that can be analyzed independently. In the following, we omit additional notations for the respective window as it can be achieved by partitioning timestamps t_i respectively. In order to detect the irrigations efficiently, we exploit that an irrigation event causes a steep temperature decrease and a slow increase to the tissue's equilibrium temperature. This behavior introduces a characteristic pattern into the sorted temperature series $s(p, t_i)$ (see fig. 2). Since the irrigation pattern can be recognized in the lower temperature part of the sorted time series, no additional template matching is necessary. This means that we can analyze all pixel's timeseries at once.

Let $s(p, i)$ denote the time points of the sorted temperature series of pixel $p \in \mathbb{N}^2$ with index $i \in [1, .., n]$ given n measurements. For each $s(p, i)$ there is an $t_j(p)$ with $j \in [1, .., n]$ such that $T(p, s_i(p)) = T(p, t_j(p))$. By $T(p, t_i(p))$ we denote the i-th measured temperature of pixel p at time $t_i(p)$. For reasons of comprehensibility, we omit the pixel index p when not necessary. In general, an irrigation event is recognized by

evaluating the following equation:

$$m(p) = f_{\mathrm{norm}} \times \sum_{i=i_1}^{i_{step}} |T(p, s_i(p)) - corr(i)| < t_{\mathrm{div}} \quad (3)$$

given normalization constant f_{norm}, threshold t_{div} and a correlation function $corr(\cdot)$. The index variables i_1 and i_{step} represent the heating window. Those constants are explained in the following paragraphs. The latter computes the similarity of the measured temperature to our model function by a single exponential function. This idea is similar to the shapelet approach of Ye and Keogh[14]). The correlation function is defined by

$$corr(t) = lim_{up} - (lim_{up} - lim_{bottom})exp(-\lambda(t - t_{start})) \quad (4)$$

with t_{start} being short for $s_{i_{start}}$. The parameters are approximated from the sorted timeseries by

$$lim_{up} = T(s(i_{step})) + 0.1 \quad (5)$$

$$lim_{bottom} = T(s_{i_{start}})) \quad (6)$$

$$\lambda = n^{-1} \sum_{i=1}^{n} \left\{ -n^{-1} ln \left(\frac{lim_{up} - T(s_{z_i}))}{lim_{up} - lim_{bottom}} \right) \right\} \quad (7)$$

at a certain number of supporting points n. By i_{step}, we denote the position of the step or last frame of the regarded irrigation window while i_{start} denotes the index of the first frame. The upper limit (lim_{up}) of the exponential decay function is set to the temperature $T(t_{step})$ representing the highest temperature after the irrigation event. A margin of $.1K$ is added to avoid divisions by zero. The lower limit (lim_{bottom}) corresponds to the lowest temperature in our window. A rough estimate of the decay constant λ is computed at three supporting points z_i. For each z_i, we estimate λ and solve the consensus problem by simply averaging all three estimates. This scheme yields a fast approximation of the characteristic warming behavior. We have to emphasize that this method is employed as first step to the recognition of our heating pattern, in subsequent steps we estimate the parameters of our proposed model (see section III-A) by a robust method.

2) Spatial Scoring: Irrigations typically affect multiple adjacent pixels with similar temperature gradients. In the following, we discuss an approach to account for this effect and thereby improve overall accuracy of our irrigation detector framework. Spatial scoring denotes that we use the information of adjacent irrigation events when reasoning about local irrigation events. This means that the score correlates with spatial homogeneity and similarity of irrigation events. A clear similarity leads to a high score value for all affected pixels. In general, the score σ of pixels p_s and p_t is defined by

$$\sigma(p_s, p_t) = f \times max(\Delta T_{p_s}, \Delta T_{p_t}) \quad (8)$$

with $\Delta T = \max_{i \in I} T(i) - \min_{j \in I} T(j)$ and I being the set of all indexes of the analyzed window. ΔT is therefore defined as
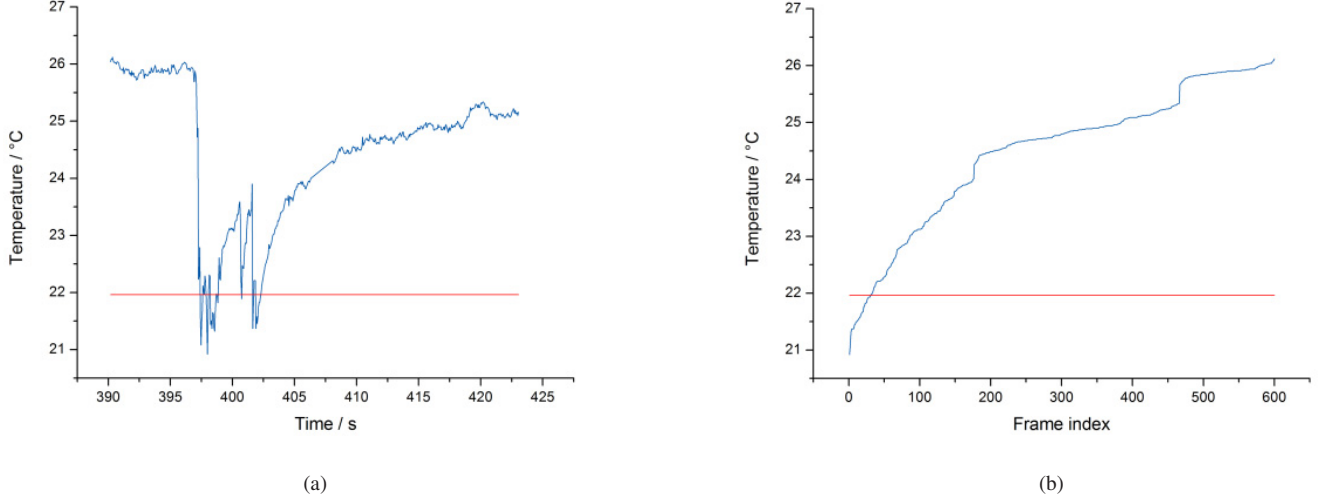
Fig. 2. **(a)** Temperature time series after application of multiple NaCl irrigations **(b)** The sorted time series shows a characteristic pattern invariant to the number of irrigations.

maximal temperature deviation. Let further be

$$f(p_s, p_t) = \begin{cases} 0, & \text{no irrigation} \\ f_m(p_s, p_t), & \text{irrigation at } p_s \text{ or } p_t \\ 2f_m(p_s, p_t), & \text{irrigation at both sites} \end{cases} \quad (9)$$

and

$$f_m(p_s, p_t) = \begin{cases} \nu_1, & \Delta t_m(p_s, p_t) < t_{m_1} \\ \nu_2, & t_{m_1} \leq \Delta t_m(p_s, p_t) < t_{m_2} \\ \nu_3, & t_{m_2} \leq \Delta t_m(p_s, p_t) < t_{m_3} \\ 0, & t_{m_3} < \Delta t_m(p_s, p_t) \end{cases} \quad (10)$$

t_{m_i} and ν_i with $i \in [0;3]$ are penalty parameters. By $\Delta t_m(p_s, p_t) = min(|ts_{p_s}(i) - ts_{p_t}(j)|)$ we denote the minimal temporal distance of the minimum temperature of two pixels p_s and p_t, whereas ts are lists of timestamps of the k lowest temperatures in the evaluated interval. The score (equation 8) represents the assumption that neighboring pixels are affected by an irrigation event at little temporal difference. In order to compute a weighted score by including the neighbors $\mathcal{N}(p)$ of pixel p, we have

$$\sigma(p_s)^{sum} = \sum_{p_t \in \mathcal{N}(p_s)} \Delta(p_s, p_t) \times \sigma(p_s, p_t) \quad (11)$$

wherein $\Delta(p_s, p_t) = 1/(ln||p_s - p_t||_2 + 1)$ is a distance metric depending on the spatial position of pixels p_s and p_t. Therefore, $\sigma(x)^{sum}$ is a weighted sum of neighboring scores. An irrigation event is flagged as detected, if the following holds

$$f^{detect} = \begin{cases} 1, & \sigma^{sum} \geq H \times t_f \\ 0, & otherwise \end{cases} \quad (12)$$

with H being the highest score reached during analysis capped to minimum level σ_{ref}: $H = min(\max_{p_s, p_t \in I}(\sigma(p_s, p_t)), \sigma_{ref})$.

3) Warming Period Detection: The preceding steps yield a list of irrigation events. For reasons of comparison, we

propose to evaluate only warming phases caused by the same irrigation event. Ideally, the liquid is applied instantaneously to the whole surface leading to very similar irrigation events. However, the propagation of temperature gradient into deeper tissue layers requires a slow, circular application of the liquid. This leads to many irrigation events originating from a global liquid application with spatially-dependent timestamps.

The time point of the global liquid application is denoted by irrigation reference and has to be recovered. Let $h(t_j)$ be the number of pixels with an irrigation event at timestamp t_j. The set $\mathbb{C}$ denotes the set of all possible irrigation timestamps. The reference timestamp t_{ref} is estimated as of

$$t_{ref} = \underset{t_j \in \mathbb{C}}{argmax} \left\{ \sum_{i=-2}^{i=2} h(t_{j+i}) \right\} \quad (13)$$

The latter equation recovers the timestamp of a reference irrigation event by evaluating the number of pixels being affected by an irrigation within 5 consecutive frames.

By fixing t_{ref}, we recover all pixels belonging to this reference irrigation. Therefore, an irrigation event at pixel i to t_{ref} is accepted if it occurred ± 5 seconds with respect to the reference timestamp. The recovered timestamp of pixel p_s is denoted by $t^*(p_s)$. Reliable model parameter estimates are achieved by evaluating the pixel's score at t^* while omitting irrigation events with weak score.

4) Parameter Learning: The proposed framework consists of several parameters for a fast and reliable detection of irrigation events. In order to improve the accuracy of our irrigation detector and adopt it to characteristics of the discussed use case, we learn relevant parameters from training data. The parameters have to be learned once and can then be used in subsequent intraoperative measurements. For parameter learning, we employ a Markov Chain Monte Carlo (MCMC)[15]

sampler that we will discuss now.

Markov Chain Monte Carlo methods draw dependent samples of a probability distribution. Each drawn sample fulfills the local Markov property meaning that it only depends on the previously drawn sample and a given probability distribution. The Metropolis-Hasting MCMC sampler is a canonical approach based on three main steps for drawing and accepting some sample θ:

1) draw θ^t from proposal distribution $p(\theta^t; \theta^{t-1})$
2) compute acceptance probability $p(\theta)$
3) accept if $p(\theta)$ is sufficiently large

The proposal distribution is modeled as normal distribution such that $p(\theta^t; \theta^{t+1}) \sim N(\theta^{t+1}, \sigma)$ given σ describing the step length. The overall energy of a configuration θ is denoted by

$$f(\theta) = \sqrt{f_{pos}^2 + f_{neg}^2} \tag{14}$$

with f_{pos} being the number of false positives and f_{neg} being the number of false negatives of the irrigation detector.

Since we only want to evaluate the latest irrigation event, i.e. the event being followed by a temperature increase until equilibrium temperature, we have to adopt the learning strategy for the multiple irrigation event detector. Suppose the warming behavior can be approximated by a double exponential function, then we arrive at the energy function of configuration θ for the multiple irrigation event detector

$$f(\theta) = \min_{\theta} \left\{ \sum_i \sum_{t=0}^{5s} |T_i(t) - \widetilde{T}_i(t)| \right\} \tag{15}$$

with $\widetilde{T}$ being the fitted double exponential function as of equation 2. By this formulation, we can quantify the divergence of expected non-linear warming behavior and the measured one after the estimated irrigation event. Note that the upper limit of $5\,s$ is an empirical constant requiring that the warming time must be at least 5 seconds.

Since the parameters of the single irrigation event detector are independent of multiple event detector's parameters, we first estimate the parameters for the single detector and afterwards for the multiple irrigation detector. The modified MH-sampler given an arbitrary configuration θ is sketched by algorithm 1.

C. Classification

As discussed, the temperature decay parameter λ_2 describes the heating behavior of underlying tissue. In case of an ischemic stroke, we further expect low values of λ_2 in under- or unperfused tissue. The parameter λ_2 should be significantly larger in healthy areas due to high perfusion and metabolism in living tissue. We also hypothesize characteristic behavior in-between healthy and ischemic tissue what we denote by "uncertain".

Therefore λ_2 is partitioned into tissue states $\mathbb{S} = \{ischemic, uncertain, healthy\}$. λ_2 is expected to vary in each state at different scales. Therefore, we model the expected

---

Algorithm 1: MH-sampler to learn parameters of the discussed irrigation detection and tissue classification framework.

input: step width σ
input: number of iterations l
input: tolerance ϵ
output: parameter vector $\theta^* \in \mathbb{R}^k$

randomly sample $\theta_1 \in \mathbb{R}^k$;
for *iteration $t \leftarrow 1$ **to** l **do***
    randomly choose dimension i of $(1; k)$;
    sample $\theta_i^{t+1} \sim N(\theta_i^t, \sigma)$;
    accept θ_i^{t+1} if $f(\theta^{t+1}) < f(\theta^t)$ or if
    $p_{acc}(\theta^{t+1}, \theta^t) = \frac{f(\theta^t)^2}{f(\theta^{t+1})^2}$ is sufficiently small.;
    if *$f(\theta^{t+1}) < \epsilon$* **then**
        stop;

---

behavior of the temperature decay constant λ_2 by the following Gaussian mixture model:

$$\lambda_2^{ischemic} \sim N(\mu_i, \sigma_i)$$
$$\lambda_2^{uncertain} \sim N(\mu_u, \sigma_u)$$
$$\lambda_2^{healthy} \sim N(\mu_h, \sigma_h)$$

Since the parameters $\Theta = (\mu_i, \mu_u, \mu_h, \sigma_i, \sigma_u, \sigma_h)$ of each class are patient specific and a priori unknown, we propose to employ the EM algorithm for parameter estimation. Its actual derivation can be found elsewhere (see for example Bishop[16]).

For each λ_2, this model yields the probabilities $p(y|\lambda_2; \Theta)$ of belonging to state $s \in \mathbb{S}$. At specific pixel location p, we are now able to infer the most probable tissue state

$$\widetilde{s}_p \in \underset{s_p \in \mathbb{S}}{argmax}\ p(s_p|\lambda_2(p); \Theta) \tag{16}$$

Each state's probability might be a reasonable indicator to infer further knowledge regarding the possible future progression of the ischemic demarcation.

D. Overview of the Irrigation detection and classification scheme

The proposed framework consists of several steps for detection of irrigation events, feature extraction and classification. Algorithm 2 shows the whole algorithm.

IV. RESULTS AND DISCUSSION

We performed several experiments to evaluate the performance of the proposed irrigation event detector. All intra-operative procedures were approved by the Human Ethics Committee of the Technische Universität Dresden (no. EK 323122008). Informed consent was obtained postoperatively in accordance with the approved scheme.

In the following, we evaluate the detector's performance in experimental test and training datasets. These are also used for learning the parameter configuration of the detectors.

Algorithm 2: Schematic overview of the proposed irrigation detection and tissue classification framework.

input: data set, $T \in \mathbb{R}^{n \times m}$
input: parameter vector, $\theta \in \mathbb{R}^l$
output: classified image, $X^* \in \mathbb{R}^n$

for *pixel* $k \leftarrow 1$ **to** n *and window* w **do**
    sort timeseries $T_{(k,w)} \rightarrow s_{(k,w)}$;
    if $m(k) = False$ **then**
        skip w;
    $f_{(k,w)}^{detect} = \sigma_{(k,w)}^{sum} > H \times t_f$;

compute histogram $h(f^{detect})$;
recover $t_{ref} = \underset{t_j \in \mathbb{C}}{argmax} \left\{ \sum_{i=-2}^{i=2} h(t_{j+i}) \right\}$;
find $p \in \mathbb{P}$ *with irrigation events* $|t_p^* - t_{ref}| \leq 5s$;
solve eqn. 2 for $t^* \leq t \leq t^* + 5s$;
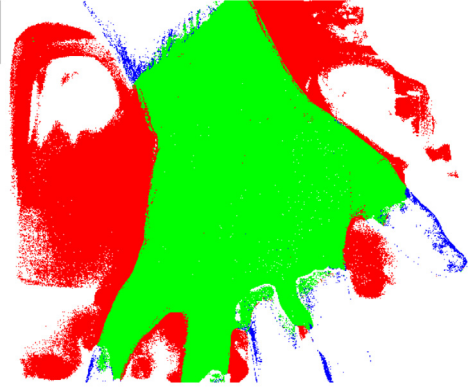*classify decay constant* $\lambda_2(p)$ *by a 3-GMM;*

Fig. 3. The detected irrigations of dataset "20, hand pour" strongly deviate from the results of other test datasets. After application of the temperature gradient to the hand, the liquid drained into a water basin beneath the hand. This behavior resembled a typical irrigation and was detected by the proposed framework. Green resembles a true positive, blue a false negative and red a false positive classification.

Afterwards, the approach is used to analyze intraoperative data.

A. Evaluation Datasets

It is fairly difficult to simulate the thermal behavior of the cortex experimentally since well-perfused exposed cortical tissue is necessary. Therefore we chose to measure the temperature propagation of the arm and hand of a volunteer as phantom. Both parts of the body also have near-surface vessels, comparable curvature, are quite homogeneously perfused but do not contain any hotspots or underperfusion. The surface temperature was approximately $28 \,^{\circ}C$. We applied several temperature gradients to the surface: $\{-8, -3, 0\}$ K whilst measuring thermal data of the surface.
We discovered two different styles of applying the irrigation liquid during intraoperative measurements: pour method and spray method. Pour implies that all of the liquid is applied to the cortex at once meaning that all the affected tissue is cooled down simultaneously. The spray method is a more flexible approach. Hereby the surgeon applies a jet of the NaCl solution to the surface in a circular manner. This can be repeated several times leading to multiple irrigation events and resulting in a very heterogeneous fluid distribution on the surface. Yet, the spray method allows a deeper propagation of temperature gradients. We simulated both behaviors during our experiments. The experimental setup consisted of a volunteer placing his hand over a glass basin. Then, water was applied to the hand in order to cause a heat transfer and subsequently drained off into the basin.

B. Irrigation Detector

The evaluation datasets were partitioned into training and test datasets. Using the MCMC sampler, the parameters t_f (see eqn. 3) and divergence threshold (see eqn. 8) were learned. The sampler achieved acceptance rates ranging from 85 % to 92 %. The results further indicate the detector achieves a good overall accuracy (see table I). We further observe a great margin in parameter space since many parameter configurations seem to perform equally well given the training and test data. The performance of $-8h - spr - r$ and $-8h - pour$ dataset deviate significantly from other results in terms of false positives (see figure 3). We found that this raised false positive rate is caused by the experimental setup. Both datasets were recorded during the first experimental run, so that the former dry and warm basin got cooled down by the fluid triggering a cooling detection. In latter runs, we filled the basin with a small amount of water to prevent this issue.

C. Tissue Characterization

Prior to the following analysis and discussion we want to emphasize that the cortical temperature distribution in case of cerebral ischemia hasn't been evaluated by thermal imaging before. Therefore we validated our model assumption regarding the differentiability of λ_1 and λ_2 empirically. As hypothesized, λ_1 is one order of magnitude larger than λ_1 because of the fast draining effect. The distribution of both parameters can be seen in figure 4.
In detail, the cohort contained cases of ischemic strokes of middle cerebral artery (MCA) respectively anterior cerebral artery (ACA) requiring a decompressive hemicraniectomy to decrease intracerebral pressure. Accompanying and without influencing the surgical intervention we performed thermographic measurements of the exposed cortex and recorded intraoperative irrigations. These irrigations are common in neurosurgery in order to prevent cortical drying.
It has to be emphasized that this intervention typically occurs in an emergency situation what prevents lengthy measurement procedures and complex experimental requirements. Therefore, we were not able to apply an irrigation liquid of appropriate temperature in some cases leading to less meaningful results.
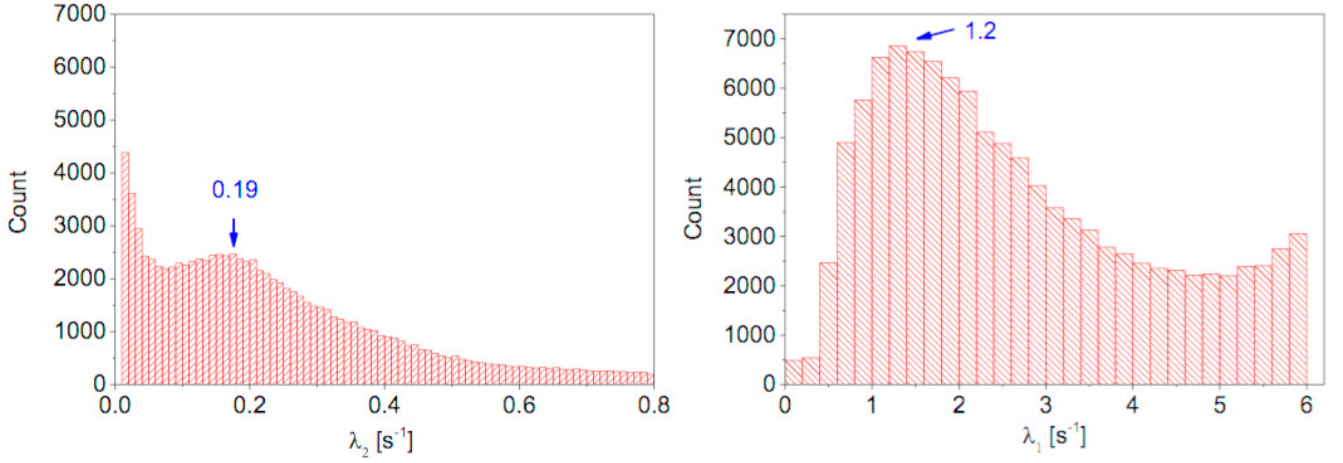
Fig. 4. In our experiments we also validated the model assumption that the time constants of tissue dynamics (left) λ_2 and fluid drainage (right) λ_1 can be separated by application of a large enough temperature gradient.

Dataset	Accuracy [%]	False Negative [%]	False Positive [%]
-8, h-spr-r	88.7	3.7	7.6
-8, h-pour	80	1.5	18.5
-3, h-spr-r	95.1	3.1	1.8
-3, h-pour	97.5	1.7	0.8
0, h-spr-r	95.9	3.4	0.7
0, h-pour	97.6	1.9	0.5
no irrigation, h	98.6	0.0	1.4

TABLE I

THIS TABLE LISTS THE PERFORMANCE OF THE PROPOSED IRRIGATION DETECTOR FRAMEWORK ON APPLIED IRRIGATIONS ON THE HAND SURFACE.

In order to validate the results, we segmented the infarct demarcation in pre- and postoperative computed tomography (CT) scans. After image registration of intraoperative thermal imaging with these CT recordings, we were able to correlate the results. CT recordings are acquired at varying amount of hours before and after the intervention hampering the comparison with intraoperative results in some cases. It is synchronize to correlate the time of the CT recording with the time of the underlying ischemic stroke. The findings of the application of our detection and classification scheme to intraoperative data are summarized in table II. We classified the results into three categories: positive, questionable, and negative. The majority of our evaluated cases show a correlation (positive result) of the λ_2 segmentation with the infarct demarcation in CT (see Fig. 5 as one example of this class). Yet, in one case, we observed a questionable result, wherein the λ_2 segmentation reveals more healthy tissue than being seen in the CT recording. We suppose this outcome to correlate with tissue of uncertain state meaning that the healthy classified tissue might be in a state in-between alive and dead. Latter assumption require more research regarding the approximation of the uncertain state by our assumed $N(\mu_u, \sigma_u)$. We further observed two case (id 1 and 2) with negative outcome. In case 1, the liquid was applied by the pour approach. Due to the increased curvature of the exposed cortex

caused by increased ICP, the fluid drained fast and didn't cause significant temperature propagations into deeper tissue layers. Therefore, no reliable λ_2 estimates could be achieved. Due to unknown thermodynamic and vascular effects, the exposed cortex at the infarct site in case 2 was colder than expected leading to the application of a too warm NaCl solution, which heated the cortex and did not impose any irrigation. Therefore, the detector couldn't recognize significant irrigations at certain sites (see Fig. 6). The other three 4 cases showed an evident correlation between the segmented temperature decay constant λ_2 and the infarct demarcation in CT measurements.

During our experiments, we encountered several challenges. In case of a low temperature gradient the estimated ΔT_2 of model equation 2 yielding potentially unreliable estimates of λ_2. Depending on the application of the liquid and the cortical curvature, it might not be possible to separate the drainage of fluid from tissue's warming process resulting in $\lambda_1 \approx \lambda_2$. Both challenges are primarily caused by high curvature or a too less amount of fluid being applied to the cortex. If the applied temperature gradient is too low, the tissue temperature returns to equilibrium temperature very fast. This prevents the projection of the temperature gradients into deeper tissue layers and prohibits adequate classification.

In general, the proposed irrigation detection framework achieved an accuracy of up to 97.6 %. This allowed us to

id	sex/age	pathology	result	comment
1	f/61	MCA infarct	negative	no temperature propagation due to increased ICP
2	f/61	MCA+ACA infarct	negative	liquid hotter than surface
3	m/59	MCA infarct	positive	
4	f/50	MCA infarct	questionable	to broad classification of healthy tissue
5	f/63	vasoplastic infarct	positive	
6	f/75	MCA infarct	positive	

TABLE II

OVERVIEW OF RESULTS FROM CLASSIFYING THE DECAY CONSTANT OF TISSUE HEATING AFTER APPLICATION OF AN INTRAOPERATIVE IRRIGATION TO THE CORTEX.
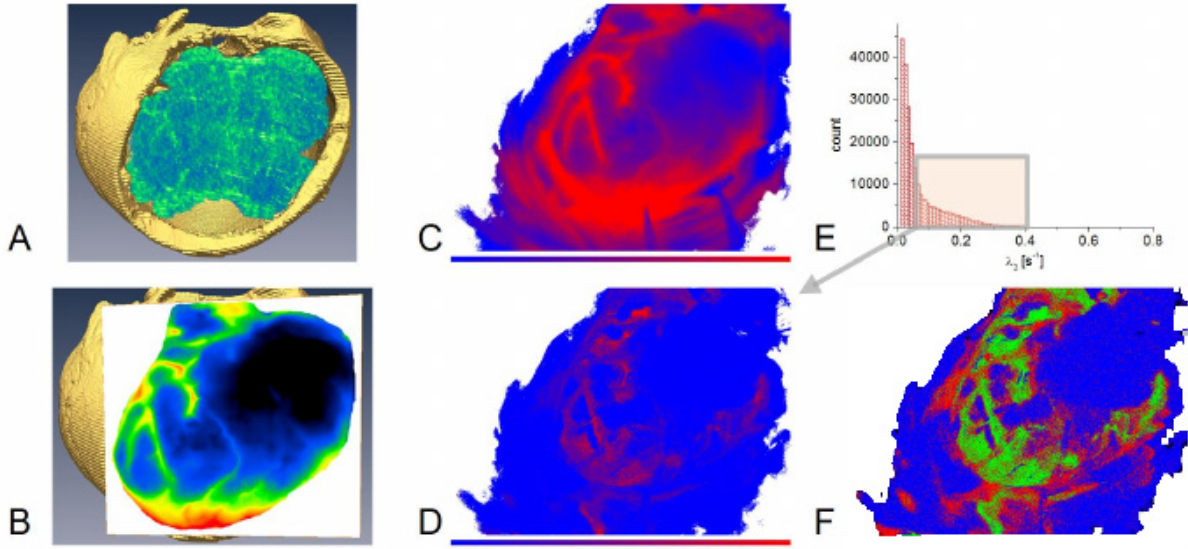

Fig. 5. This figure shows the results of case 5. In **A**, the infarct demarcation is segmented as green-blue in a post-operative CT recording. Subimage **B** shows the orientation of the thermal image to the CT dataset. **C** depicts the temperature distribution at equilibrium temperature after the irrigation. **D** displays the spatial distribution of λ_2 and **E** shows the histogram of all λ_2 values. **F** represents the segmentation as result of fitting the 3-Gaussian mixture model. Blue represents the ischemic / low perfusion state, green the healthy state and red representing uncertainty. The estimated underperfused tissue state strongly correlates with post-operative infarct demarcation. Some tissue is located near well perfused arteries (green) and might indicate areas that might be affected by further ischemic progression. Compared to the raw temperature image of **B** the results allow inferring more detailed information regarding the tissue perfusion.

estimate the parameters of discussed dynamic tissue temperature model. Hereby, we are able to quantify standardized thermodynamic properties of imaged tissue allowing conclusions regarding its perfusion state.

V. SUMMARY

Thermography is an emerging whitelight-independent, non-invasive method to measure the temperature distribution of surfaces. Active dynamic thermography allows us to quantify dynamic thermal behaviour by the application of temperature gradients. In the medical domain, this enables the detection of abnormal tissue and vascular pathologies.

In this study, we employ active dynamic thermography in order to analyze the perfusion of the exposed human cortex during neurosurgical interventions in case of ischemic strokes. The proposed method requires the application of a temperature gradient to the exposed cerebral cortex in order to recover information regarding its perfusion state. Temperature gradients are introduced by the application of cold NaCl irrigations

to the surface of the exposed cortex. These events are imaged and detected by a novel online machine learning framework. Following this, the tissue perfusion can be approximated by the estimation of the parameters of the discussed perfusion model. Its parameters include thermal decay constants that quantify the heating behavior of tissue.

We were the first to show that the intraoperative segmentation of temperature decay constants by a 3-Gaussian mixture model correlates with preoperative infarct demarcations in CT imaging. This enables the surgeon to recognize the progression of infarct demarcations from preoperative measurements to the actual intraoperative scene. Further research has to be done in order to improve the clinical significance of our results by an extensive validation study and advance the predictions of the machine learning framework. The estimated parameters yield a standardized representation of cortical perfusion meaning that the accuracy might be advanced by applying supervised learning.
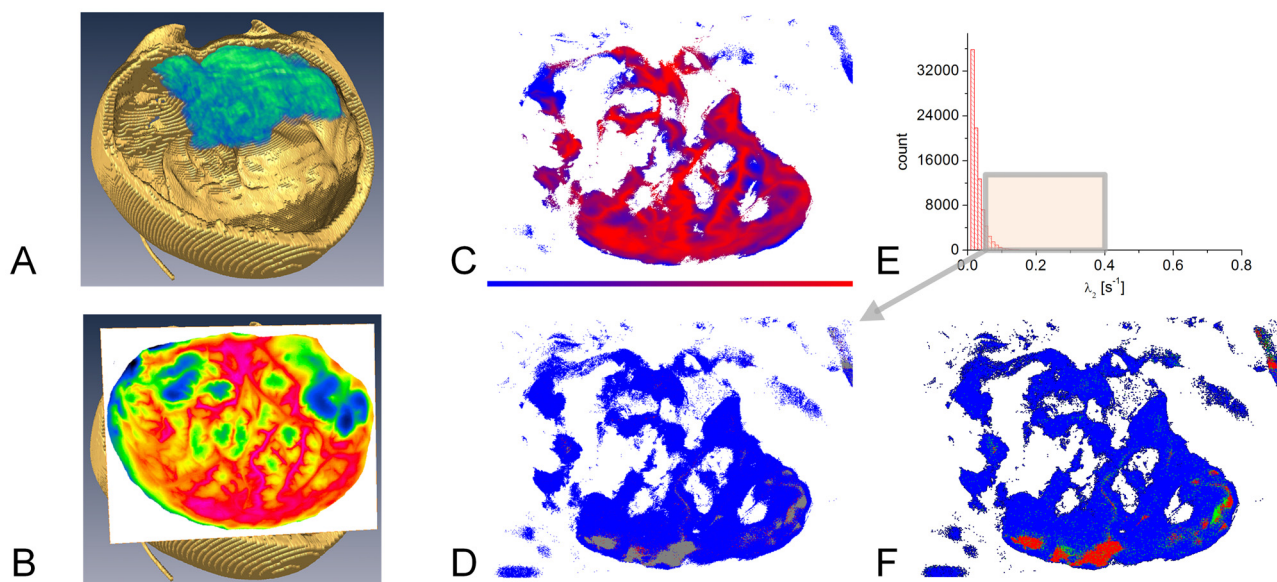
Fig. 6. In case 2, the applied liquid was partially hotter than the surface preventing meaningful results. The cause of this issue was the applied NaCl solution being partially hotter than the surface. Future investigations should therefore consist of a mechanism to provide NaCl liquid at constantly low temperature (e.g. $20^\circ C$). **A** resembles the segmented infarct demarcation while **B** shows the orientation of the thermal image with respect to the CT dataset. In **C**, the equilibrium temperature after the irrigation event with white pixels resembling rejected detections is imaged. **D** displays the spatial distribution of λ_2 and **E** shows the histogram of all λ_2 values. **F** represents the segmentation as result of fitting the 3-Gaussian mixture model.

VI. ACKNOWLEDGEMENT

REFERENCES

[1] A. M. Gorbach, J. D. Heiss, L. Kopylev, and E. H. Oldfield, "Intraoperative infrared imaging of brain tumors," *Journal of Neurosurgery*, vol. 101, no. 6, pp. 960–969, 2004, pMID: 15599965. [Online]. Available: http://thejns.org/doi/abs/10.3171/jns.2004.101.6.0960

[2] G. Steiner, S. B. Sobottka, E. Koch, G. Schackert, and M. Kirsch, "Intraoperative imaging of cortical cerebral perfusion by time-resolved thermography and multivariate data analysis," *Journal of Biomedical Optics*, vol. 16, no. 1, pp. 016 001–016 001–6, 2011. [Online]. Available: +http://dx.doi.org/10.1117/1.3528011

[3] A. Gorbach, J. D. Heiss, L. Kopylev, and E. H. Oldfield, "Intraoperative infrared imaging of brain tumors," *Journal of Neurosurgery*, 2004.

[4] P. Branemark, S. Fagerberg, L. Langer, and J. Soderbergh, "Infrared thermography in diabetes mellitus," *Diabetologia*, 1967.

[5] P. Sun, H. Lin, S. Jao, Y. Ku, R. Chan, and C. Cheng, "Relationship of skin temperature to sympathetic dysfunction in diabetic at-risk feet," *Diabetes Research and Clinical Practice*, 2006.

[6] R. Cesaris, A. Grimaldi, M. Balestrazzi, G. Ranieri, R. Chirappa, and F. Avantaggianto, "Changes in blood pressure and thermographic values resulting from use of a beta- blocker plus diuretic and of an alpha-betablocker plus diuretic," *Drugs Under Experimental and Clinical Research*, 1985.

[7] B. Gratt, S. Graff-Radford, V. Shetty, W. Solberg, and E. Sickles, "A six year clinical assessment of electronic facial thermography," *Dentomaxillofacial Radiology*, 1996.

[8] F. Ring, "Pandemic: thermography for fever screening of airport passengers," *Thermology International*, 2007.

[9] V. P. Vavilov, "Dynamic thermal tomography: Recent improvements and applications," *NDT & E International*, 2015.

[10] Z. S. Deng and J. Liu, "Enhancement of thermal diagnostics on tumors underneath the skin by induced evaporation," *Proc. 27th Annual Conference of IEEE Engineering in Medicine and Biology*, 2005.

[11] H. H. Pennes, "Analysis of tissue and arterial blood temperatures in the resting human forearm," *Journal of Applied Physiology*, 1948.

[12] G. Gutierrez and M. Giordano, "Study of the bioheat equation using monte carlo simulations for local magnetic hyperthermia," *Proc. ASME 2008 International Mechanical Engineering Congress and Exposition*, 2008.

[13] A. Nowakowski, *7. Quantitative active dynamic thermal IR-imaging and thermal tomography in medical diagnostics*. Taylor and Francis, 2013.

[14] L. Ye and E. Keogh, "Time series shapelets: A new primitive for data mining," *SIGKDD*, 2009.

[15] W. Gilks, S. Richardson, and D. Spiegelhalter, *Markov Chain Monte Carlo in Practice*. CRC Press, 1995.

[16] C. M. Bishop, *Pattern Recognition and Machine Learning*. Springer, 2006.

A.7. INTRAOPERATIVE FUNCTIONAL THERMAL IMAGING OF THE PRIMARY SENSORY CORTEX

N. Hoffmann, E. Koch, S. Gumhold, M. Kirsch, G. Steiner. Intraoperative functional thermal imaging of the primary sensory cortex. In: Proceedings of 16th CURAC Annual Conference, 2017.

Intraoperative functional thermal imaging of the primary sensory cortex

Nico Hoffmann[1], Edmund Koch[2], Stefan Gumhold[1], Matthias Kirsch[3], Gerald Steiner[2]

[1]Technische Universität Dresden, Computergraphik und Visualisierung, Dresden, Germany
[2]Technische Universität Dresden, Klinisches Sensoring und Monitoring, Dresden, Germany
[3]Universitätsklinikum „Carl Gustav Carus", Klinik und Poliklinik für Neurochirurgie, Dresden, Germany

```
contact: nico.hoffmann@tu-dresden.de
```

Abstract

Infrared cameras can be used to record the emitted heat radiation of the exposed human cortex during neurosurgical interventions. The main contributor to the thermal radiation of the cortex is regional cerebral blood flow. In case of tumour resections, the knowledge about eloquent areas is of vast importance since the removal of potential eloquent tissue might induce significant functional deficits. Furthermore, neurovascular coupling allows us to relate focal neural activity to changes in regional cerebral blood flow. Fortunately, changes in regional cerebral blood flow also alter the emitted heat radiation of the cortex, for what reason we propose a novel statistical data analysis framework in order to recognize and visualize these changes. This is achieved by integrating the thermal signature of these changes in cerebral blood flow as well as random effects into a generic semiparametric regression model which is then subject to a statistical inference procedure. The method was applied to a cohort of five intraoperative cases with promising results. We validated the detected eloquent areas with anatomical localization as well as electrophysiological measurements. The deterministic components can be adopted to general electrical stimulation protocols meaning that the framework allows to incorporate the expected behaviour for arbitrary experimental designs.

Keywords: Neurosurgery, Neuroimaging, Penalized Splines, Semiparametric Regression

1   Problem

In this work, we focus on neurosurgical interventions for the resection of brain tumours. Anaplastic and infiltrative (malignant) tumours are characterized by a weak differentiation between healthy and pathological tissue which hampers the resection of respective tissue. In case of tumour growth beneath functional areas, it is essential to minimize postoperative functional deficits in order to retain the patient's quality of life as long as possible. We approach this challenge by using intraoperative thermal imaging which is able to capture the emitted temperature radiation of tissue [9]. This radiation depends on the tissue's composition and dynamic processes such as cortical perfusion. It is a non-invasive and contactless imaging modality allowing us to detect temperature gradients up to $30\,mK$. The detected infrared radiation originates from the tissue's surface and interferes with the environment due to heat flow, convection and tissue cooling tissue making thermal images highly dynamic and nonstationary over time. In neurosurgery, the detected temperature gradients derive from perfusion- and neural activity related heat transfers beneath and at the exposed cortical surface. Compared to prevalent functional imaging modalities such as intraoperative optical imaging, TI is robust against various environmental conditions as it is a whitelight-independent method and is not affected by light reflections at the cortex. Steiner et al. [8] demonstrated the detection of an ice-cold saline solution applied through a central line as tool for tissue perfusion diagnostics using methods of multivariate statistics. Shevelev showed the general ability to measure neural activity by recording the heat distribution of rat brains in 1993 [7]. Gorbach [4] extended these results and had shown that sensoric and motor activity can be recognized by expensive cooled high-sensitive infrared cameras.

In a seminal paper, Friston et al. employed the general linear model (GLM) for analysis of functional imaging [2]. Additionally, the authors of [3] give a comprehensive overview on recent developments. They also showed

how to integrate experimental conditions into the general linear model to understand neural activity under various experimental conditions. Since then, effort was put into extending this framework to other imaging modalities such as SPECT [5]. The traditional GLM approach can be extended by non-parametric components which leads to semiparametric regression or partially linear models and originates back to 1988 [6]. These models join the deterministic components of state-of-the-art GLMs with non-parametric components such as B-Splines [1] to account for non-linear random behaviour. The latter can be observed in biomedical data as hysteresis effects in detectors might induce non-linear drifts or physiological signals might introduce periodic patterns or non-stationary behaviour (see Fig. 1).

In this study, we extend prior findings regarding the detection of functional areas using intraoperative thermal imaging (TI) by means of a sound statistical framework with respective inference procedures. The framework allows us to design and analyse arbitrary experimental conditions and setups. The generic formulation might also provide necessary tools to apply the framework to other imaging modalities as well.
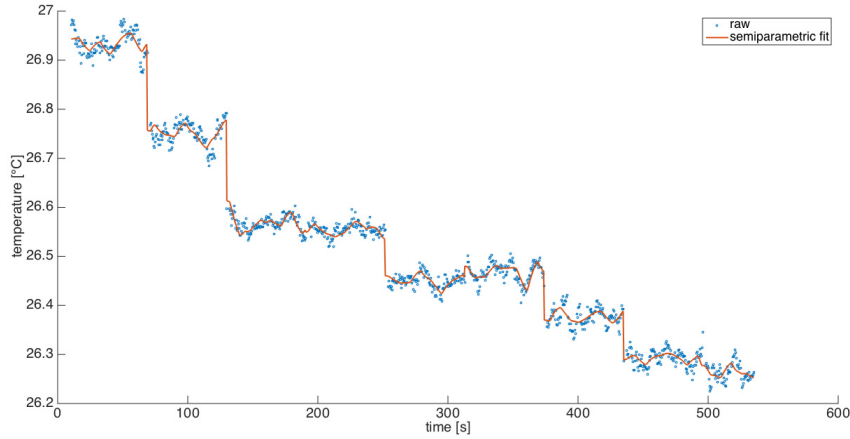

Fig. 1: The periodic non-uniformity correction of thermal imaging devices induces step artefacts into the timecourse which can be circumvented by adding additional degrees of freedom of the underlying non-parametric model at the respective timepoints.

2 Material and Methods

Intraoperative imaging data was acquired during resections of tumour tissue beneath the central sulcus. All intraoperative procedures were approved by the Human Ethics Committee of the Technische Universität Dresden (no. EK 323122008). The patients were under general anaesthesia wherein focal activations of the primary somatosensory cortex were provoked by contralateral median nerve stimulation.

Semiparametric regression extends simple linear regression by joining parametric as well as non-parametric components in order to model deterministic effects while compensating random non-linear behaviour. The non-parametric components typically describe autocorrelations of higher order which are a priori unknown. In the following, we will discuss necessary extensions to model the challenges of thermal imaging data in terms of the semiparametric regression framework to recognize the small thermal signatures correlating with changes in regional cerebral blood flow. In general, the semiparametric regression model reads

$$y = X\beta + Zb + e \tag{1}$$

given a length m time-series $y \in \mathbb{R}^m$, the design matrix $X \in \mathbb{R}^{k \times m}$ of k parametric components and coefficients $\beta \in \mathbb{R}^k$, a $k_1 + k_2$ dimensional non-parametric basis $Z \in \mathbb{R}^{k_1+k_2 \times m}$ with coefficients $b \in \mathbb{R}^{k_1+k_2}$ as well as normally distributed noise $e \sim N(0, \sigma I)$.

2.1 Intraoperative Functional Thermal Imaging

IR cameras consist of a focal-plane array of microbolometer detectors that convert incident electromagnetic radiation of the mid- to long IR range into electrical resistance changes which are then computed into temperature values. Hereby, the detector element, the optics and the camera body warm up until a convergence temperature is reached. This behaviour induces non-linear temperature drifts into the data that is compensated by a periodic gain and offset correction (non-uniformity correction (NUC) [9]). The NUC normalizes the data of each microbolometer and hereby gives a temperature and drift normalized image just after the NUC occurred. However, the NUC induces a jump discontinuity into the time-series of each pixel and alters the low frequency time-behaviour of the time series. This effect can be recognized in the mean temperature curve of a thermographic recording in Fig. 1. In the following, we extend the semiparametric regression framework in order to recognize deterministic patterns that correlate with evoked neural activity (section 2.2) while it compensates non-linear background noise (section 2.3).

2.2 Thermal Model for Neural Activity

The actual thermal imaging data is recorded intraoperatively during contralateral median nerve stimulation. This protocol consists of 10 periods where each period consists of 30 s resting-state condition followed by 30 s stimulation. The latter evokes neural activity which in turn initiates neurovascular coupling (NVC). Moreover, NVC alters the regional cerebral blood flow which results in changes of the tissue's temperature distribution. The latter propagate through several tissue layers before they are detected by the IR camera. Because of this behaviour, we approximate this signal by a smooth bell-like curve. Therefore, we model the expected signature of neural activity as Gaussian function

$$\gamma(t_i|\mu,\sigma) = \beta \exp(((t_i - \mu)/2\sigma)^2) \tag{2}$$

Here, $\mu \in \mathbb{R}^+$ denotes the point in time of maximum signal intensity while $\sigma \in \mathcal{R}^+$ describes the steepness of the temperature change. We further expect μ and σ to correlate with the depth of the focal activation. In fact, we expect neural activity of deeper tissue layers to correlate with a weaker amplitude and broader thermal signature. In this case, the signal's shape is also expected to have less curvature and therefore higher σ values. The design matrix X (eqn. 1) can be seen as dilated and shifted variants of eqn. 2. Suppose we are given time-points $[t_1 \dots t_m]$ with $t_i \in \mathbb{R}$, then we can discretize $\gamma(t_i|\mu, \sigma)$ by $\Gamma(\mu,\sigma) = [\gamma(t_1|\mu,\sigma)^T \dots \gamma(t_m|\mu,\sigma)^T]^T$. In case of k+1 electrical stimulations with a period of Δ_e, the design matrix becomes

$$X(\mu,\sigma) = [\Gamma(\mu,\sigma) \; \Gamma(\mu + \Delta_e,\sigma) \dots \; \Gamma(\mu + k\Delta_e,\sigma)] \tag{3}$$

given μ and σ.

2.3 Background Signals

Unfortunately, the NUC periodically induces a jump discontinuity and applies a slope correction to each microbolometer detector [9]. Furthermore, thermal time-series are superimposed by various high-frequent effects originating from physiological activity such as periodic patterns at heart rate as well as certain irregular components. We address the contributions of the NUC as well as the physiological effects by two orthogonal B-Spline components Z_1 and Z_2. The former, Z_1, is formed by a low number of knots k_1 and coefficients $b_1 \in \mathbb{R}^{k_1}$ to approximate low-frequent non-linear behaviour. Z_2 addresses high-frequent behaviour with $k_2 \gg k_1$ knots and coefficients $b_2 \in \mathbb{R}^{k_2}$. As stated, the NUC introduces a jump discontinuity into the data (see Fig. 1). To account for this issue, we estimate all j time-points t_j of each NUC and add an additional knot at t_j to Z_2. This approach introduces additional degrees-of-freedom to account for steep changes at respective time points.

2.4 Inference

Attention has to be paid to Z_2 since it might also approximate low-frequent behaviour and neural activity. To prevent this, we add a L_2 penalty to the wavelet transformed B-Spline estimate WZ_2b_2. Given the previously discussed experimental conditions X and our B-Splines Z_1, Z_2, we form $G = [X, Z_1, Z_2]$ and arrive at the minimization problem

$$\min_b \|G\rho - y\|_2^2 + \lambda\|PWGS\rho\|_2^2 \tag{4}$$

with $S = blkdiag(0_{k+k_1}, 1_{k_2})$ and coefficients $\rho = [\beta, b_1^T, b_2^T]^T$. The block-diagonal matrix S enforces that the penalty is solely applied to the estimate of Z_2. By letting $P = blkdiag(1_{128}, 0_{m-128})$, we restrict the penalty to the lower dyads 1 through 6 of the wavelet transform meaning that the second B-Spline component doesn't approximate respective behaviour. These lower dyads can be seen as an approximation of the low-frequency terms of Z_2b_2. This approach enables us to penalize the low-frequent behaviour of the estimated signal and can be thought of a high-pass filter. The penalized normal equations become

$$\rho(\lambda, \mu, \sigma) = (G^T G + \lambda S^T G^T W^T P^T PWGS)^{-1} G^T y \tag{5}$$

Akaike's Information Criterion (AIC) [6] and Generalized Cross-Validation (GCV) [6] can now be employed to optimize μ, σ and λ of equation 5. Finally, significant values of β can now be inferred by testing the null hypothesis $H_0: \beta = 0$ which leads to the t-statistics (see [6] for further details):
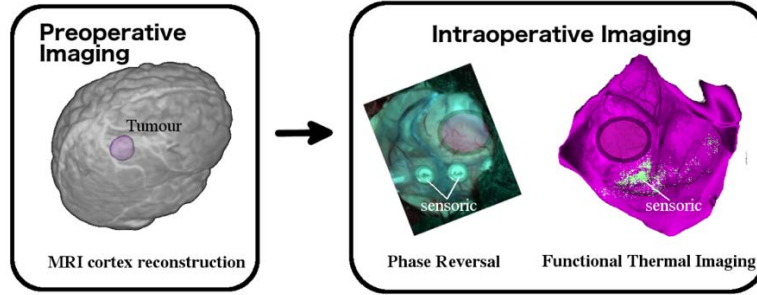
$$t = \beta/\sqrt{var(\beta)} \tag{6}$$

Fig. 2: This case suffered from a tumour on primary somatosensory cortex (purple circle). Phase reversal was observed between electrodes 2 and 3 whilst sensory activity was measured at electrodes 3 and 4. Analysing thermal imaging data with the proposed semiparametric regression framework allowed fine-grain localisation of cortical neural activity (statistically significant activations are visualized by green pixels)

3 Results

In this section, the performance of the proposed framework and respective metrics is quantified on synthetic data in section 3.1. Subsequently, these parameters are employed for the analysis of intraoperative thermal imaging data as discussed in section 3.2.

3.1 Simulation study

In order to evaluate our model using ground-truth information, we use intraoperative resting-state data of 640 x 480 pixels at 1024 time-points as baseline dataset. This dataset is being created by augmenting the resting-state data by the sampled activation function (eqn. 2) at certain amplitudes β and σ = 10 and μ = 15s. Without loss of generality, we expect a spatial extent of 2 cm in diameter of our activation function, meaning that a circular area of radius 5 pixels (347 pixels in total) is superimposed by our activation pattern while the resting-state behaviour of 306,853 baseline time courses is preserved. This ground-truth dataset allows us to evaluate the performance of AIC and GCV for optimizing the parameters of our regression model. The results are shown in table 1. Furthermore, two critical t-statistics, $t \geq 3.0$ ($p < 0.001$) and $t_{bonf} \geq 5.8$ (Bonferroni corrected $p < 0.001/m$), were examined for reasoning about values of β being significantly different from zero (see eqn. 6 and

[6] for details). A Signal-To-Noise ratio (SNR) of approximately one ($\beta = 0.03$) results in suboptimal performance of both GCV and AIC, however the best performance was achieved by AIC3.0 with a TPR of 0.15. In case of a SNR of approximately 4, we observe a TPR of 0.986 in case of AIC3.0 and acceptable 0.781 for GCV3.0. The three approaches AIC3.0, AIC5.8 and GCV3.0 resulted in good performance in case of signals with SNR of 6 with TPR > 0.87. The False-Positive-Rates of all four approaches are listed in table 1. GCV 5.8 showed nearly perfect FPR, yet at cost of a decreased overall performance.

	AIC3.0	AIC5.8	GCV3.0	GCV5.8
False-positive rate	0.023	0.0002	0.042	0.0001
True-positive rate	0.986	0.648	0.781	0.539

Table 1 This table lists the false-positive and true-positive rates of various approaches for parameter optimization and significance testing applied to the synthetic dataset at a SNR of 4.

3.2 Somatosensory Evoked Potentials

Contralateral electrical stimulation was applied to the patient's median nerve as described in section 2.1. A continuous stream of thermal images of the cerebral cortex was recorded during electrophysiology and subject to the described regression analysis. As discussed earlier, we expect changes in the cortical heat distribution of tissue near to the hand areal of the primary somatosensory cortex. However, both the shape σ and the time to peak μ of the neural activation (eqn. 2) are unknown meaning that we have to estimate them by a grid search. The sensory activity of the exposed cortical tissue was further assessed by electrophysiological measurements (phase reversal). Table 2 lists the results of analysing the thermographic recordings by the proposed semiparametric regression framework. The column activation TI lists the results after testing the parameter of the activation function with respect to t_{Bonf} and AIC parameter optimization. By positive we denote cases with a dense cluster of pixels comprising of significantly increased t-statistics ($t > t_{bonf}$) within the postcentral gyrus (see Fig. 2). Weak activation denotes a sparse cluster of significant pixels within the postcentral gyrus.

Case	age / sex	pathology	location	activation TI	phase reversal
1	58 / m	Met. Adeno-Ca.	precentral l.	positive	positive
2	33 / f	Met. Mamma-Ca.	parietal l.	positive	positive
3	79 / m	Met. Melanoma	frontoparietal r.	positive	positive
4	72 / f	Glioblastoma	parietal r.	weak	positive
5	69 / m	Glioblastoma	parietooccipital l.	positive	positive

Table 2 Results of applying the semiparametric regression model to intraoperative functional thermal imaging data.

4 Discussion

The results indicate that AIC is an appropriate measure for optimizing the parameters of the proposed semiparametric regression framework. Depending on the actual signal strength, the very conservative Bonferroni corrected t-statistic yields good true positive rates while minimizing FPRs as required for medical decision support systems. The analysis of four cases resulted in a dense cluster of active pixels on the postcentral gyrus (see for example Fig. 2). However, a single case showed a significant focal temperature change in a vessel on the postcentral gyrus and solely a sparse activation pattern on the same gyrus. The latter might be due to the fact that we proposed to compute Bonferroni corrected t-statistics. This measure is very conservative and neglects potential spatial correlation among adjacent pixels and might decrease the overall sensitivity. In all cases, we found that that the position of the estimated statistically significant eloquent sites correlates with the expected functional activity on the primary sensory cortex as validated by phase reversal. In general, we demonstrated the applicability of the semiparametric regression for analysis of thermal imaging data of the human cortex.

5   Conclusion

Postoperative functional limitations or deficits significantly affect the patient's outcome for what reason tissue resections should be supported by robust intraoperative imaging modalities to visualize neural activity. The visualization of neural activity during neurosurgical tumour resections might therefore guide medical decision regarding the extent of tumour mass removal. Therefore, we extended the GLM framework by semiparametric regression methods in order to recognize the thermal signature of focal neural activity in intraoperative thermal imaging data. For this purpose, neural activity on the sensory cortex was provoked intraoperatively by contralateral stimulation of the median nerve whilst the heat distribution of the cerebral cortex was recorded intraoperatively by an IR camera. The proposed penalized semiparametric model includes the expected thermal signature of neural activity as well as characteristic thermal behaviour of the human cortex and IR cameras. The latter can be seen as a combination of periodic discontinuity points, non-linear temporal drifts as well as perfusion changes relating to cortical autoregulation. In 4 of 5 cases, the proposed method resulted in promising results to visualize neural activity of the somatosensory cortex. The results were further validated by anatomic localization as well as phase reversal. In general, we demonstrated the applicability of intraoperative thermal imaging to visualize statistically significant eloquent areas of the exposed human cortex.

Acknowledgement

References

[1] C. DeBoor, A practical guide to splines, Springer-Verlag, New York (1978).

[2] K. J. Friston, A. P. Holmes, K. J. Worsley, J.-P. Poline, C. D. Frith, and R. S. J. Frackowiak, Statistical parametric maps in functional imaging: A general linear approach, Hum. Brain Mapp., 2 189–22 (1994)

[3] K. J. Friston, J. T. Ashburner, S. Kiebel, T. E. Nichols, and W. D. Penny, Statistical Parametric Mapping: The Analysis of Functional Brain Images, Elsevier, London (2006)

[4] A. M. Gorbach, J. Heiss, C. Kufta, S. Sato, P. Fedio, W. A. Kammerer, J. Solomon, and E. H. Oldfield, Intraoperative infrared functional imaging of human brain, Ann. of Neurol., 54 297–310 (2003)

[5] K. A. McNally, A. L. Paige, G. Varghese, H. Zhang, E. J. Novotny, S. S. Spencer, I. G. Zubal, and H. Blumenfeld. Localizing Value of Ictal–Interictal SPECT Analyzed by SPM, Epilepsia, 46 1450–1465 (2005)

[6] D. Ruppert, M. P. Wand, and R. J. Carroll, Semiparametric Regression, Cambridge University Press, New York (2003)

[7] I. A. Shevelev, E. N. Tsicalov, A. M. Gorbach, K. P. Budko, and G. A. Sharaev, Thermoimaging of the brain, J. Neurosci. Methods, 46 49–58 (1993)

[8] G. Steiner, S. B. Sobottka, E. Koch, G. Schackert, and M. Kirsch, Intraoperative imaging of cortical cerebral perfusion by time-resolved thermography and multivariate data analysis, J Biomed Opt., 16 16001–616007 (2011)

[9] M. Vollmer and K.-P. Möllmann, Infrared Thermal Imaging: Fundamentals, Research and Applications, WILEY-VCH, Weinheim (2010)

LIST OF PUBLICATIONS

1. J. Hollmach, N. Hoffmann, C. Schnabel, S. Küchler, S. Sobottka, M. Kirsch, G. Schackert, E. Koch, G. Steiner. Highly sensitive time-resolved thermography and multivariate image analysis of the cerebral cortex for intrasurgical diagnostics. In: Proceedings of SPIE 8565, 856550, 2013.

2. Florian Weidner, N. Hoffmann, Yordan Radev, J. Hollmach, C. Schnabel, M. Kirsch, G. Schackert, U. Petersohn, E. Koch, G. Steiner. Entwicklung eines Gehirnphantoms zur Perfusions- und Brain Shift Simulation. In: A. Förster, J. Füssel, M. Gelinsky, E. Koch, H. Malberg, W. Vonau, editors, Reports on Biomedical Engineering - Band 2: 5. Dresdner Medizintechnik-Symposium, pages 111 – 113, 2014.

3. N. Hoffmann, J. Hollmach, C. Schnabel, Y. Radev, M. Kirsch, U. Petersohn, E. Koch, G. Steiner. Wavelet subspace analysis of intraoperative thermal imaging for motion filtering. Lecture Notes in Computer Science, 8815:411 – 420, 2014.

4. V. Senger*, N. Hoffmann*, J. Müller, J. Hollmach, C. Schnabel, Y. Radev, J. Müller, M. Kirsch, U. Petersohn, G. Steiner, E. Koch, R. Tetzlaff. Motion correction of thermographic images in neurosurgery: Performance comparison. In Biomedical Circuits and Systems Conference (BioCAS), pages 121 – 124, 2014. [* both authors contributed equally to this work.]

5. N. Hoffmann, Y. Radev, J. Hollmach, C. Schnabel, M. Kirsch, G. Schackert, U. Petersohn, E. Koch, G. Steiner. Gaussian mixture models for classification of perfused blood vessels in intraoperative thermography. Biomedical Engineering / Biomedizinische Technik. 59(S1):596 - 599, 2014.

6. J. Hollmach, Yordan Radev, N. Hoffmann, C. Schnabel, S. Sobottka, M. Kirsch, G. Schackert, E. Koch, G. Steiner. Intraoperative perfusion imaging of the cerebral cortex by time-resolved thermography. Biomedical Engineering / Biomedizinische Technik 59(S1), pages 608 – 611, 2014.

7. J. Hollmach, C. Schnabel, N. Hoffmann, Yordan Radev, G. Steiner, G. Schackert, E. Koch, M. Kirsch. Intraoperative imaging of cortical perfusion by time-resolved thermography using cold bolus approach. In: Proceedings of SPIE 9036, 903627, 2014.

8. N. Hoffmann, F. Weidner, C. Schnabel, E. Koch, G. Steiner, U. Petersohn, M. Kirsch. Incorporating MRI structural information into intraoperative functional thermography in neurosurgery. In: Proceedings of 15th CURAC Annual Conference, 2016.

9. N. Hoffmann, E. Koch, U. Petersohn, M. Kirsch, G. Steiner. Cerebral cortex classification by conditional random fields applied to intraoperative thermal imaging. Current Directions in Biomedical Engineering. 2(1): 475-478, 2016.

10. N. Hoffmann, G. Drache, E. Koch, G. Steiner, M. Kirsch, U. Petersohn. Quantification and Classification of Cortical Perfusion during Ischemic Strokes by Intraoperative Thermal Imaging. TU Dresden technical report TUD-FI16-02, 2016.

11. N. Hoffmann, F. Weidner, P. Urban, T. Meyer, C. Schnabel, U. Petersohn, E. Koch, S. Gumhold, G. Steiner, M. Kirsch. Framework for 2D-3D image fusion of infrared thermography with preoperative MRI. Biomedical Engineering / Biomedizinische Technik, 2017.

12. N. Hoffmann, E. Koch, S. Gumhold, M. Kirsch, G. Steiner. Intraoperative functional thermal imaging of the primary sensory cortex. In: Proceedings of 16th CURAC Annual Conference, 2017.

BIBLIOGRAPHY

[1] J. R. Adler, S. D. Chang, M. J. Murphy, J. Doty, P. Geis, and S. L. Hancock. The cyberknife: a frameless robotic system for radiosurgery. *Stereotactic and functional neurosurgery*, 1997.

[2] M. M. Alauddin. Positron emission tomography (PET) imaging with (18)F-based radiotracers. *American journal of nuclear medicine and molecular imaging*, 2(1):55–76, 2012. doi: 2160-8407/ajnmmi1109002Review.

[3] J. Ashburner and K. J. Friston. Voxel-Based Morphometry—The Methods. *NeuroImage*, 11(6):805–821, 2000. doi: 10.1006/nimg.2000.0582.

[4] M. Behbahaninia, N. L. Martirosyan, J. Georges, J. a. Udovich, M. Y. S. Kalani, B. G. Feuerstein, P. Nakaji, R. F. Spetzler, and M. C. Preul. Intraoperative fluorescent imaging of intracranial tumors: A review. *Clinical Neurology and Neurosurgery*, 115(5):517–528, 2013. doi: 10.1016/j.clineuro.2013.02.019.

[5] Y. Bengio and P. Lamblin. Greedy layer-wise training of deep networks. *Advances in Neural Information Processing Systems 19 (NIPS'2006)*, (1):153–160, 2007.

[6] M. S. J. Berwick and M. Jones. Linear superposition of sensory-evoked and ongoing cortical. *Frontiers Neuroenergetics*, 2010.

[7] M. Billinger, C. Brunner, and G. R. Müller-Putz. SCoT: a Python toolbox for EEG source connectivity. *Frontiers in neuroinformatics*, 8(March):22, 2014. doi: 10.3389/fninf.2014.00022.

[8] M. Billinger, C. Brunner, and G. R. Müller-Putz. Online visualization of brain connectivity. *Journal of Neuroscience Methods*, 256:106–116, 2015. doi: 10.1016/j.jneumeth.2015.08.031.

[9] Blausen.com. Blausen gallery 2014. *Wikiversity Journal of Medicine*, 1(2), 2015.

[10] B. G. Booth, S. P. Miller, C. J. Brown, K. J. Poskitt, V. Chau, R. E. Grunau, A. R. Synnes, and G. Hamarneh. STEAM - Statistical Template Estimation for Abnormality Mapping: A personalized DTI analysis technique with applications to the screening of preterm infants. *NeuroImage*, 125:705–723, 2016. doi: 10.1016/j.neuroimage.2015.08.079.

[11] R. Braunschweig, J. Müller, J. Müller, and R. Tetzlaff. Nero mastering 300k cnn cells. In *European Conference on Circuit Theory and Design*, pages 1–4, 2013.

[12] P. Brodal. *The Central Nervous System*. Oxford University Press, New York, 4th edition, 2010.

[13] R. P. Cabeen, M. E. Bastin, and D. H. Laidlaw. Kernel Regression Estimation of Fiber Orientation Mixtures in Diffusion MRI. *NeuroImage*, 127:158–172, 2015. doi: http://dx.doi.org/10.1016/j.neuroimage.2015.11.061.

[14] R. Cesaris, A. Grimaldi, M. Balestrazzi, G. Ranieri, R. Chirappa, and F. Avantaggianto. Changes in blood pressure and thermographic values resulting from use of a beta-blocker plus diuretic and of an alpha-betablocker plus diuretic. *Drugs Under Experimental and Clinical Research*, 1985.

[15] J. Chalela, C. Kidwell, L. Nentwich, M. Luby, J. Butman, A. Demchuk, M. Hill, N. Patronas, L. Latour, and S. Warach. Magnetic resonance imaging and computed tomography in emergency assessment of patients with suspected acute stroke: a prospective comparison. *Lancet*, 2007.

[16] D. Chicco, P. Sadowski, and P. Baldi. Deep autoencoder neural networks for gene ontology annotation predictions. *Proceedings of the 5th ACM Conference on Bioinformatics, Computational Biology, and Health Informatics - BCB '14*, pages 533–540, 2014. doi: 10.1145/2649387.2649442.

[17] J. Clarke. Squids. *Scientific American*, 1994.

[18] D. Comanicu and P. Meer. Mean shift: A robust approach toward feature space analysis. *IEEE Trans. Pattern Anal. Machine Intell.*, 24(5):603–619, 2002. doi: 10.1109/34.1000236.

[19] X. Cui, S. Bray, D. M. Bryan, G. H. Glover, and A. L. Reiss. A quantitative comparison of NIRS and fMRI across multiple cognitive tasks. *NeuroImage*, 54(4):2808–2821, 2011. doi: 10.1016/j.neuroimage.2010.10.069.A.

[20] C. DeBoor. *A practical guide to splines*. Springer-Verlag, New York, 1st edition, 1978.

[21] C. Demene, E. Tiran, L. A. Sieu, A. Bergel, J. L. Gennisson, M. Pernot, T. Deffieux, I. Cohen, and M. Tanter. 4D microvascular imaging based on ultrafast Doppler tomography. *NeuroImage*, 127:472–483, 2015. doi: 10.1016/j.neuroimage.2015.11.014.

[22] S. Dimou, R. A. Battisti, D. F. Hermens, and J. Lagopoulos. A systematic review of functional magnetic resonance imaging and diffusion tensor imaging modalities used in presurgical planning of brain tumour resection. *Neurosurgical Review*, 36(2):205–214, 2013. doi: 10.1007/s10143-012-0436-8.

[23] O. Dössel and T. M. Buzug, editors. *Biomedizinische Technik - Medizinische Bildgebung*. DeGruyter, Berlin Boston, 2014.

[24] D. D. Dougherty, S. L. Rauch, and J. F. Rosenbaum. *Essentials of Neuroimaging for Clinical Practice*. Amer Psychiatric Pub Inc, 2004.

[25] K. B. Duan, J. C. Rajapakse, H. Wang, and F. Azuaje. Multiple SVM-RFE for gene selection in cancer classification with expression data. *IEEE Transactions on Nanobioscience*, 4(3):228–233, 2005. doi: 10.1109/TNB.2005.853657.

[26] R. Duncan, editor. *SPECT Imaging of the Brain.* Kluwer Academic Publishers, Dordrecht, 1997.

[27] P. Dupont, W. Van Paesschen, A. Palmini, R. Ambayi, J. Van Loon, J. Goffin, S. Weckhuysen, S. Sunaert, B. Thomas, P. Demaerel, R. Sciot, A. J. Becker, H. Vanbilloen, L. Mortelmans, and K. Van Laere. Ictal perfusion patterns associated with single MRI-visible focal dysplastic lesions: Implications for the noninvasive delineation of the epileptogenic zone. *Epilepsia*, 47(9):1550–1557, 2006. doi: 10.1111/j.1528-1167.2006.00628.x.

[28] P. H. Eilers, I. D. Currie, and M. Durban. Fast and compact smoothing on large multidimensional grids. *Computational Statistics & Data Analysis*, 50(1):61–76, Jan. 2006.

[29] K. J. Friston, J. T. Ashburner, S. Kiebel, T. E. Nichols, and W. D. Penny. *Statistical Parametric Mapping: The Analysis of Functional Brain Images*. Academic Press, 1st edition, 2007.

[30] B. Gaonkar, R. T Shinohara, and C. Davatzikos. Interpreting support vector machine models for multivariate group wise analysis in neuroimaging. *Medical image analysis*, 24(1):190–204, 2015. doi: 10.1016/j.media.2015.06.008.

[31] T. Gazit, I. Doron, O. Sagher, M. H. Kohrman, V. L. Towle, M. Teicher, and E. Ben-Jacob. Time-frequency characterization of electrocorticographic recordings of epileptic patients using frequency-entropy similarity: A comparison to other bi-variate measures. *Journal of Neuroscience Methods*, 194(2):358–373, 2011. doi: 10.1016/j.jneumeth. 2010.10.011.

[32] W. Gilks, S. Richardson, and D. Spiegelhalter, editors. *Markov Chain Monte Carlo in Practice*. Chapman & Hall, London, 1st edition, 1996.

[33] A. M. Gorbach, J. Heiss, C. Kufta, S. Sato, P. Fedio, W. A. Kammerer, J. Solomon, and E. H. Oldfield. Intraoperative infrared functional imaging of human brain. *Annals of Neurology*, 54:297–310, 2003.

[34] A. M. Gorbach, J. D. Heiss, L. Kopylev, and E. H. Oldfield. Intraoperative infrared imaging of brain tumors. *J Neurosurg*, 101(6):960–969, 2004. doi: 10.3171/jns.2004. 101.6.0960.

[35] B. Gratt, S. Graff-Radford, V. Shetty, W. Solberg, and E. Sickles. A six year clinical assessment of electronic facial thermography. *Dentomaxillofacial Radiology 1996, 25, 247*, 1996.

[36] J. C. Griffis, J. B. Allendorfer, and J. P. Szaflarski. Voxel-based Gaussian naive Bayes classification of ischemic stroke lesions in individual T1-weighted MRI scans. *Journal of Neuroscience Methods*, 257:97–108, 2016. doi: 10.1016/j.jneumeth.2015.09.019.

[37] C.-A. Guillermo, A. Furdea, K. Takano, C. A. Ruf, H. Flor, and N. Birbaumer. Brain Communication in a Completely Locked-In Patient using Bedsinde Near-Infrared Spectroscopy. *Neurology*, 82:1930–1932, 2014. doi: 10.1212/NXI.0000000000000086.

[38] C. Guy and D. ffytche. *An Introduction to the Principles of Medical Imaging*. Imperial College Press, London, 2005.

[39] M. Haglund and D. Hochman. Imaging of intrinsic optical signals in primate cortex during epileptiform activity. *Epilepsia*, 2007.

[40] J. Harbison, A. Massey, L. Barnett, D. Hodge, and G. Ford. Rapid ambulance protocol for acute stroke. *Lancet*, 1999.

[41] M. P. Heinrich, I. J. A. Simpson, B. W. Papiez, S. M. Brady, and J. A. Schnabel. Deformable image registration by combining uncertainty estimates from supervoxel belief propagation. *Medical Image Analysis*, 27:57–71, 2016. doi: 10.1016/j.media.2015. 09.005.

[42] P. U. Heuschmann, O. Busse, M. Wagner, M. Endres, A. Villringer, J. Röther, P. L. Kolominsky-Rabas, and K. Berger. Schlaganfallhäufigkeit und versorgung von schlaganfallpatienten in deutschland. *Aktuelle Neurologie*, 2010.

[43] K. Hunter, T. Blaxton, S. Bookheimer, C. Figlozzi, W. Gaillard, C. Grandin, A. Anyanwu, and W. Theodore. (15)o water positron emission tomography in language localization: a study comparing positron emission tomography visual and computerized region of interest analysis with the wada test. *Ann Neurol.*, 1999.

[44] A. Irimia, B. Wang, S. R. Aylward, M. W. Prastawa, D. F. Pace, G. Gerig, D. A. Hovda, R. Kikinis, P. M. Vespa, and J. D. Van Horn. Neuroimaging of structural pathology and connectomics in traumatic brain injury: Toward personalized outcome prediction. *NeuroImage: Clinical*, 1(1):1–17, 2012. doi: 10.1016/j.nicl.2012.08.002.

[45] F. Jolesz, editor. *Intraoperative Imaging and Image-Guided Therapy*. Springer-Verlag, New York, 2014.

[46] P. Kaatsch, C. Spix, S. Hentschel, A. Katalinic, S. Luttmann, C. Stegmaier, S. Caspritz, J. Cernaj, A. Ernst, J. Folkerts, J. Hansmann, K. Kranzhöfer, E. Kriegho-Henning, B. Kunz, A. Penzkofer, K. Treml, K. Wittenberg, N. Baras, B. Barnes, J. Bertz, N. Buttmann-Schweiger, S. Dahm, M. Franke, J. Haberland, K. Kraywinkel, A. Wienecke, and U. Wolf. Krebs in deutschland 2009/2010. häufigkeiten und trends. *Beiträge zur Gesundheitsberichterstattung des Bundes*, 2013.

[47] Z. Karimaghaloo, D. L. Arnold, and T. Arbel. Adaptive multi-level conditional random fields for detection and segmentation of small enhanced pathology in medical images. *Medical Image Analysis*, 27:17–30, 2016. doi: 10.1016/j.media.2015.06.004.

[48] A. H. Kaye and E. R. Laws. *Brain Tumors. An Encyclopedic Approach*. Saunders, 3rd edition, 2011.

[49] N. Kriegeskorte, M. Mur, and P. a. Bandettini. Representational similarity analysis - connecting the branches of systems neuroscience. *Frontiers in systems neuroscience*, 2(November):4, 2008. doi: 10.3389/neuro.06.004.2008.

[50] T. Krings, B. Buchbinder, W. Butler, K. Chiappa, H. Jiang, G. Cosgrove, and B. Rosen. Functional magnetic resonance imaging and transcranial magnetic stimulation: complementary approaches in the evaluation of cortical motor function. *Neurology*, 1997.

[51] Z. Lai, X. Qu, Y. Liu, D. Guo, J. Ye, Z. Zhan, and Z. Chen. Image reconstruction of compressed sensing MRI using graph-based redundant wavelet transform. *Medical Image Analysis*, 27:93–104, 2016. doi: 10.1016/j.media.2015.05.012.

[52] M. Lavine, M. M. Haglund, and D. W. Hochman. Dynamic linear model analysis of optical imaging data acquired from the human neocortex. *Journal of Neuroscience Methods*, 199(2):346–362, 2011. doi: 10.1016/j.jneumeth.2011.05.017.

[53] S. K. Lee, S. Y. Lee, K. K. Kim, K. S. Hong, D. S. Lee, and C. K. Chung. Surgical outcome and prognostic factors of cryptogenic neocortical epilepsy. *Annals of Neurology*, 58(4): 525–532, 2005. doi: 10.1002/ana.20569.

[54] Y. Li, R. Rey-Dios, D. W. Roberts, P. A. Valdés, and A. A. Cohen-Gadol. Intraoperative fluorescence-guided resection of high-grade gliomas: A comparison of the present techniques and evolution of future strategies. *World Neurosurgery*, 2014.

[55] R. Lorenz, R. P. Monti, I. R. Violante, C. Anagnostopoulos, A. Aldo, G. Montana, and R. Leech. The Automatic Neuroscientist : automated experimental design with real-time fMRI. *NeuroImage*, 129:1–22, 2016. doi: 10.1016/j.neuroimage.2016.01.032.

[56] D. N. Louis, H. Ohgaki, O. D. Wiestler, W. K. Cavenee, P. C. Burger, A. Jouvet, B. W. Scheithauer, and P. Kleihues. World health organization classification of tumours of the central nervous system. *Acta Neuropathalogica*, 2007.

[57] J. Lv, X. Jiang, X. Li, D. Zhu, H. Chen, T. Zhang, S. Zhang, X. Hu, J. Han, H. Huang, J. Zhang, L. Guo, and T. Liu. Sparse representation of whole-brain fMRI signals for identification of functional networks. *Medical Image Analysis*, 20(1):112–134, 2015. doi: 10.1016/j.media.2014.10.011.

[58] N. Martirosyan, D. Cavalcanti, J. Eschbacher, P. Delaney, A. Scheck, M. Abdelwahab, P. Nakaji, R. Spetzler, and M. Preul. Use of in vivo near-infrared laser confocal endomicroscopy with indocyanine green to detect the boundary of infiltrative tumor. *Journal of Neurosurgery*, 2011.

[59] M. Mehta, M. A. Vogelbaum, S. Chang, and N. Patel. *Cancer: Principles & Practice of Oncology*, chapter Neoplasms of the Central Nervous System. Lippincott Williams & Wilkins, Philadelphia, 9th edition, 2011.

[60] T. Meyer, S. B. Sobottka, M. Kirsch, G. Schackert, R. Steinmeier, E. Koch, and U. Morgenstern. Intraoperative optical imaging of functional brain areas for improved image-guided surgery. *Biomedical Engineering / Biomedizinische Technik*, 58:225–236, 2013.

[61] H. Mi, C. Petitjean, P. Vera, and S. Ruan. Joint tumor growth prediction and tumor segmentation on therapeutic follow-up PET images. *Medical Image Analysis*, 23(1): 84–91, 2015. doi: 10.1016/j.media.2015.04.016.

[62] T. J. Mitchell, C. D. Hacker, J. D. Breshears, N. P. Szrama, M. Sharma, D. T. Bundy, M. Pahwa, M. Corbetta, A. Z. Snyder, J. S. Shimony, and E. C. Leuthardt. A novel data-driven approach to preoperative mapping of functional cortex using resting-state functional magnetic resonance imaging. *Neurosurgery*, 73(6):969–983, 2013. doi: 10. 1227/NEU.0000000000000141.

[63] A. Nabavi, C. T. Mamisch, D. T. Gering, D. F. Kacher, R. S. Pergolizzi, W. M. Wells, R. Kikinis, P. M. Black, and F. A. Jolesz. Image-guided therapy and intraoperative mri in neurosurgery. *Minim Invasiv Ther*, 9(3-4):277–286, 2000.

[64] N. Naseer, M. J. Hong, and K.-S. Hong. Online binary decision decoding using functional near-infrared spectroscopy for the development of brain-computer interface. *Experimental brain research*, 232(2):555–64, 2014. doi: 10.1007/s00221-013-3764-1.

[65] H. Nili, C. Wingfield, A. Walther, L. Su, W. Marslen-Wilson, and N. Kriegeskorte. A Toolbox for Representational Similarity Analysis. *PLoS Computational Biology*, 10(4), 2014. doi: 10.1371/journal.pcbi.1003553.

[66] A. Nowakowski. *Quantitative Active Dynamic Thermal IR-Imaging and Thermal Tomography in Medical Diagnostics*, pages 1–30. CRC Press, 2016/01/17 2012. doi: doi:10.1201/b12938-8.

[67] H. Obrig and A. Villringer. Beyond the visible - Imaging the human brain with light. *Journal of Cerebral Blood Flow and Metabolism*, 23(1):1–18, 2003. doi: 10.1097/01. WCB.0000043472.45775.29.

[68] S. Ohue, S. Kohno, A. Inoue, D. Yamashita, H. Harada, Y. Kumon, K. Kikuchi, H. Miki, and T. Ohnishi. Accuracy of diffusion tensor magnetic resonance imaging-based tractography for surgery of gliomas near the pyramidal tract: A significant correlation between subcortical electrical stimulation and postoperative tractography. *Neurosurgery*, 70(2):283–294, 2011. doi: 10.1227/NEU.0b013e31823020e6.

[69] K. Ota, N. Oishi, K. Ito, and H. Fukuyama. Effects of imaging modalities, brain atlases and feature selection on prediction of Alzheimer's disease. *Journal of Neuroscience Methods*, 256:168–183, 2015. doi: 10.1016/j.jneumeth.2015.08.020.

[70] K. Poeck. *Neurologie*. Springer-Lehrbuch, Berlin Heidelberg, 8th edition, 1993.

[71] B. W. Pogue, S. Gibbs-Strauss, P. A. Valdés, K. Samkoe, D. W. Roberts, and K. D. Paulsen. Review of neurosurgical fluorescence imaging methodologies. *IEEE J Sel Top Quantum Electron*, 16(3):493–505, 2010.

[72] A. Rahmim and H. Z. H. Pet versus spect: strengths, limitations and challenges. *Nuclear Medicine Communications*, 2008.

[73] E. F. J. Ring and K. Ammer. Infrared thermal imaging in medicine. *Physiological Measurement*, 33(3):R33–R46, 2012. doi: 10.1088/0967-3334/33/3/R33.

[74] F. Ring. Pandemic: thermography for fever screening of airport passengers. *Thermology International*, 2007.

[75] P. E. Roland. *Brain activation*. Wiley-Liss, New York, 1997.

[76] S. Rueda, C. L. Knight, A. T. Papageorghiou, and J. A. Noble. Feature-based fuzzy connectedness segmentation of ultrasound images with an object completion step. *Medical Image Analysis*, 26(1):30–46, 2015. doi: 10.1016/j.media.2015.07.002.

[77] E. Samset and H. Hirschberg. Neuronavigation in intraoperative mri. *Computer Aided Surgery*, 1999.

[78] J. L. Saver, G. C. Fonarow, E. E. Smith, M. J. Reeves, M. V. Grau-Sepulveda, W. Pan, D. M. Olson, A. F. Hernandez, E. D. Peterson, and L. H. Schwamm. Time to treatment with intravenous tissue plasminogen activator and outcome from acute ischemic stroke. *Journal of the American Medical Association*, 2013.

[79] A. Schlögl and G. Supp. Analyzing event-related EEG data with multivariate autoregressive parameters. *Progress in Brain Research*, 159:135–147, 2006. doi: 10.1016/S0079-6123(06)59009-0.

[80] L. Schuh and I. Drury. Intraoperative electrocorticography and direct cortical electrical stimulation. *Seminars in Anesthesia*, 16(1):46–55, 1997. doi: 10.1016/S0277-0326(97) 80007-4.

[81] O. Sergeeva, F. Uhlemann, G. Schackert, C. Hergeth, U. Morgenstern, and R. Steinmeier. Integration of intraoperative 3d-ultrasound in a commercial navigation system. *Zentralblatt Neurochirurgie*, 2006.

[82] J. Sheehan, C. P. Yen, and L. Steiner. Gamma knife surgery – induced meningioma report of two cases and review of the literature. *Journal of Neurosurgery*, 2006.

[83] M. E. Shenton, H. M. Hamoda, J. S. Schneiderman, S. Bouix, O. Pasternak, Y. Rathi, M. A. Vu, M. P. Purohit, K. Helmer, I. Koerte, A. P. Lin, C. F. Westin, R. Kikinis, M. Kubicki, R. A. Stern, and R. Zafonte. A review of magnetic resonance imaging and diffusion tensor imaging findings in mild traumatic brain injury. *Brain Imaging and Behavior*, 6 (2):137–192, 2012. doi: 10.1007/s11682-012-9156-5.

[84] I. A. Shevelev, E. N. Tsicalov, A. M. Gorbach, K. P. Budko, and G. A. Sharaev. Thermoimaging of the brain. *J Neurosci Meth*, 46:49——58, 1993. doi: 10.1016/ 0165-0270(93)90140-M.

[85] Siemens. Somatom definition flash - technical specifications. http://www.healthcare.siemens.com/computed-tomography/dual-source-ct/ somatom-definition-flash/technical-specifications, 2016. Accessed: 2016-04-24.

[86] R. Sitaram, H. Zhang, C. Guan, M. Thulasidas, Y. Hoshi, A. Ishikawa, K. Shimizu, and N. Birbaumer. Temporal classification of multichannel near-infrared spectroscopy signals of motor imagery for developing a brain-computer interface. *NeuroImage*, 34(4): 1416–1427, 2007. doi: 10.1016/j.neuroimage.2006.11.005.

[87] R. S. Snell. *Clinical Neuroanatomy*. LWW, Baltimore, 7th edition, 2010.

[88] S. B. Sobottka, T. Meyer, M. Kirsch, E. Koch, R. Steinmeier, U. Morgenstern, and G. Schackert. Intraoperative optical imaging of intrinsic signals: a reliable method for visualizing stimulated functional brain areas during surgery. *J Neurosurg*, 119(4): 853–863, 2013.

[89] S. B. Sobottka, T. Meyer, M. Kirsch, G. Reiss, E. Koch, U. Morgenstern, and G. Schackert. Assessment of visual function during brain surgery near the visual cortex by intraoperative optical imaging. *Biomedizinische Technik*, 58(3):249–256, 2013. doi: http://dx.doi.org/10.1515/bmt-2012-0074.

[90] X. Song, L. P. Panych, and N. K. Chen. Spatially regularized machine learning for task and resting-state fMRI. *Journal of Neuroscience Methods*, 257:214–228, 2016. doi: 10.1016/j.jneumeth.2015.10.001.

[91] A. T. Sornborger and T. Yokoo. A multivariate, multitaper approach to detecting and estimating harmonic response in cortical optical imaging data. *Journal of Neuroscience Methods*, 203(1):254–263, 2012. doi: 10.1016/j.jneumeth.2011.09.018.

[92] C. J. Stam. Nonlinear dynamical analysis of EEG and MEG: Review of an emerging field. *Clinical Neurophysiology*, 116(10):2266–2301, 2005. doi: 10.1016/j.clinph.2005. 06.011.

[93] G. Steiner, S. B. Sobottka, E. Koch, G. Schackert, and M. Kirsch. Intraoperative imaging of cortical cerebral perfusion by time-resolved thermography and multivariate data analysis. *J Biomed Opt*, 16:16001–16006, 2011.

[94] J. Steketee. Spectral emissivity of the skin and pericardium. *Physics in Medicine and Biology*, 1973.

[95] H.-i. Suk, C.-y. Wee, S.-w. Lee, and D. Shen. State-Space Model with Deep Learning for Functional Dynamics Estimation in Resting-State fMRI. *NeuroImage*, 129:292–307, 2016. doi: 10.1016/j.neuroimage.2016.01.005.

[96] T. Terasawa, T. Dvorak, S. Ip, G. Raman, J. Lau, and T. A. Trikalinos. Systematic review: Charged-particle radiation therapy for cancer. *Annals of Internal Medicine*, 2009.

[97] M. S. Treder, A. K. Porbadnigk, F. S. Avarvand, K.-R. Müller, and B. Blankertz. The LDA beamformer: Optimal estimation of ERP source time series using linear discriminant analysis. *NeuroImage*, 129:279–291, 2016. doi: 10.1016/j.neuroimage.2016.01.019.

[98] D. A. Turner, editor. *Modern Neurosurgery: Clinical Translation of Neuroscience Advances*. CRC Press, 2005.

[99] G. Unsgaard, T. Selbekk, T. B. Müller, S. Ommedal, S. H. Torp, G. Myhr, J. Bang, and T. A. N. Hernes. Ability of navigated 3d ultrasound to delineate gliomas and metastases–comparison of image interpretations with histopathology. *Acta Neurochirurgica*, 2005.

[100] W. Van Paesschen, P. Dupont, S. Sunaert, K. Goffin, and K. Van Laere. The use of SPECT and PET in routine clinical practice in epilepsy. *Current opinion in neurology*, 20 (2):194–202, 2007. doi: 10.1097/WCO.0b013e328042baf6.

[101] B. D. Van Veen, W. van Drongelen, M. Yuchtman, and A. Suzuki. Localization of brain electrical activity via linearly constrained minimum variance spatial filtering. *IEEE Transactions on Biomedical Engineering*, 44(9):867–880, 1997. doi: 10.1109/10.623056.

[102] P. Vincent, H. Larochelle, I. Lajoie, Y. Bengio, and P.-A. Manzagol. Stacked Denoising Autoencoders: Learning Useful Representations in a Deep Network with a Local Denoising Criterion. *Journal of Machine Learning Research*, 11(3):3371–3408, 2010.

[103] M. Vollmer and K.-P. Möllmann. *Infrared Thermal Imaging: Fundamentals, Research and Applications*. WILEY-VCH, Weinheim, 1st edition, 2010.

[104] J. Vrba and S. Robinson. Signal processing in magnetoencephalography. *Methods*, 25: 249 – 271, 2001.

[105] H. Walter, editor. *Funktionelle Bildgebung in Psychiatrie und Psychotherapie.* Schattauer, Stuttgart, 2007.

[106] F. Weidner, N. Hoffmann, Y. Radev, J. Hollmach, C. Schnabel, M. Kirsch, G. Schackert, U. Petersohn, E. Koch, and G. Steiner. Entwicklung eines gehirn-phantoms zur perfusions- und brain shift simulation. In *Rep Biomed Eng*, volume 2, pages 111–113, 2014.

[107] N. M. Wetjen, G. D. Cascino, a. J. Fessler, E. L. So, J. R. Buchhalter, B. P. Mullan, T. J. O'Brien, F. B. Meyer, and W. R. Marsh. Subtraction ictal single-photon emission computed tomography coregistered to magnetic resonance imaging in evaluating the need for repeated epilepsy surgery. *Journal of neurosurgery*, 105(1):71–6, 2006. doi: 10.3171/jns.2006.105.1.71.

[108] C. R. Wirtz, M. M. Bonsanto, M. Knauth, V. M. Tronnier, F. K. Albert, A. Staubert, and S. Kunze. Intraoperative magnetic resonance imaging to update interactive navigation in neurosurgery: method and preliminary experience. *Computer Aided Surgery*, 1997.

[109] J. C. Ye, S. Tak, K. E. Jang, J. Jung, and J. Jang. NIRS-SPM: Statistical parametric mapping for near-infrared spectroscopy. *NeuroImage*, 44(2):428–447, 2009. doi: 10. 1016/j.neuroimage.2008.08.036.

[110] L. Ye and E. Keogh. Time series shapelets: A new primitive for data mining. In *Proceedings of the 15th ACM SIGKDD international conference on Knowledge discovery and data mining*, pages 947–956, 2009.

[111] F. Z. Yetkin, W. M. Mueller, G. L. Morris, T. L. McAuliffe, J. L. Ulmer, R. W. Cox, D. L. Daniels, and V. M. Haughton. Functional mr activation correlation with intraoperative cortical mapping. *American Journal of Neuroradiology*, 1997.

Erklärungen zur Eröffnung des Promotionsverfahrens

1. Hiermit versichere ich, dass ich die vorliegende Arbeit ohne unzulässige Hilfe Dritter und ohne Benutzung anderer als der angegebenen Hilfsmittel angefertigt habe; die aus fremden Quellen direkt oder indirekt übernommenen Gedanken sind als solche kenntlich gemacht.

2. Bei der Auswahl und Auswertung des Materials sowie bei der Herstellung des Manuskripts habe ich Unterstützungsleistungen von folgenden Personen erhalten:
Sen.-Prof. Dr.-Ing. habil Uwe Petersohn.

3. Weitere Personen waren an der geistigen Herstellung der vorliegenden Arbeit nicht beteiligt. Insbesondere habe ich nicht die Hilfe eines kommerziellen Promotionsberaters in Anspruch genommen. Dritte haben von mir weder unmittelbar noch mittelbar geldwerte Leistungen für Arbeiten erhalten, die im Zusammenhang mit dem Inhalt der vorgelegten Dissertation stehen.

4. Die Arbeit wurde bisher weder im Inland noch im Ausland in gleicher oder ähnlicher Form einer anderen Prüfungsbehörde vorgelegt und ist auch noch nicht veröffentlicht worden.

5. Ich bestätige, dass ich die geltende Promotionsordnung der Fakultät Informatik der Technischen Universität Dresden anerkenne.

Dresden, 24.4.2016

Nico Hoffmann